



저작자표시-비영리-변경금지 2.0 대한민국

이용자는 아래의 조건을 따르는 경우에 한하여 자유롭게

- 이 저작물을 복제, 배포, 전송, 전시, 공연 및 방송할 수 있습니다.

다음과 같은 조건을 따라야 합니다:



저작자표시. 귀하는 원저작자를 표시하여야 합니다.



비영리. 귀하는 이 저작물을 영리 목적으로 이용할 수 없습니다.



변경금지. 귀하는 이 저작물을 개작, 변형 또는 가공할 수 없습니다.

- 귀하는, 이 저작물의 재이용이나 배포의 경우, 이 저작물에 적용된 이용허락조건을 명확하게 나타내어야 합니다.
- 저작권자로부터 별도의 허가를 받으면 이러한 조건들은 적용되지 않습니다.

저작권법에 따른 이용자의 권리는 위의 내용에 의하여 영향을 받지 않습니다.

이것은 [이용허락규약\(Legal Code\)](#)을 이해하기 쉽게 요약한 것입니다.

[Disclaimer](#)

공학박사 학위논문

**Interfacial Engineering of Conjugated
Polymers by Nanoconfinement for
Optoelectronic Applications**

나노갭힘효과에 의한 전도성 고분자의
독특한 특성과 광전자 소자로의 응용

2018년 2월

서울대학교 대학원
공과대학 화학생물공학부
고종국

Abstract

**Interfacial Engineering of Conjugated
Polymers by Nanoconfinement
for Optoelectronic Applications**

Jongkuk Ko

School of Chemical and Biological Engineering

The Graduate School

Seoul National University

The conjugated polymers have gained enormous attention as next-generation semiconducting materials because of their tunable electrical and optical properties combined with plastic properties such as toughness, plasticity and elasticity. Therefore, various applications such as OTFT, OLED, OPV, photodetector, and sensor etc., were considered and widely studied. Among various application using conjugated polymers, OLED has already been commercialized and is about to become an alternative displays and light sources. Cheap, flexible and cost-effective solar cells by conjugated polymers are particularly prominent application to solve energy related problems.

Less than 0.1 % of power conversion efficiencies in 1980s have been increased up to more than 12 % recently. There were several breakthroughs by developing of new process methods and new materials. New conjugated polymers such as low

bandgap polymers which more efficiently absorb photons and transfer electrons were synthesized. In addition, bulk heterojunction was discovered which provide large interfaces for charge separation and pathways for efficient charge transfer. However, chemical instability as well as metastable nanostructures by bulk heterojunction which are intrinsic drawbacks of organic materials have made difficult for OPVs to be commercialized. Therefore, it required another breakthrough approach which can enhance both device performance and stability at the same time.

Nanoconfinement could be effective approach to realize both efficient and stable optoelectronic devices. Nano-confined polymers have shown novel structural and dynamical properties which were not obtainable using conventional methods. Controlling the structural properties and dynamics by nanoconfinements could give us new approach to solve the problems. In this study, systematic studies of nanoconfinement effect on structural properties and dynamics of conjugated polymers will be shown. We applied nanoconfinements effects on organic solar cells to realize efficient and stable device performance based on those systematic studies.

In the first Chapter, fundamentals on conjugated polymers, organic solar cells and nanoconfinement effects will be described to address the importance and effectiveness of our approach.

In the second Chapter, nanoconfinement effects on crystalline structure of conjugated polymer were studied. Based on structural studies, organic semiconductor thin films with dramatically enhanced charge mobility along with superior oxidization resistivity were realized by exploiting nanoconfinement followed by solution-based doping. First, easy and mass-producible methods to fabricate nanostructures of conjugated polymers will be introduced. Parameters of conjugated polymer nanostructures such as size, geometry and composing materials

were easily controlled using newly developed patterning methods. Based on those newly developed patterning methods, systematic studies on the effect of nanoconfinement on structural properties of conjugated polymers were conducted. We fabricated nanopillars, nanoholes, and nanocones of conducting polymer with different chemical structure, dimension, and crystallinity based on patterning with soft PFPE templates. GIWAXS measurements showed the changes in both chain orientation and crystallinity depending on the degree of confinement which are quite different from the bulk crystallinity of conducting polymers. More than 20 times higher population of crystallites having face-on orientation were obtained by nanoconfinement effect. In addition, they have shown more than two magnitudes higher charge mobility along vertical direction by increased crystallinity. Moreover, doping on those nanostructured films further increased the conductivity 400 ~ 500 times higher than that of bulk film.

In the third chapter, two examples of nanoconfined geometry showing unusual dynamics of molecules will be shown. Based on those dynamical studies, organic solar cells with increased device performance and stability were realized. First we used nanowire network structures in bulk heterojunction as confinement geometry. we demonstrate a novel strategy for the stabilization of nanomorphology of organic solar cells by inducing polymeric nanowire network structures. The physically interconnected network structures form robust electron donor domains and impose confinement which suppresses the aggregation of the electron acceptor, [6,6]-phenyl-C61-butyric acid methyl ester (PCBM). Organic solar cells having the nanowire network structures showed increased power conversion efficiencies and dramatically enhanced thermal stability compared to BHJ and non-network nanowire-based devices. Second geometry is quasi-OHJ fabricated by sequential

process. For this study we used PTB7 and PCBM. PTB7 were first deposited on substrate. And on PTB7 films, PCBM dissolved in DCM/DIM were deposited by spin-casting. During the spin-coating process, some PCBM were diffused into PTB7 amorphous phases forming interdigitated structures at the interfaces. Because of such as interdigitated structures, confined structures at the interfaces, they showed significantly enhanced device stabilities. Compared to device performance of BHJ were deteriorated within initial 10 hours, other nanoconfined devices showed stabilized performance more than 1,000 hours.

In the last chapter, effect of nanoconfinement on both structural properties and dynamics was applied to organic solar cell to realize efficient and stable organic solar cells. P-type materials PCBM and PNDIT were deposited on top of 70 nm sized P3HT nanopillars to fabricate ordered heterojunction geometry. Strong face-on orientation with high crystallinity in P3HT nanopillars will provide effective pathways for hole transport along vertical direction. Their interdiffusion between donor and acceptor molecules were effectively controlled by changing annealing conditions. In addition, their dynamics were quantitatively analyzed by in-situ GISAXS experiments. They have shown different rate of diffusion and stabilized degree of diffusion. We could obtain highly enhanced device performance by decreasing domains sizes from the controlled interdiffusion of donor and acceptor molecules. Moreover, they endured harsh thermal conditions up to 200 °C for 4 hours by the stabilized interdiffusion due to nanoconfinement.

Keywords: Conjugated Polymers, Nanoconfinement, Organic Solar Cells

Student Number: 2012-22578

Table of Contents

Chapter 1. Introduction	1
1.1. Fundamentals on Organic Photovoltaics	1
1.1.1. Introduction to organic photovoltaics.....	1
1.1.2. Working principles of organic photovoltaics.....	3
1.2. Challenges in Organic Photovoltaics	6
1.1.1. Device performance	6
1.1.2. Device Stability	10
1.3. Unique Properties of Conjugated Polymers under Nanoconfinement	12
1.3.1. Fundamentals on nanoconfinement effects	12
1.3.2. Conjugated polymers under nanoconfinement.....	14
Chapter 2. Unique Structural Properties of Conjugated Polymers by Nanoconfinement for Enhanced Electrical Properties	16
2.1. Introduction	16
2.2. Experimental.....	18
2.3. Results and Discussion	20
2.3.1. Development of patterning methods	20
2.3.2. Nanoconfinement effects on crystalline structures by the size of nanostructures.....	23
2.3.3. Nanoconfinement effects on crystalline structures by the geometry of nanostructures.....	26
2.3.4. Electrical doping on nanostructured conjugated polymers	29
2.3.5. Enhanced optical and electrical properties by nanoconfinement effects	31
2.4. Conclusion.....	33
Chapter 3. Unusual Dynamics of Conjugated Polymers by Nanoconfined Geometry for Stabilized Nanomorphology	34
3.1. Introduction	34
3.2. Nanoconfined Geometry by Polymeric Nanowire Network Structures in Bulk Heterojunction Solar Cells	36

3.2.1. Experimental	39
3.2.2. Results and discussion	41
3.3. Nanoconfined geometry by quasi-Ordered Heterojunction Solar Cells Fabricated by Sequential Process	60
3.3.1. Experimental	63
3.3.2. Results and discussion	65
3.4. Conclusion.....	80
Chapter 4. Controlling Structural Properties and Dynamics of Conjugated Polymers by Nanoconfined Geometry for Efficient and Stable Organic Solar Cells	82
4.1. Introduction	82
4.2. Experimental	84
4.3. Results and Discussion	86
4.3.1. Ordered Heterojunctions by Polymer : Fullerene System	86
4.3.2. Ordered Heterojunctions by Polymer : Polymer System	108
4.4. Challenges and Further Works	118
Bibliography	120
Abstract in Korean.....	127

List of Tables

Table 3.2.1. Summary of fitted results of Figure 3.2.6..	50
Table 3.2.2. Table 3.2.1. Summary of fitted results of Figure 3.2.6..	52
Table 3.2.3. Summary of device performances with different additives and annealing conditions..	55
Table 3.2.4. Summary of device performance of P3HT:PCBM blend films without additives..	57
Table 3.2.5. Summary of device performance of P3HT:PCBM blend films without additives..	59
Table 3.3.1. Current-voltage (J-V) characteristics) of OSCs with various photoactive layer conditions.....	77
Table 4.3.1. Summary of ensemble average conductivity and photoconductivity extracted from the histograms of Figure 4.3.9.	
Table 4.3.2. Performance parameters of nanostructured P3HT/PCBM solar cells extracted from the J-V characteristics.	106

Table of Contents

Figure 1.1.1. Schematic illustration of working principles of organic solar cells..	4
Figure 1.1.2. Schematic illustration of J-V characteristics of organic solar cells..	5
Figure 1.2.1. Schematic illustration of development of nanomorphology geometry in organic solar cells.....	8
Figure 1.2.2. Timeline of best research-cell energy conversion efficiencies produced by NREL.	9
Figure 1.2.3. Schematic diagram of the strategies to increase stability. © Royal Society of Chemistry.....	11
Figure 1.3.1. Schematic illustration of nanoconfinement effects on structural properties and dynamics of polymers.....	13
Figure 2.3.1. a) A schematic illustration for the procedure to fabricate nanopillars of conjugated polymers. b) GISAXS 2D results which measured P3HT nanopillars..	21
Figure 2.3.2. SEM top images of conjugated polymer nanostructures changing various parameters (size, geometry, and materials).....	22
Figure 2.3.3. GIWAXS 2D results measured different size of nanopillars using different kinds of conjugated polymers.....	24
Figure 2.3.4. . a) GIWAXS 2D results and 1D profiles of P3HT flat films and P3HT nanopillars. b) Line cuts along out-of-plane direction of PCDTBT nanopillars and PTB7 nanopillars.....	25
Figure 2.3.5. . a) Calculated penetration depth of X-ray beams at different incidence angles. b) Schematic illustrations of penetration of X-ray beams at difference incidence angles.	27
Figure 2.3.6. a) GIWAXS 2D results of PTB7 nanopillars and nanocones which were measured at different incidence angles. b) Calculated ratios of (010) peak intensity	

to (100) peak intensity of PTB7 nanopillars and PTB7 nanocones at different incidence angles.28

Figure 2.3.7. (a) Schematics of electrically-doped nanopillars by PMA molecules. (b) SEM top and cross-section images of electrically-doped nanopillars and (c) XPS depth profiling of electrically-doped nanopillars.30

Figure 2.3.8. (a) Schematics of method for measuring charge mobilities of nanostructured samples. Log-log plots of current density of (b) PTB7 and (c) P3HT. (d) Normalized charge mobilities of samples when they are exposed in air up to 100 hours.32

Figure 3.2.1. Schematic of transition from P3HT nanowires to nanowire network structures by thermal annealing.38

Figure 3.2.2. UV-Vis absorption spectra of P3HT:PCBM blend films prepared from blend solutions added with (a) CHN and (b) 2CP at different annealing conditions.43

Figure 3.2.3. AFM phase images of top PCBM over layer removed P3HT:PCBM blend films spin-coated from blend solution added with (a) ~ (d) cyclohexanone and (e) ~ (h) 2-chlorophenol with different annealing conditions.44

Figure 3.2.4. Two dimensional GIWAXS patterns of P3HT:PCBM blend films prepared from blend solutions added with (a), (c), (e), (g) CHN and (b), (d), (f), (h) 2CP at different annealing conditions. Line cuts along horizontal directions and angular cuts from 2D GIWAXS patterns of (i), (k) CHN added samples and (j), (l) 2CP added samples.45

Figure 3.2.5. SANS profiles of P3HT:PCBM blend films prepared from (a) cyclohexanone added, (b) 2-chlorophenol added at different annealing conditions and (C) profiles of 2CP added samples and CHN added samples annealed at 150 °C for comparison of their network sizes.48

Figure 3.2.6. SANS profiles of P3HT:PCBM blend films (a) as cast and annealed at (b) 80 °C, (c) 120 °C, and (d) 150 °C prepared from blend solutions with cyclohexanone and their fitted curves.....	49
Figure 3.2.7. SANS profiles of P3HT:PCBM blend films (a) as cast and annealed at (b) 80 °C, (c) 120 °C, and (d) 150 °C prepared from blend solutions with 2-chlorophenol and their fitted curves.....	51
Figure 3.2.8. The current density-voltage characteristics of devices spin-coated from P3HT:PCBM blend solutions with different additives at different annealing conditions. a) J-V curve, b) IPCE of solar cells.	54
Figure 3.2.9. J-V characteristics of as cast and annealed at 150 °C P3HT:PCBM blend films without additives under simulated AM 1.5G solar illumination..	56
Figure 3.2.10. Stability curves of devices to compare the differences between non-additive and additives, network and non-network structures under continuous heating at 120 °C for 120 minutes.....	58
Figure 3.3.1. Schematic illustration of procedures and nanomorphology fabricated by sequential process.....	62
Figure 3.3.2. 2D Grazing-Incidence Wide-Angle X-ray Scattering (GIWAXS) patterns of PTB7-th depending on solvent and grazing incident angle.....	68
Figure 3.3.3. 2D Grazing-Incidence Wide-Angle X-ray Scattering (GIWAXS) patterns of PTB7-th \ PC70BM sequentially deposited layers depending on solvent and grazing incident angle.....	69
Figure 3.3.4. 2D Grazing-Incidence Wide-Angle X-ray Scattering (GIWAXS) patterns of PTB7-th \ PC70BM sequentially deposited layers depending on solvent and grazing incident angle.....	70
Figure 3.3.5. Scattering intensities measured at (010) position in qz direction with different grazing incidence angles and deposition solvents of (a) PTB7-th and (b) PTB7-th \ PC70BM sequentially deposited layers.....	71

Figure 3.3.6. (a) Current-voltage (J-V) characteristics, (b) incident photon-to-electron conversion efficiency (IPCE) of OSCs with PTB7-th dissolved in various solvents with identical thickness of photoactive layer..	76
Figure 3.3.7. (a) Current-voltage (J-V) characteristics of HODs and (b) VOC as a function of Plight varying the solvent of PTB7-th.	78
Figure 3.3.8. Degradation tendency of (a) JSC, (b) VOC, (c) FF, (d) PCE as a function of 85°C thermal aging at 85°C for 1000 h.	79
Figure 4.3.1. a) A schematic illustration for the procedure to fabricate P3HT nanopillars and subsequent PCBM deposition. b) Plan-view and cross-section scanning electron microscopy (SEM) images of P3HT nanopillars prepared. c) A diagram showing the change in volume fraction of P3HT pillars and cavities as a function of pillar diameter (where D_p is the pillar diameter and D_{int} is the pillar to pillar distance).	89
Figure 4.3.2. . a) A schematic illustrating of the two types of diffusion processes. SFM height images of b) P3HT:PCBM nanostructured samples as-prepared and annealed at four different temperatures (80, 120, 150, and 180 °C) for 20 min and c) P3HT nanopillar structures with PCBM top layers that were removed by cyclohexane.	90
Figure 4.3.3. Horizontal cuts of GISAXS measurements of a P3HT pillar only film (red) and a sample with P3HT pillars deposited with PCBM (blue) with corresponding Miller indices. The P3HT pillar only film shows the hexagonal scattering with the fourth-order peak feature representing a good ordering of the P3HT nanopillars. The P3HT pillars surrounded by PCBM shows the first and second order peaks due to low electron density contrast between P3HT and PCBM..	91
Figure 4.3.4. GIWAXS 2D scattering patterns of a) P3HT nanopillars, b) as-prepared nanostructured P3HT/PCBM films (PCBM deposited on P3HT nanopillars), and c) nanostructured P3HT/PCBM films annealed at 80 °C, d) 120 °C, e) 150 °C, and f) 180 °C. g) The ratio of face-on orientation population to edge-on	

orientation of nanostructured P3HT/PCBM films with 4 different anneal temperatures. The changes in crystal size as a function of annealing time: h) in the in-plane direction and i) in the out-of-plane direction at 4 different annealing temperatures.....93

Figure 4.3.5. GIWAXS line cuts along: (a) qy and (b) qz directions from nanostructured P3HT/PCBM films, which were measured during thermal anneal at 4 different anneal temperatures (80, 120, 150, and 180 °C) up to 120 min..94

Figure 4.3.6. Figure 4.3.6. (a) Angular cuts at the (010) position of P3HT pillar-only, as-cast P3HT pillar/PCBM, and the P3HT pillar/PCBM samples annealed at 4 different temperatures. (b) A schematic on the contributions to face-on (red), edge-on (blue), and isotropically (white) oriented P3HT in the integrated intensity of the angular cut.....95

Figure 4.3.7. The changes in GISAXS scattering profiles of nanostructured P3HT/PCBM as a function of annealing time (up to 120 min) at: a) 80 °C, b) 120 °C, c) 150 °C, and d) 180 °C. e) The changes in total scattering intensity (TSI) as a function of annealing time at 4 different anneal temperatures. f) The changes in the fraction of P3HT diffused into surroundings as a function of annealing time for the samples annealed at 150 and 180 °C.....98

Figure 4.3.8. Height images of nanostructured P3HT/PCBM films a) with and b) without PCBM cap layer removed by cyclohexane treatment (i.e., only P3HT nanopillars remained) at 4 different annealing temperatures. c) SFM images of nanostructured P3HT/PCBM films in the c) dark state and d) illuminated state annealed at 4 different temperatures..102

Figure 4.3.9. Histograms extracted from the cSFM results (with >1500 pillars) on the nanostructured P3HT/PCBM films with (a) as prepared and annealed at: (b) 80 °C, (c) 120 °C, (d) 150 °C, and (e) 180 °C.....103

Figure 4.3.10. J-V characteristics of nanostructured P3HT/PCBM solar cells in different anneal conditions (as-prepared, annealed at 80 °C, 120 °C, 150 °C, and 180 °C), measured under 1 Sun illumination..105

Figure 4.3.11. (a) A schematic illustration of the conductivity distribution on nanostructured P3HT:PCBM films. The QI-SFM images of: (b) height and (c) conductivity for a nanostructured P3HT:PCBM film (as-cast) with illumination and their (d) cross-sectional height and current graphs. The surroundings of pillars, which are mainly filled with PCBM, show higher conductivity than the P3HT pillar regions due to higher charge mobility of PCBM. 107

Figure 4.3.12. a) A schematic illustration for the procedure to fabricate P3HT nanoholes and subsequent PNDIT deposition. b) Plan-view scanning electron microscopy (SEM) images of P3HT nanoholes prepared. c) Chemical structures of polymers used in this study. 2D GISAXS patterns of d) P3HT nanoholes, e) P3HT nanoholes/PNDIT and f) P3HT nanoholes/PNDIT2..... 110

Figure 4.3.13. a) A schematic illustration for the procedure to fabricate P3HT nanoholes and subsequent PNDIT deposition. b) Plan-view scanning electron microscopy (SEM) images of P3HT nanoholes prepared. c) Chemical structures of polymers used in this study. 2D GISAXS patterns of d) P3HT nanoholes, e) P3HT nanoholes/PNDIT and f) P3HT nanoholes/PNDIT2..... 112

Figure 4.3.14. The changes in GISAXS scattering profiles of nanostructured P3HT/PNDIT as a function of annealing time (up to 120 min) at: a) as-prepared, b) 120 °C, c) 140 °C, d) 160 °C, d) 180 °C, and d) 200 °C..... 114

Figure 4.3.15. Contour plots of a) molecular diffusion and d) power conversion efficiencies as a function of annealing time and temperatures..... 116

Figure 4.3.16. Figure 4.3.16. Device stabilities as a function of active layer geometry, annealing temperature and time... 117

Chapter 1. Introduction

1.1. Fundamentals on Organic Photovoltaics

1.1.1. Introduction to organic photovoltaics

The organic materials, polymers were considered as insulators. At the beginning of the 20th century, semi-conducting properties of organic materials were first discovered for anthracene. In the 1970s conducting polymers were discovered¹ and received enormous attention for their diverse applications due to their electrical and optical properties combined with plastic properties such as toughness, plasticity, resistance to friction and elasticity. Among various application using conducting polymers, OLED has already been commercialized and are about to become an alternative displays and light source. Allan J. Heeger, Ala G. MacDiarmid, and Hideki Shirakawa received the Nobel Prize in Chemistry in 2000 for the discovery and development of these conductive polymers.

Polymers consists of repetition of monomer by carbon-carbon covalent bonds. Conventional polymers which are called as plastics, are linked by four carbon-carbon single bonds by hybridization of one s orbital and three p orbitals with a length of 1.54 Å and do not conduct electrons. However, electrons could transport through the backbone of polymers when the electrons are delocalized in π -electron system by alternating single and double bonds formed by two s orbitals and two p orbitals. The delocalized π orbital is the highest occupied molecular orbital (HOMO), and the π^* orbital is the lowest unoccupied molecular orbital (LUMO). The energy differences between the HOMO and LUMO which in the rage of 1-4 eV are band gap of conducting polymers and allows absorbance of lights to convert into electricity.

Organic solar cell is an important application of optoelectronic properties,

absorbance of photons and convert into light, of conductive polymers. They have attracted extensive attention because of their promising advantages such as light weight, facile tunability, flexibility and low cost. In addition, band gaps of conjugated polymers can be controlled by changing chemical structures of conjugated polymers to absorb or transmit different wavelength of light such NIR, Vis and UV. Moreover, very thin layers of solar cell about 100 – 200 nm are available because of their high absorption coefficient of organic molecules. Based on those unique properties, potentially various applications are available such as window with solar cells and indoor solar cells as well as alternatives for brittle, heavy silicon solar cells.

However, intrinsic drawbacks of organic materials such as low dielectric constant and charge mobility make organic solar cells to have low charge conversion efficiency compared to inorganic counterparts. Excitons are strongly bound electron and hole pairs in organic semiconductors.² Therefore, excitons should be diffused to donor-acceptor interfaces to be dissociated into electrons and holes by electric field.³ However very short diffusion length (~10 nm)^{4, 5} by low dielectric constants and low charge mobilities makes recombination easily during the photon to electron conversion process.

To overcome above mentioned problems, bulk heterojunction geometry was suggested to optimize exciton dissociation and charge transport process.^{6 7 8} However, degradation of the active layer morphology by metastable nanostructures^{9 10 11 12 13} as well as permeation of oxygen and water^{14 15 16} and mechanical instability¹⁷⁻¹⁹ makes organic solar cells to be unstable during operation in ambient conditions. In-detail challenges in the point of device performance and stability will be described in chapter 1.2

1.1.2. Working principles of organic photovoltaics

Mechanism of OPV consists of five steps (1) light absorbance, (2) generation of exciton, (3) diffusion of exciton to the donor-acceptor interface, (4) exciton dissociation at the interface, and (4) charge transport to each electrode. Organic solar cells operate based on the photovoltaic effect. Photons with the energy larger than the band gap of polymers are absorbed creating excitons, which is different from inorganic based solar cells. The excitons, bound pair of electron-hole requires additional energy to overcome binding energy of 0.1 – 0.4 eV to be dissociated.² Excitons could be separated into electron and hole pair by electric fields. Therefore, they diffuse into electron donor-acceptor interfaces and dissociated.⁵ Dissociated charges transported to each electrodes and finally injected to outer circuit. All of the process is important factors which determine the overall solar cell efficiency and large amounts of efforts were devoted to optimize energy conversion process by developing new materials,²⁰⁻³³ and process methods.^{8, 34-36 37 38-50}

Electrical characteristics of solar cells are described as four factors short-circuit current, open circuit voltage and fill factor and power conversion efficiency by measuring J-V characteristics under illumination. The open-circuit voltage, V_{oc} is the maximum voltage across the solar cell measured when the device is open-circuited. The short-circuit current density, J_{sc} is maximum available current density of solar cells measured at the condition of short-circuited. The fill factor, FF is defined as product of V_{oc} and J_{sc} divided by maximum obtainable power of solar cells. Those factors are highly related with quality of solar cell devices. Power conversion efficiency is the device performance parameter of a solar cell, defined as producible power per incidence light usually air mass 1.5.

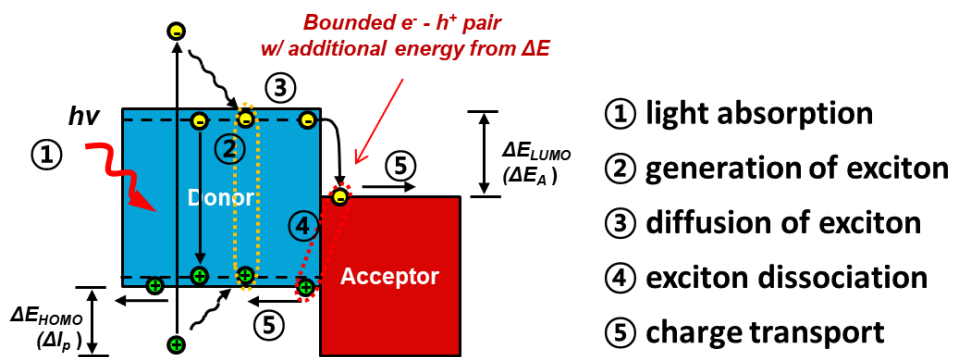


Figure 1.1.1. Schematic illustration of working principles of organic solar cells.

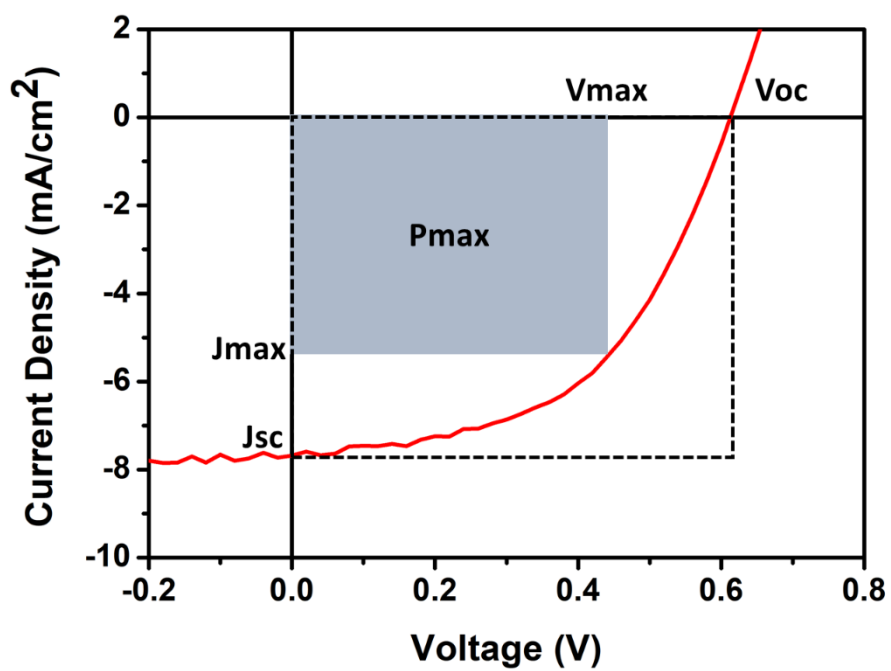


Figure 1.1.2. Schematic illustration of J-V characteristics of organic solar cells.

1.2. Challenges in Organic Photovoltaics

1.2.1. Device performance

As a consequence of the enormous efforts, the power conversion efficiency (PCE) has reached over 12-13%³⁰⁻³³ recently. There were several important breakthrough in the field of organic solar cells by developing of new process methods and new materials. Since the photo-induced current by anthracene were first reported by Kalman and Pope in 1959, less than 0.1 % of power conversion efficiencies were reported until 1980.⁵¹ The first breakthrough was made by C. W. Tang adopting stacked electron donor and acceptor materials, copper phthalocyanine \ perylene tetracarboxylic derivative and reported higher than 1 %.⁵² The second breakthrough was made by the development of bulk heterojunction geometry which is fabricated by spin-coating of electron donor and acceptor blend solutions.⁶⁻⁸ The bulk heterojunction was consisted of donor and acceptor physically mixed nano-phases to maximize interfacial surface between donor and acceptor materials. The introduction of bulk heterojunction (BHJ) photoactive layer greatly boosted the low power conversion efficiency (PCE) because of the preferable nanoscale charge migration path, which allows thick photoactive layer without any loss of charge extraction property. Since then various approaches have been suggested to control the nano-morphologies of BHJs and to obtain optimal nanostructure such as thermal³⁴ and solvent annealing,³⁵ solvent selection,⁸ mixed solvents³⁶ and using additives.³⁷ However, slight changes in process conditions lead to disturbed 3-dimensional nano-phases, resulting in unpredictable and unscalable BHJ morphology under mass fabrication conditions. In addition, it is difficult to control the molecular-scale structures such as chain orientation and crystallinity without altering the molecular structure.

Other geometries were suggested and studied. Ordered heterojunction, which is interdigitated donor and acceptor structures with the size of 20 nm were suggested to be an ideal nanomorphology of organic solar cells.³⁸⁻⁵⁰ However, control on nanostructure with size under 20 nm is much more difficult to fabricate and often requires very expensive lithography techniques.^{38, 41, 44, 47, 50, 53} And it often caused defects and trap sites at the donor acceptor interfaces making lower device performance than BHJ's.

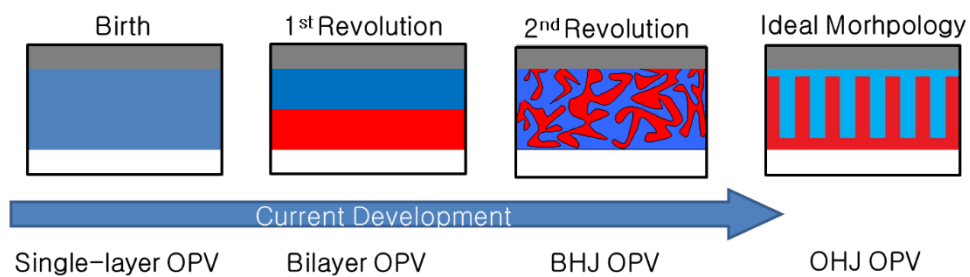


Figure 1.2.1. Schematic illustration of development of nanomorphology geometry in organic solar cells.

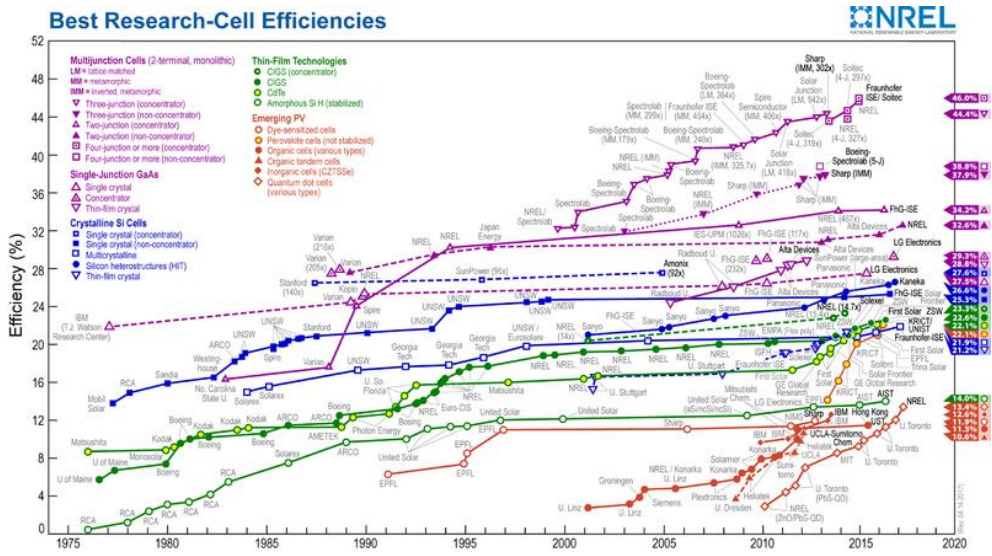


Figure 1.2.2. Timeline of best research-cell energy conversion efficiencies produced by NREL.

1.2.2. Device Stability

Development of new donor and acceptor materials, along with the optimization of device morphology at the nanometer scale, has led to organic photovoltaic devices with more than 12 % power conversion efficiency ³⁰⁻³³, pushing them closer to commercialization. These achievements are centered around the discovery of ultrafast electron transfer ^{20, 21} from bulk heterojunction geometry in organic photovoltaics. Although the utilization of bulk heterojunctions has led to transformative advances in the area of energy conversion, the metastable nanostructures of randomly distributed donor and acceptor domains often lead to low thermal stability^{9 10 11 12 13}. Therefore, methods for inducing favourable nanoscale morphology to enhance operational stability need to be addressed. It requires above 7 % of power conversion efficiency in large area with more than 5 years of lifetimes for the commercialization according to economic assessment. ⁵⁴

Moreover, OPVs are also suffered from permeation of photo, air, water and mechanical stabilities. Several methods were suggested to overcome those low stabilities as shown in Figure 1.2.3. However, it is relative lacks on study of device stability. New approach and breakthrough is required. ⁵⁵⁻⁵⁹

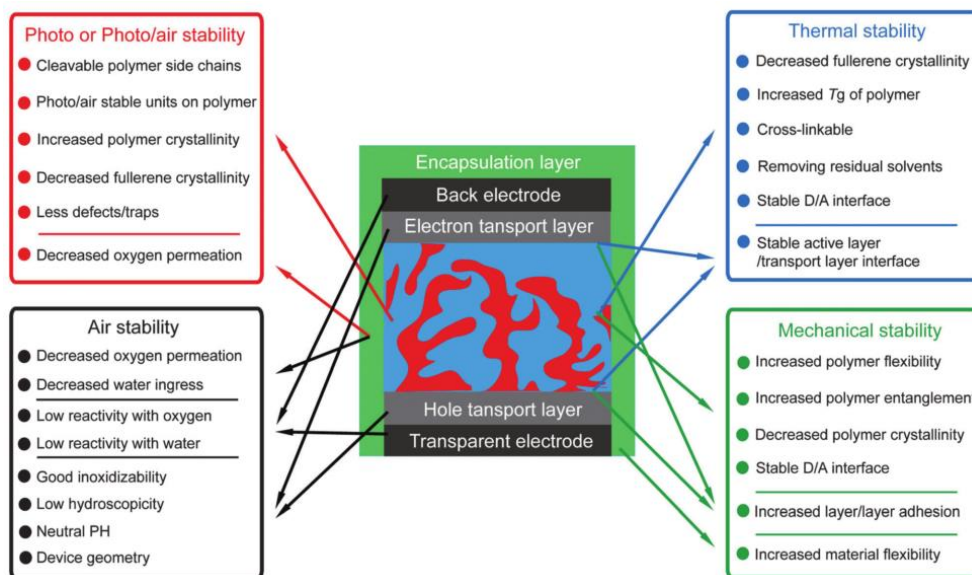


Figure 1.2.3. Schematic diagram of the strategies to increase stability.

© Royal Society of Chemistry.

1.3. Unique Properties of Conjugated Polymers under Nanoconfinement

1.3.1. Fundamentals on nanoconfinement effects

Polymers have shown quite different properties compared to other organic and inorganic materials such as structural properties and dynamics because they are chained molecules. Especially when they are confined in nanostructures under 100 nm size, they have shown peculiar structural properties and dynamics compared to when they are in bulk state. There were several studies on the effect of nanoconfinement using various geometries from 1 dimensional,⁶⁰⁻⁶⁵ 2 dimensional^{42, 44, 48, 50, 53, 66-71} to 3 dimensional geometry.^{72, 73}

When the polymers are in the state of thin film, which is the case of one dimensional confinement, they have shown different structural properties and chain dynamics due to interaction with substrate. Their crystallinity, chain orientation and glass temperatures could be altered due to confinement.⁶⁰⁻⁶⁵ When the polymers are in the nanostructures under 100 nm, nanoconfinement more significantly affected the structural properties and dynamics because of interaction of wall and suppressed radius of gyration of polymers.^{42, 44, 48, 50, 53, 66-71} Recently 3-d confinement using colloids system were shown. Block copolymer, which consists of two different polymers linked by chemical bonds, have shown interesting morphologies when they are confined in 3-d.^{72, 73} New nanamorphology and unique properties by a confinement could be applicable for the novel applications.

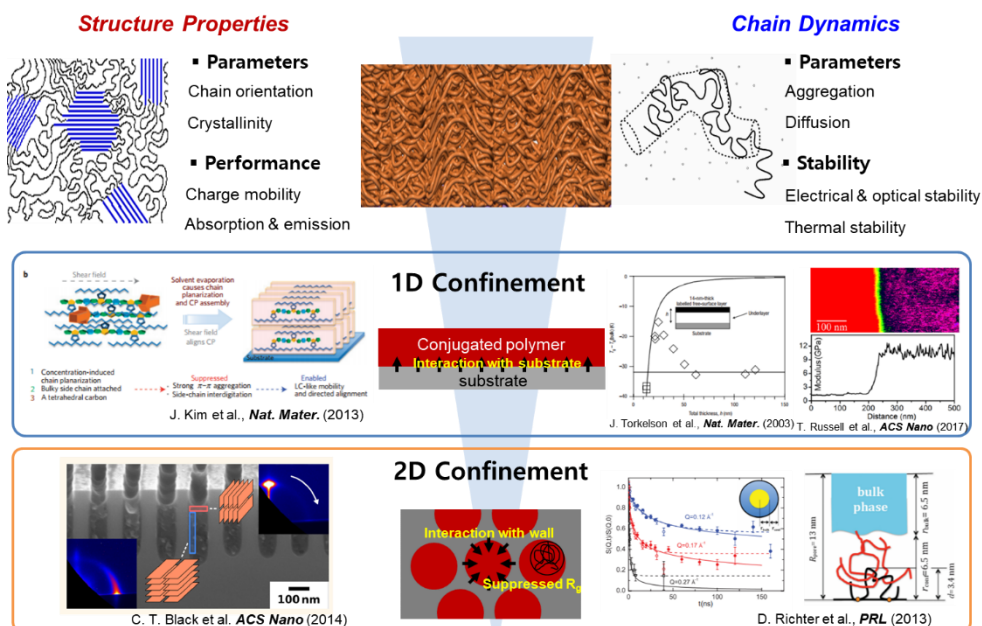


Figure 1.3.1. Schematic illustration of nanoconfinement effects on structural properties and dynamics of polymers

1.3.2. Conjugated polymers under nanoconfinement

Structural properties and chain dynamics of conjugated polymers are related with device performance and stability. There were studies on effect of nanoconfinement on structural properties to chain orientation and crystallinity of conjugated polymers which critically influence on the device performance of solar cells.

By using 1-d confinement, their chain orientation was effectively controlled by controlling the interaction with substrate. Charge mobilities along horizontal direction were highly increased for the application of OTFT⁶⁴ and light illumination were highly increased in OLED⁷⁴⁻⁷⁷ applications.

2-d nanostructures were employed for the further confined geometry. All the studies used P3HT, semicrystalline polymer due to easy process and characterization. P3HT, semicrystalline polymer have shown edge-on orientation in the bulk state, and thin film state. However, when they are confined under 100 nm nanostructures, their chain orientation was changed from edge-on to face-on orientation^{42, 44, 48, 50, 53, 66, 67} which leads to more than 2 magnitudes higher charge mobility⁷⁰ along vertical direction which were not obtainable using conventional methods.

However, there were no studies using low bandgap polymer which is amorphous because it is difficult to realize nanostructures under 100 nm. The properties of low bandgap polymers will be quite different from those of P3HT because they are amorphous polymers. In addition, the dynamics of conjugated polymers have been rarely studied. Compared to inorganic based solar cells whose molecules are linked by strong chemical bonding, blended organic materials are too weak to external stimuli. Therefore, understanding and controlling dynamics of organic materials is critical to realize stabilized device performance. As mentioned

in Chapter 1.2.2, device stability is also important challenges for the commercialization of solar cells. Nanoconfinement could be effective approach to control both structural properties and dynamics at the same time to realize efficient and stable optoelectronic applications.

Chapter 2. Unique Structural Properties of Conjugated Polymers by Nanoconfinement for Enhanced Electrical Properties

2.1. Introduction

Organic electronic devices have attracted much attention as lightweight, low-cost, and easy-to-process replacements for inorganic devices. However, inherent drawbacks of organic materials such as low charge mobility and vulnerable to heat and oxygen make it difficult for commercialization. Different chemical structures of organic semiconductors and process methods have been suggested to realize superior and stable electrical properties. Among them, nanostructuring as well as proper doping of organic semiconductors remains as a major potential and challenges. Previous studies have shown that conducting polymers have different structural properties when they are under nanoconfined geometry.^{42, 44, 48, 50, 53, 66, 67, 70} However, there have been no systematic studies because it is difficult to realize nanostructures of polymers with complicated chemical structure. Even though several studies have shown fabrication of nanopillars with P3HT, it was difficult to realize nanostructures of conjugated polymers under 100 nm using polymers without Tg. Moreover, all the previous approach was complicated and require harsh condition such as high pressure and temperature as well as strong acid and base which will deteriorate electrical properties of conjugated polymers.^{38, 41, 44, 47, 50, 53} In addition, solution-based electrical doping of organic semiconductors has recently been introduced and only applied to flat thin films.⁷⁸ However, there was no studies of doping on nanostructured samples.

In this chapter, organic semiconductor thin films with dramatically enhanced charge mobility along with superior oxidization resistivity were realized by exploiting nanoconfinement followed by solution-based doping. First, easy and mass-producible methods to fabricate nanostructures of conjugated polymers will be introduced. Parameters of conjugated polymer nanostructures such as size, geometry and composing materials were easily controlled. Nanopillar, nanohole and nanocone structures having different feature sizes from 40 – 200 nm were easily fabricated. Also various conjugated polymers were easily used for the fabrication of nanostructures.

Based on those newly developed patterning methods, systematic studies on the effect nanoconfinement on structural properties of conjugated polymers were conducted. We fabricated nanopillars, nanoholes, and nanocones of conducting polymer with different chemical structure, dimension, and crystallinity based on patterning with soft PFPE templates. GIWAXS measurements showed the changes in both chain orientation and crystallinity depending on the degree of confinement which are quite different from the bulk crystallinity of conducting polymers. poly(3-hexylthiophene-2,5-diyl) (P3HT), typical semicrystalline conducting polymer, and poly[N-9'-heptadecanyl-2,7-carbazole-alt-5,5-(4',7'-di-2-thienyl-2',1',3'-benzothiadiazole)] (PCDTBT) and poly[4,8-bis(5-(2-ethylhexyl)thiophen-2-yl)benzo[1,2-b;4,5-b']dithiophene-2,6-diyl-alt-(4-(2-ethylhexyl)-3-fluorothieno[3,4-b]-thiophene-)-2-carboxylate-2-6-diyl] (PTB7), which are well known semicrystalline and amorphous conducting polymers used for organic solar cells, particularly showed dramatic effects by the nanoconfinement. Because of the increased crystallinity by the nanoconfinement, those nanopillars showed more than two magnitude higher conductivity than bulk film.

Additionally, to obtain better electrical properties, nanostructured conjugated polymers were electrically doped by solution based methods. Doping on those nanostructured films further increased the conductivity 400 ~ 500 times relative to the bulk film. They have shown more increased charge mobility than non-doped nanostructure samples as well as highly increased oxidization stability.

2.2. Experimental

Fabrication of AAO Templates and Surface Modification AAO templates were prepared by the two-step anodization process of high purity aluminum sheet (99.999 %, Goodfellow).⁷⁹ An aluminum sheet was electropolished in a mixture solution of perchloric acid (HClO₄, Aldrich) and ethanol (C₂H₅OH, Aldrich) at 20 V. The polished aluminum template was then anodized at 40 V in 0.3 M oxalic acid solution at 15 °C for 4 hrs. After the first anodization, the aluminum oxide film was chemically eliminated by etching in a mixture of phosphoric acid and chromic acid at 45 °C for 10 hrs. Finally, the second anodization was performed at the same condition as the first anodization. The depth of pores was controlled by varying the time lapse of the second anodization. Subsequently, the pore widening was performed by immersing the resulting AAO template in phosphoric acid solution (10 wt%). For the surface modification of the AAO template, it was treated with oxygen plasma in 1 scm of oxygen flow at 25 W for 3 min and immersed in a solution of 0.5 wt% 3-(aminopropyl triethoxysilane) (APTES) aqueous solution for 15 min. The APTES-treated AAO template then reacted with monoglycidyl ether-terminated poly-dimethylsiloxane (PDMS) at 80 °C for 4 hrs.⁸⁰ Nanostructures of P3HT nanopillars were characterized with FE-SEM (JSM-6701F in Seoul National

University Chemical & Biological Engineering Research Facilities and JSM-6700F in the National Center for Inter-University Research Facilities of Seoul National University)

Fabrication of PFPE Replica Molds and Pattern Transfer First, nanopillar patterned PUA was replicated from the PDMS-grafted AAO template. The PUA replica mold was detached from the AAO template after UV precure of PUA within the AAO mold. More than 3 hrs of additional UV cure was performed to guarantee the complete reaction of the PUA mold. The second replica mold from the PUA mold was fabricated using polyfluoropolyether (PFPE). Nanopore PFPE pattern was fabricated by following the same procedure to prepare the PUA replica mold. Then, a P3HT (4002-EE, Rieke-Metals) solution in chloroform was spin-coated on the PFPE replica mold to fill up the nanopores of the PFPE mold. Finally, a hexagonally packed array of P3HT nanopillars was obtained by transferring the P3HT films on a target substrate with heat (50 - 60 °C for 1 min) and pressure (~ 4 bar). The PFPE mold was easily released when the treatment temperature was lowered to room temperature.

GIWAXS Measurements Details GIWAXS was performed at the 3C Beamline of the Pohang Accelerator Laboratory (PAL). All samples were prepared on Si wafer. X-ray with a wavelength of $\lambda = 1.29 \text{ \AA}$ and incident angles varying from 0.11° to 0.15° were used for the measurements. Same exposure time was used for fair comparison.

2.3. Results and Discussion

2.3.1. Development of patterning methods

All the previous methods based on soft lithography requires expensive and complicated processes. In addition, they require harsh condition such as high pressure and temperature as well as strong acid and base which will deteriorate electrical properties of conjugated polymers. They were only possible to fabricate P3HT nanopillars with limited feature-size and geometry.

The procedure to fabricate nanostructures of conjugated polymers, based on the soft molding pattern transfer, is illustrated in Figure 1a. Polyfluoropolyether (PFPE) replica molds with hexagonal nanopores were prepared using a two-step replication process from an AAO template.^{46 81} By changing the anodization conditions of AAO, we could easily control diameter, height and geometry of AAO templates. The various geometries of nanostructures were transferred to a target substrate after filling up the nanopores of PFPE replica molds with conjugated polymer solutions by spin-casting as shown in Figure 2.3.2. We note that the transfer process is possible at low temperature (60 °C) and low pressure (~ 4 bar) because of low surface energy properties of PFPE molds. Moreover, more than 500 replicas could be fabricated from 1 AAO templates. The uniform size of nanostructures in large area were verified by the scanning electron microscopy image and GISAXS results (Figure 2.3.1.b)).

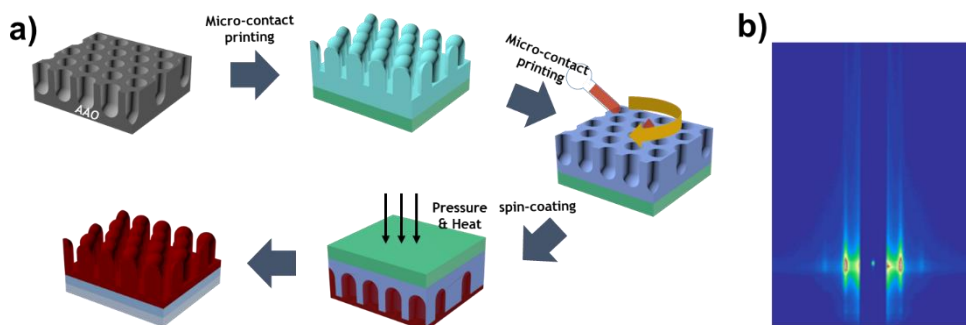


Figure 2.3.1. a) A schematic illustration for the procedure to fabricate nanopillars of conjugated polymers. b) GISAXS 2D results which measured P3HT nanopillars.

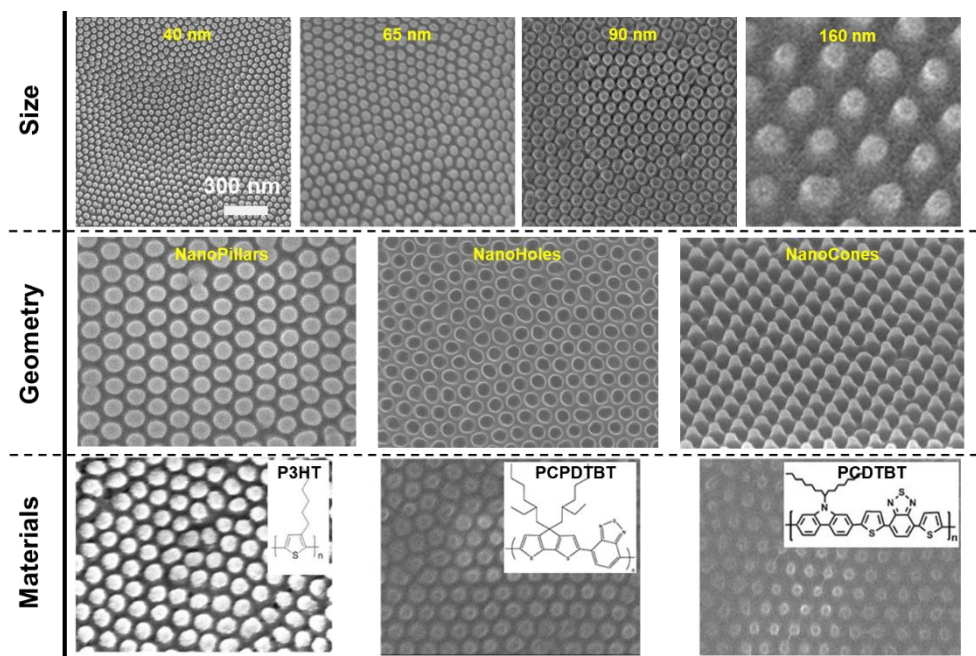


Figure 2.3.2. SEM top images of conjugated polymer nanostructures changing various parameters (size, geometry, and materials).

2.3.2. Nanoconfinement effects on crystalline structures by the size of nanostructures

Systematic studies on the effects of nanoconfinement on structural properties of conjugated polymers were performed by changing diameters of nanopillars. The diameter sizes of 45nm, 60nm, 100nm, 170 nm nanopillars made of PCDTBT, PTB7-th and P3HT were used for this study as shown in Figure 2.3.2. Grazing incidence wide angle X-ray scattering was performed to characterize crystalline structure and orientation of polymers in nanopillars. As the degree of confinement becomes larger, (diameters of nanopillars become smaller) the crystallinity of confined molecules was highly increased, which is indicated by the strong π - π staking peaks as shown in Figure 2.3.3. Semi-crystalline polymer (P3HT) as well as amorphous polymers (PCDTBT, PTB7-th) have shown nanoconfinement effects. Their crystallinity was much higher than bulk films which are thermally heated or additive added.

Semicrystalline polymers, P3HT has shown dominant face-on orientation as previously reported.^{42, 44, 48, 50, 53, 66, 67, 70} In the case of amorphous low bandgap polymer, PCDTBT and PTB7, their crystallinity corresponding to face-on orientation were highly increased by nanoconfinement as shown in Figure 2.3.3. Especially, PTB7-th showed higher population of crystalline structures than P3HT when it is highly confined (40 nm pillars) even though the size of crystal is smaller than P3HT. Those highly dominant face-on orientation by nanoconfinement will be beneficial for charge transport along vertical direction.

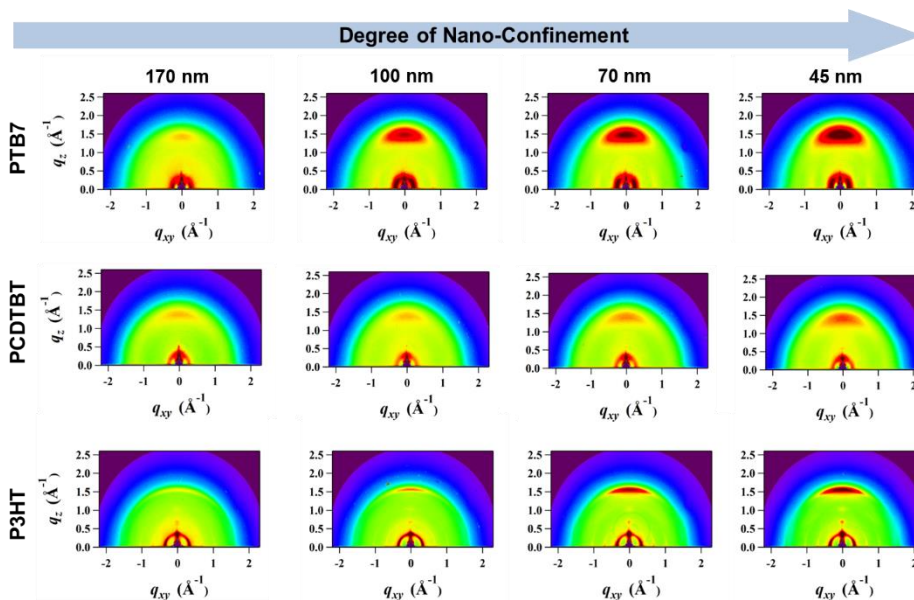


Figure 2.3.3. GIWAXS 2D results measured different size of nanopillars using different kinds of conjugated polymers.

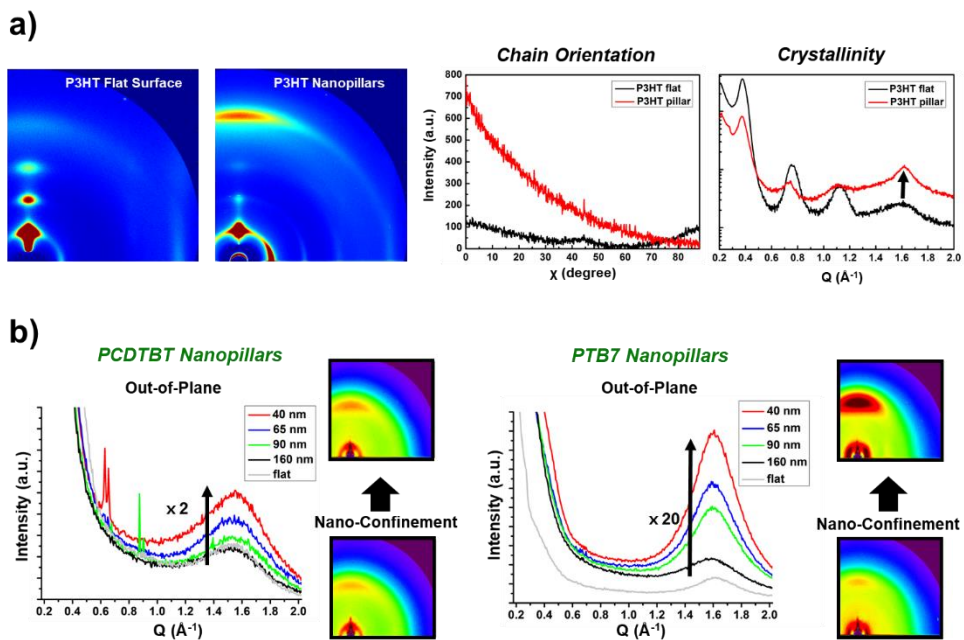


Figure 2.3.4. a) GIWAXS 2D results and 1D profiles of P3HT flat films and P3HT nanopillars. b) Line cuts along out-of-plane direction of PCDTBT nanopillars and PTB7 nanopillars

2.3.3. Nanoconfinement effects on crystalline structures by the geometry of nanostructures

We also studied the effect geometry of nanostructures on nanoconfinement effect. For this study, we measured GIWAXS at different incidence angles. By changing the incidence angle of x-ray beam, we can control the penetration depth of x-ray beams. We ranged the incidence angles from 0.11° to 0.15° to measure crystalline structures of surface structures as well as internal structures of nanostructured conjugated polymers. At the incidence angle of 0.11° , X-ray beams only penetrate surfaces of the films so that we can measure surface nanostructures of the samples. At the critical angle of 0.13° , penetration depth of X-ray beams was increased up to full penetration depth of samples and crystalline structures in top layer and inner layer were measured. As the incidence angles were increased above critical angles, X-rays penetrated further into silicon substrates mainly revealing information of inner layer of samples.⁸²⁻⁸⁴

We compared two geometries of nanostructures, nanopillars and nanocones of PTB7. We calculated ratio of (010) peak intensity to (100) peak intensity to estimate relative face-on crystalline populations at each incidence angle since scattering volume becomes smaller as the incidence angles become smaller. As can be seen in this Figure 2.3.6., nanopillars which have constant nanoconfinement along vertical direction, the (010)/(100) ratio showed similar values at different incidence angles. However, in the case of nanocones, the calculated ratio was increased as incidence angles smaller because of strong confinement at the edge of nanocones, which verifies nanoconfinements effects on conjugated polymers

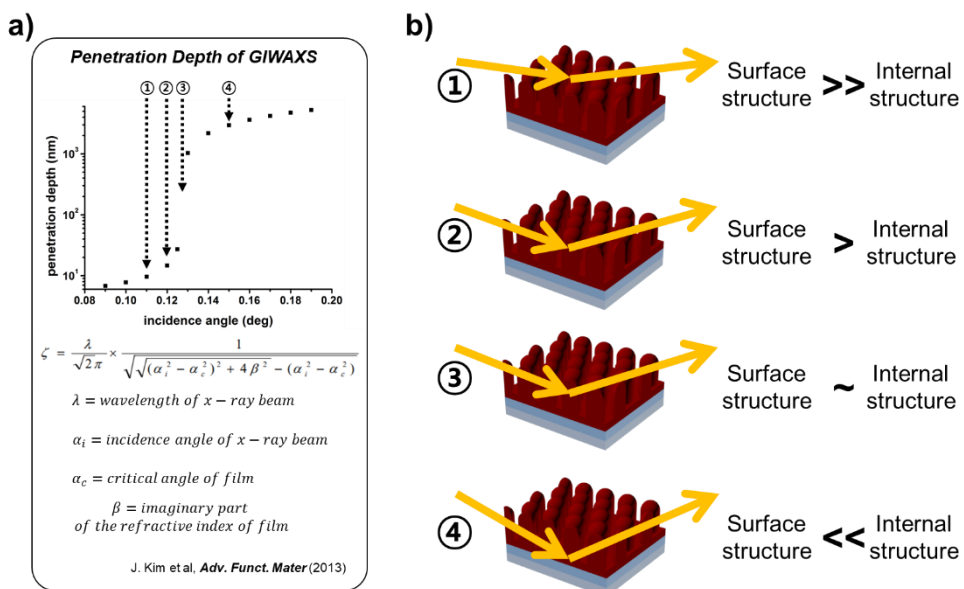


Figure 2.3.5. a) Calculated penetration depth of X-ray beams at different incidence angles. b) Schematic illustrations of penetration of X-ray beams at difference incidence angles

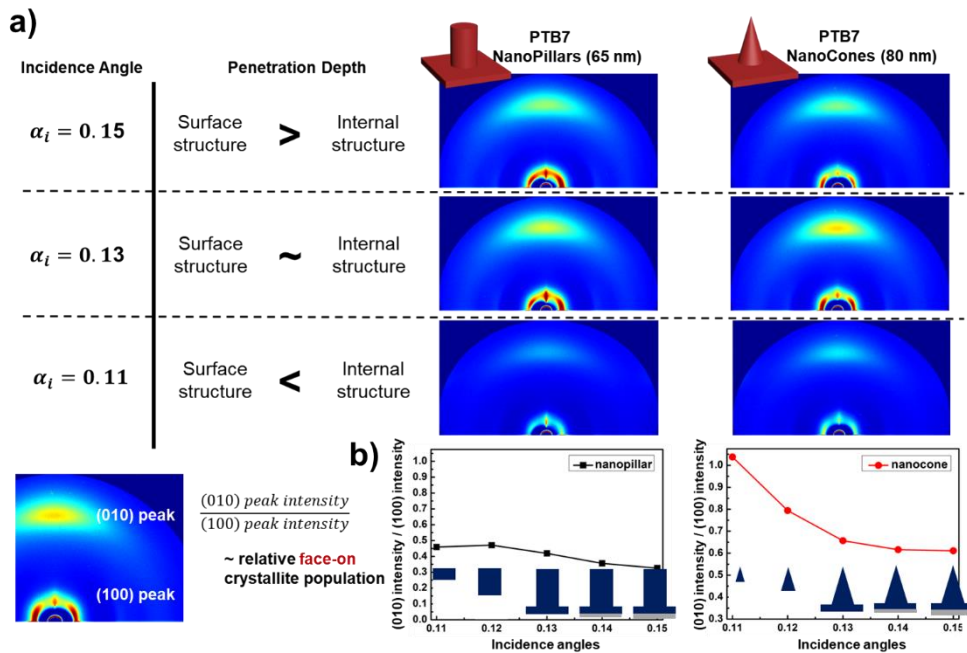


Figure 2.3.6. a) GIWAXS 2D results of PTB7 nanopillars and nanocones which were measured at different incidence angles. b) Calculated ratios of (010) peak intensity to (100) peak intensity of PTB7 nanopillars and PTB7 nanocones at different incidence angles.

2.3.4. Electrical doping on nanostructured conjugated polymers

To obtain better electrical properties, we tried to dope on these nanostructured conjugated polymers. The first effective method of solution based electrical doping on conjugated polymers were recently introduced.⁷⁸ They reported more efficient and stable OPV devices attribute to increased conductivity, good contacts as well as enhanced oxidization resistance by using this solution based electrical doping method. We used the same process methods on our system. Immersing the P3HT and PTB7 nanopillars in PMA nitromethane solution, nanopillars were electrically doped about 10 nm from the surfaces as depicted in Figure 2.3.6.(a). Doping of inorganic materials into organic materials showed brighter top images of nanopillars and higher intensities of edges parts of nanopillars in cross-section image as shown in Figure 2.3.7 (b) because of higher electron density of doping materials (Mo in PMA). Constant peak intensities of Mo in depth profiling of XPS supports that nanopillars were successfully doped by solution process.

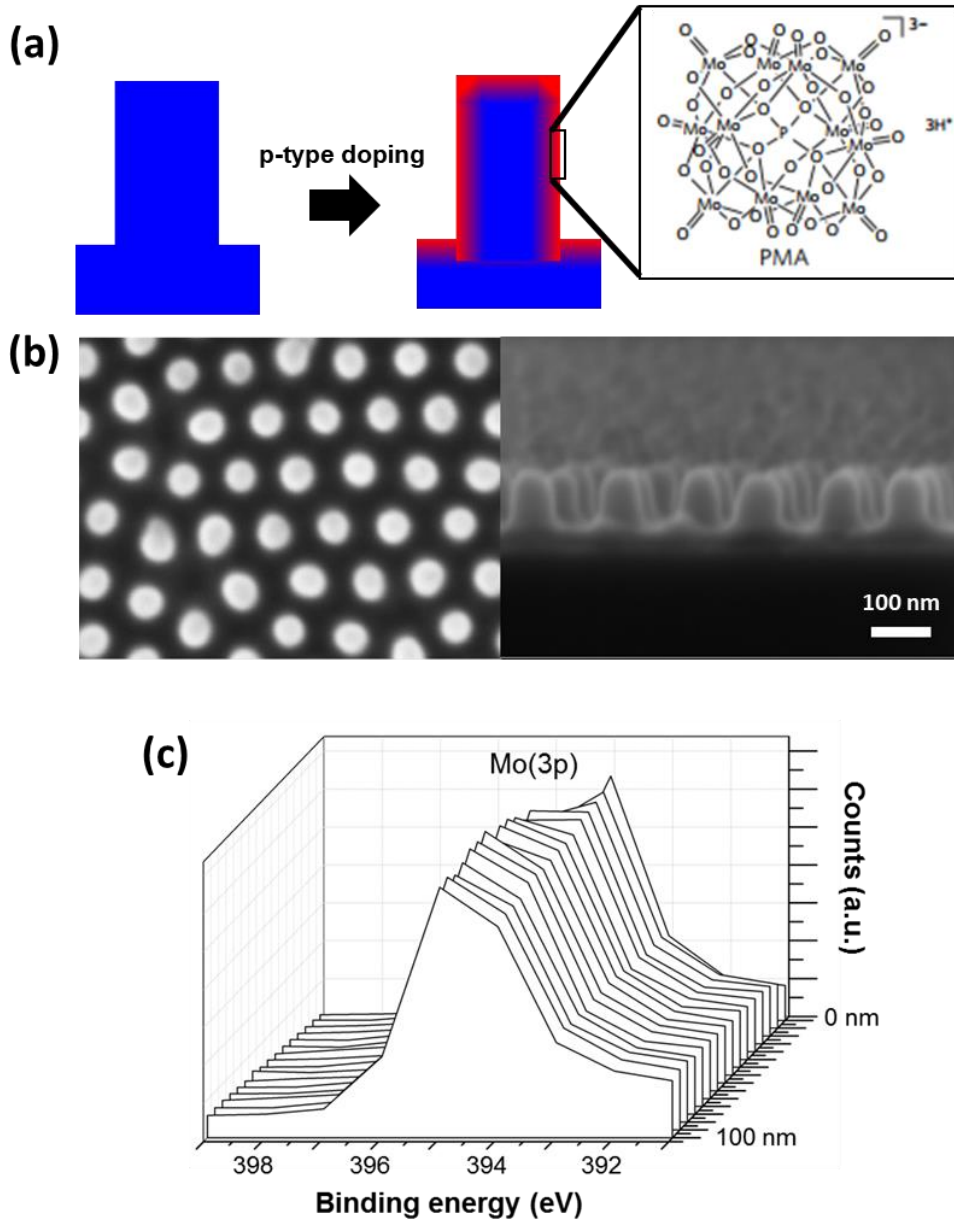


Figure 2.3.7. (a) Schematics of electrically-doped nanopillars by PMA molecules. (b) SEM top and cross-section images of electrically-doped nanopillars and (c) XPS depth profiling of electrically-doped nanopillars.

2.3.5. Enhanced optical and electrical properties by nanoconfinement effects

To elucidate the effect of nanoconfinement and electrical doping on electrical property, we measured macro-scale electrical properties of nanopillars. In the previous study, they characterized charge mobilities of P3HT micropillars and nanopillars by using gold coated elastomer PCBM for conformal contacts of top parts of P3HT pillars with electrodes.^{70, 85} We employed gold coated thin PET films to have good contacts with top parts of the nanopillars as well as prevent destruction of gold films by buckling of PCBM during pressing procedures as shown in Figure 2.3.8.(a). Both PTB7 and P3HT nanopillars have shown more than two magnitudes higher charge mobility along vertical direction by nanoconfinement effects. In addition, the doped nanopillars showed additional 2 or 3 times increased charge mobilities than non-doped samples as shown in Figure 2.3.8.(c) and (d). Nanostructured conjugated polymers are more vulnerable to oxidization because of large surface area as shown in Figure 2.3.8.(d). However electrical doping on nanopillars dramatically increased oxidization stability when they are exposed to air.

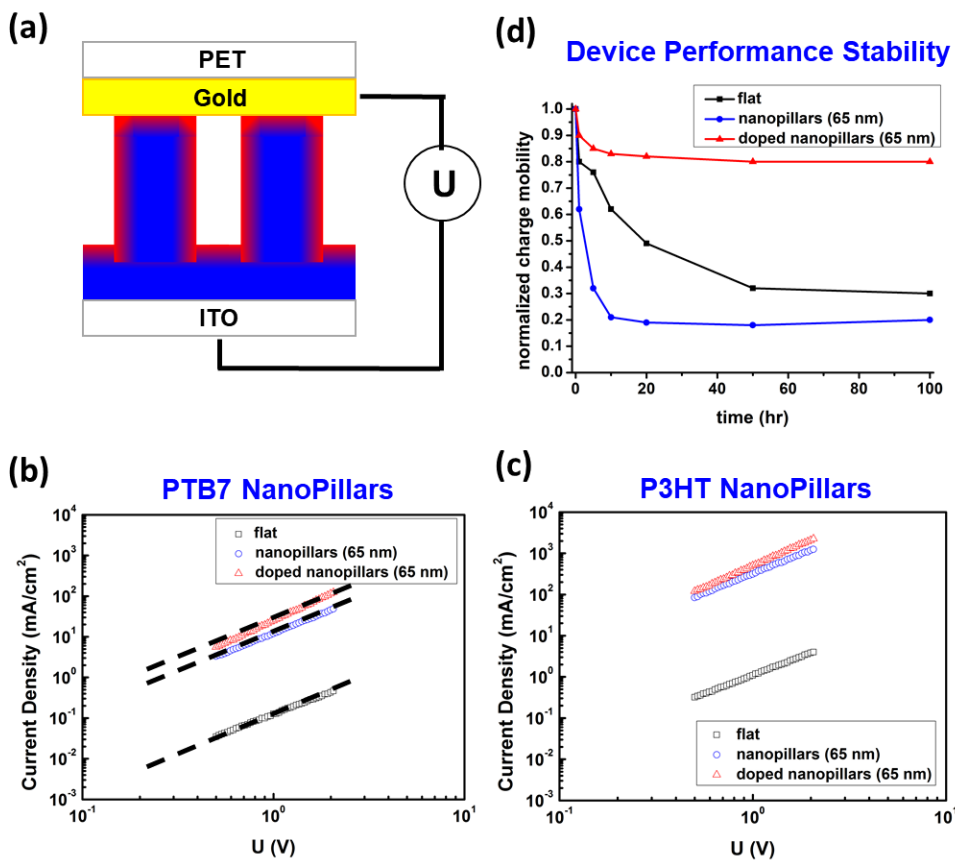


Figure 2.3.8. (a) Schematics of method for measuring charge mobilities of nanostructured samples. Log-log plots of current density of (b) PTB7 and (c) P3HT. (d) Normalized charge mobilities of samples when they are exposed in air up to 100 hours.

2.4. Conclusion

We conducted systematic studies on the effect of nanoconfinements on structural and electrical properties of conjugated polymers based on our simple patterning methods which we call it as residual-solvent assisted pattern transfer method. GIWAXS studies on different feature size and geometry of conjugated polymer nanostructures show the dramatic effect of nanoconfinements on crystalline structures of polymers. More than 20 times higher population of crystallites having face-on orientation were obtained by nanoconfinement effect. In addition, they have shown more than two magnitudes higher charge mobility along vertical direction by increased crystallinity. Moreover, doping on those nanostructured films further increased the conductivity 400 ~ 500 times higher than that of bulk film. We are convinced that nanoconfinement along with electrical doping could be widely extended to other conjugated polymer for the varied application of optoelectronics.

Chapter 3. Unusual Dynamics of Conjugated Polymers by Nanoconfined Geometry for Stabilized Nanomorphology

3.1. Introduction

Development of new donor and acceptor materials and controlling nano-morphology lead to more than 12 % power conversion efficiency close to commercialization. However, intrinsic drawbacks of organic materials are still limiting factors for high device performance and long term stability as described in Chapter 1. Especially, poor stability is a major limiting factor for commercialization and there lacks the studies on the stability of organic solar cells. Because of their metastable nanostructures in bulk heterojunction geometry, little heat makes organic materials to be mobile and destroy tens-of-nanometer domains. It is essential to induce favorable nanomorphologies which are thermally stable to realize stable and efficient organic solar cells.

There were previous studies on diffusion of PCBM electron acceptor.⁸⁶⁻⁸⁸ Since PCBM fullerene derivatives are small molecules, the rate of diffusion was so fast that they diffused into all the films in a few seconds. And aggregation of PCBM by heat is the one of the main reason of poor stability in BHJ. It is important to suppress diffusion of PCBM for stable nanomorphology.⁸⁹⁻⁹¹

In this chapter, two examples of nanoconfined geometry in organic solar cell will be shown to realize efficient and stable performance. First, we used nanowire network structures in bulk heterojunction as confinement geometry. we demonstrate a novel strategy for the stabilization of nanomorphology of organic solar cells by

inducing polymeric nanowire network structures. Thermal annealing of poly(3-hexylthiophene-2,5-diyl) (P3HT) nanowires, highly crystalline, 1-dimensional structures held together through interchain π - π stacking, led to the formation of nanowire network structures confirmed through small angle neutron scattering (SANS) measurements. The physically interconnected network structures form robust electron donor domains and impose confinement which suppresses the aggregation of the electron acceptor, [6,6]-phenyl-C61-butylic acid methyl ester (PCBM). Organic solar cells having the nanowire network structures showed increased power conversion efficiencies and dramatically enhanced thermal stability compared to BHJ and non-network nanowire-based devices. Furthermore, the performance of the nanowire network-based devices were inversely related to the size of the networks, attesting to the significance of nanoconfined geometry formed within nanowire network structures.

Second geometry is quasi-OHJ fabricated by sequential process. For this study, we used PTB7 and PCBM. PTB7 were first deposited on substrate. PCBM dissolved in DCM/DIM were deposited by spin-casting on top of PTB7 films. During the spin-coating process, some PCBM were diffused into PTB7 amorphous phases forming interdigitated structures at the interfaces. They showed significantly enhanced device stability due to interdigitated structures, which are confined geometry at the interfaces. Compared to performance of BHJs were deteriorated within initial 10 hours, other nanoconfined devices showed stable performance more than 1000 hours when it is annealed at 85 °C. In addition, we could obtain PCE close to BHJ's by changing the solvents for PTB7 depositions.

3.2. Nanoconfined Geometry by Polymeric Nanowire Network Structures in Bulk Heterojunction Solar Cells

Polymer nanowires, which are well-defined, 1-dimensional crystalline assemblies, have much higher crystallinity and enhanced charge mobility compared to amorphous aggregates or fibril deposited films.^{92, 93} Solution-based nanofiber formation makes it possible to develop structural order prior to film deposition, allowing for enhanced charge mobility. Inducing polymer nanowire formation using P3HT, a well-known semicrystalline conducting polymer, has been shown to enhance the performance and oxidization stability of OTFTs⁹²⁻⁹⁶ and OPVs⁹⁷⁻¹⁰⁵. Recently, this approach has been extended to low bandgap polymers, leading to OPVs having more than 10 % power conversion efficiency.¹⁰³ However, systematic studies to control and characterize the 3-dimensional assemblies of the nanowires inside the active layers of organic electronic devices are scarce. Detailed investigations could give us an insight for enhanced device performance and stability. In this study, we report a simple strategy for the formation of network structures of P3HT nanowires in P3HT nanowire:PCBM blend films. The stable nanowire network structures could be induced by thermal annealing, and significantly improved charge transport along the vertical direction was observed. Devices containing the network structures obtained using this method maintain their power conversion efficiencies even during operation at 120 °C. Grazing incidence wide angle X-ray scattering (GIWAXS) and small angle neutron scattering (SANS) measurements were conducted to analyze the three-dimensional network structures of nanowires previously not investigated at the ensemble scale.

The influence of the network structures on the nanoscale morphologies,

electrical properties, performance, and thermal stability of the OPVs is also systematically evaluated. Compared to the typical, non-network structures, highly enhanced electrical properties, device performance, and stability were obtained. The device performance, in particular, was strongly dependent on the characteristic lengths of network structures, with decreasing characteristic lengths leading to increasing device performance. The observation is attributed to better balanced charge mobilities as well as smaller PCBM domain sizes.

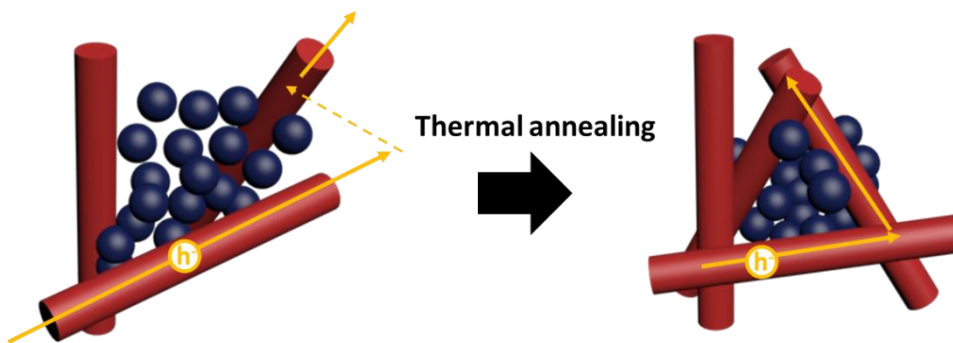


Figure 3.2.1. Schematic of transition from P3HT nanowires to nanowire network structures by thermal annealing

3.2.1. Experimental

Materials & preparation of films P3HT (4002-EE) was purchased from Rieke Metals Inc. and PC60BM was purchased from Nano-C Inc.. PEDOT:PSS (CLEVIOS™ P VP AI 4083) was purchased from Heraeus Deutschland GmbH & Co. KG. Chlorobenzene (anhydrous, 99.8%), 2-chlorophenol ($\geq 99\%$), and cyclohexanone (99%) were purchased from Sigma-Aldrich Co. Ltd.

P3HT:PCBM (1:1.5 wt% ratio) were dissolved in CB with total concentration of 35 mg/mL and stirred for 3 hours at 30 °C. 50 vol % of additives such as CHN and 2CP was slowly injected to P3HT:PCBM blend solutions at a rate of 12 ml/h. Then, solutions was additionally stirred more than 12 hours at 30 °C. Thin-films of reference (P3HT:PCBM blends without additives), CHN-added, and 2CP-added solutions were prepared by spin-coating at 2,000 rpm.

Characterization P3HT:PCBM blend films were characterized by UV-Vis absorption, AFM, GIWAXS and SANS. The absorption spectra were obtained using PerkinElmer Lambda 35 Ultraviolet-Visible (UV-Vis) spectrophotometer. AFM measurements were conducted using JPK Nanowizard 3. Height and phase images were taken after soaking the samples in cyhexane for 30 minutes. GIWAXS was performed at the 3C and 9A Beamlines of the Pohang Accelerator Laboratory (PAL). We used X-ray with a wavelength of $\lambda = 1.114 \text{ \AA}$ and an incident angle of 0.14° . SANS was conducted at the High-flux Advanced Neutron Application Reactor (HANARO) of the Korea Atomic Energy Research Institute (KAERI) in Daejeon, Korea. An incident neutron wavelength of 6 \AA with $\Delta\lambda/\lambda = 0.12$ was used. In addition, multiple sample to detector distances, 1.16 m, 6.7 m, and 17 m were used for the measurements. P3HT:PCBM films were prepared on quartz glass and 16 films were

stacked to obtain enough intensity for each measurement.

Device Fabrication Indium tin oxide (ITO)-coated glass substrates were ultrasonicated in acetone, isopropyl alcohol, and deionized water for 15 minutes each, and dried overnight in an oven. After treating the substrates with ultraviolet-ozone (UVO) for 15 minutes, PEDOT:PSS was then spin-coated at 4000 rpm for 40 sec. The coated samples were dried at 120 °C for more than 30 min. P3HT:PCBM blend solutions were spin-coated at 2,000 rpm and taken into high-vacuum chamber to eliminate residual solvent. LiF and Al layers deposited to the thickness of 0.5 nm and 100 nm, respectively, by thermal chemical vapor deposition with the active areas of the solar cells to be 9 mm². The devices were thermally annealed at 80 °C, 120 °C, and 150 °C for 20 minutes in nitrogen atmosphere. The J-V characteristics were obtained under AM 1.5 G condition with an intensity of 100 mw/cm² using Keithley SMU237 and a solar simulator (Newport 91160A).

3.2.2. Results and Discussion

The P3HT nanowires used in this study were prepared using either cyclohexanone (CHN) or 2-chlorophenol (2CP) as additive. Both CHN and 2CP have marginal solubility toward P3HT while showing a stark contrast in solubility of PCBM (23.6 mg/ml in CHN and 112.0 mg/ml in 2CP). The treatment of P3HT:PCBM blend solutions with additives allowed for the variation of the length of P3HT nanowires in the solution state. The additives were chosen since they have similar boiling points. To minimize the thickness variation in devices prepared from blend solutions having different additives, solutions were stirred for more than 12 hours at 30 °C were spin-coated at 2,000 rpm. Three films, the reference (without additives), CHN added, and 2CP added, all showed the thickness of 180 nm.

Figure 3.3.2. shows the UV-Vis absorption spectra of P3HT:PCBM blend films prepared using CHN and 2CP. The absorption feature around 333 nm was attributed to PCBM, and the broad absorption from 400 nm to 650 nm was assigned to P3HT. Both blend film samples showed well-defined vibronic structures at 545 and 600 nm, suggesting the formation of highly ordered P3HT structures. Upon thermal annealing at 80 °C, 120 °C and 150 °C, the P3HT absorption band increased in intensity. However, the PCBM peaks were significantly decreased when the annealing was conducted at 150 °C, presumably due to the disassembly of PCBM agglomerates.

To obtain real space images of the samples, AFM measurements were performed. Figure 2 shows the AFM phase images after the treatment of the blend films with cyclohexane to remove the PCBM overlayers.^{106, 107} Images of films obtained from solutions containing CHN and 2CP clearly showed the presence of P3HT nanowires. The use of CHN additive gave longer nanowires. However, no

distinct changes were observed in phase and height images, regardless of the annealing temperature.

GIWAXS was employed to analyze the crystalline structures of samples. Figure 3.2.4. shows the two-dimensional scattering patterns of each sample. The strong peak intensities at the position of (010) along the in-plane direction and of (100) along the out-of-plane directions indicate the formation of highly ordered P3HT structures. The (100) peak from the CHN added samples showed strongly enhanced intensity (Figure 3.2.4. i and j), indicating the formation of longer nanowires by CHN, consistent with AFM results. Polar scattering profiles were obtained at the (100) peak to evaluate the relative orientation of nanowires (Figure 3.2.4. k and l). Intensities of CHN added samples were more drastically decreased as azimuthal angles were increased from 90° to 180° than those of 2CP added samples, implying that a greater fraction of nanowires were lying horizontally in the CHN added films, likely due to the greater nanowire length, than in the 2CP added samples.

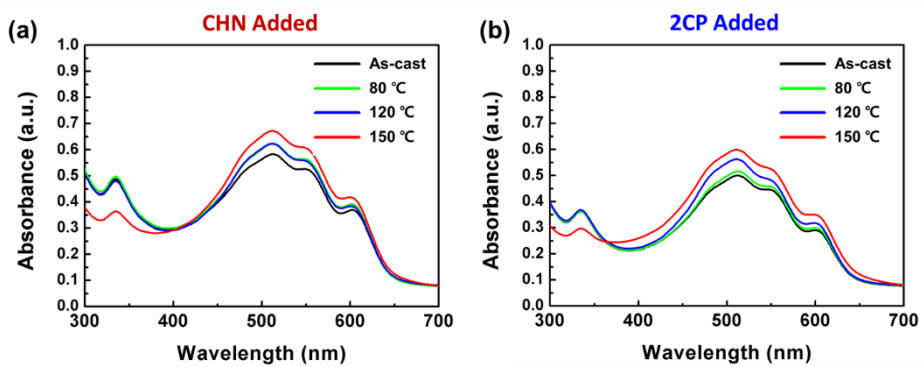


Figure 3.2.2. UV-Vis absorption spectra of P3HT:PCBM blend films prepared from blend solutions added with (a) CHN and (b) 2CP at different annealing conditions

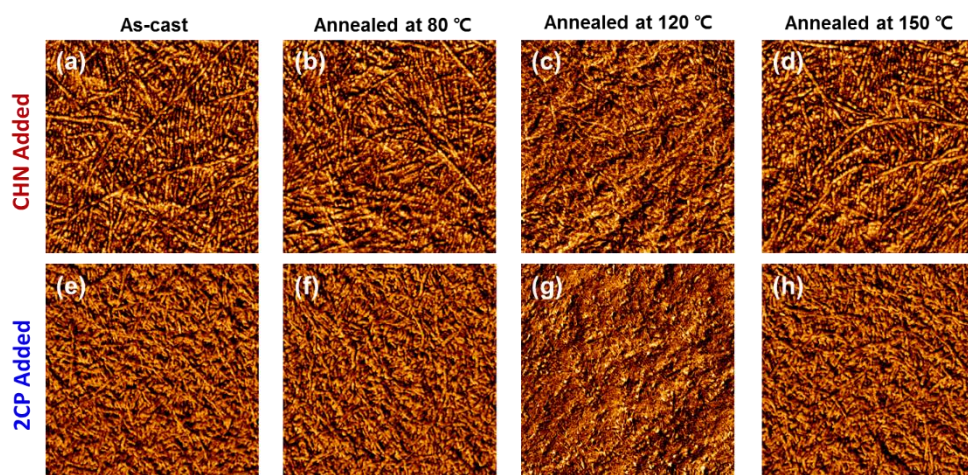


Figure 3.2.3. AFM phase images of top PCBM over layer removed P3HT:PCBM blend films spin-coated from blend solution added with (a) ~ (d) cyclohexanone and (e) ~ (h) 2-chlorophenol with different annealing conditions

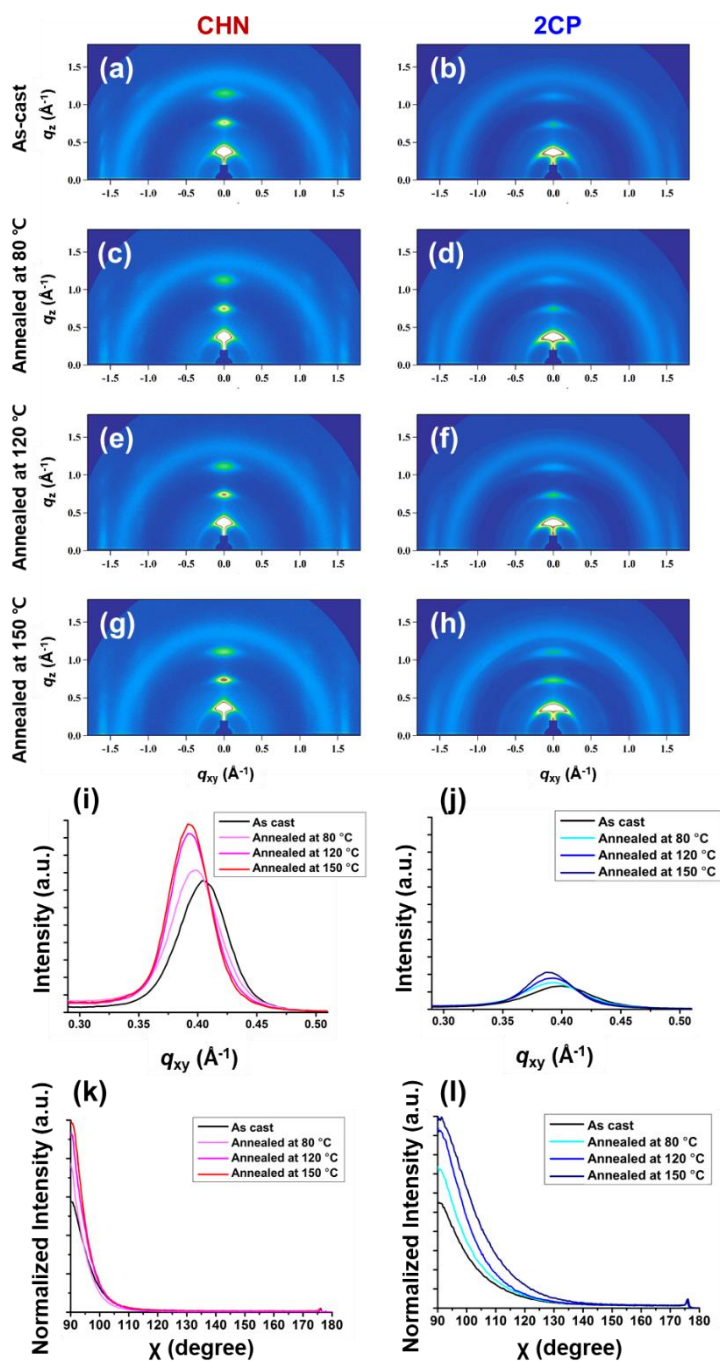


Figure 3.2.4. Two dimensional GIWAXS patterns of P3HT:PCBM blend films prepared from blend solutions added with (a), (c), (e), (g) CHN and (b), (d), (f), (h) 2CP at different annealing conditions. Line cuts along horizontal directions and angular cuts from 2D GIWAXS patterns of (i), (k) CHN added samples and (j), (l) 2CP added samples

The three-dimensional structures of the blend films were probed by SANS. The thermal transition of P3HT nanowires to nanowire network structures, along with the influence of the nanowire network formation on the PCBM phases were investigated by comparing the SANS results of as-cast films with those annealed at various temperatures. Figure 3.2.5. shows the corresponding SANS profiles. Samples prepared using additives showed a Q^{-1} behavior at the medium q range, revealing the existence of isolated rigid rods (nanowires) of P3HT.¹⁰⁷⁻¹⁰⁹ Upon thermal annealing at 80 °C and 120 °C, no changes were observed at the low q region for both CHN and 2CP added samples, suggesting no significant changes in the aggregated structures of the nanowires. In films annealed at 150 °C, which is above the glass transition temperature of P3HT, the SANS profiles followed the power law of $Q^{-2\sim 3}$, implying the formation of nanowire network structures.¹⁰⁷⁻¹¹² The average mesh sizes of network fabricated by using CHN and 2CP were 48.3 nm and 34.9 nm, respectively, which could be deduced from the crossover points of isolated rigid rod (Q^{-1}) to network behaviour ($Q^{-2\sim 3}$). Shorter nanowires formed network structures with shorter characteristic lengths. At higher Q regions, poly hard sphere model was employed to quantify the sizes of PCBM.¹¹³ The SLD values of P3HT and PCBM ($0.7 \times 10^{-6} \text{ \AA}^2$ and $3.6 \times 10^{-6} \text{ \AA}^2$, respectively^{113, 114}) were used and their fitting curves and results are summarized in Figure 3.2.6., Figure 3.2.7, Table 3.2.1, and Table 3.2.2. Interestingly, the PCBM agglomerates appeared to have decomposed, with their sizes significantly decreased when the samples were annealed at 150 °C. The observation is consistent with the network structure formation of P3HT nanowires, which, in turn induced nanoconfined geometry to PCBM phases. As the characteristic lengths of network structures were decreased, the size of PCBM agglomerates were further reduced. This was attributed to the increased degree of

confinement. We hypothesize that shorter nanowires lead to more densely-formed network structures, giving higher degree of confined for PCBM domains. The smaller domain sizes form favorable morphology for solar cells. In addition, stabilized device performances were expected from the annealed samples due to robust nanowire network structures and suppression of the PCBM aggregations.

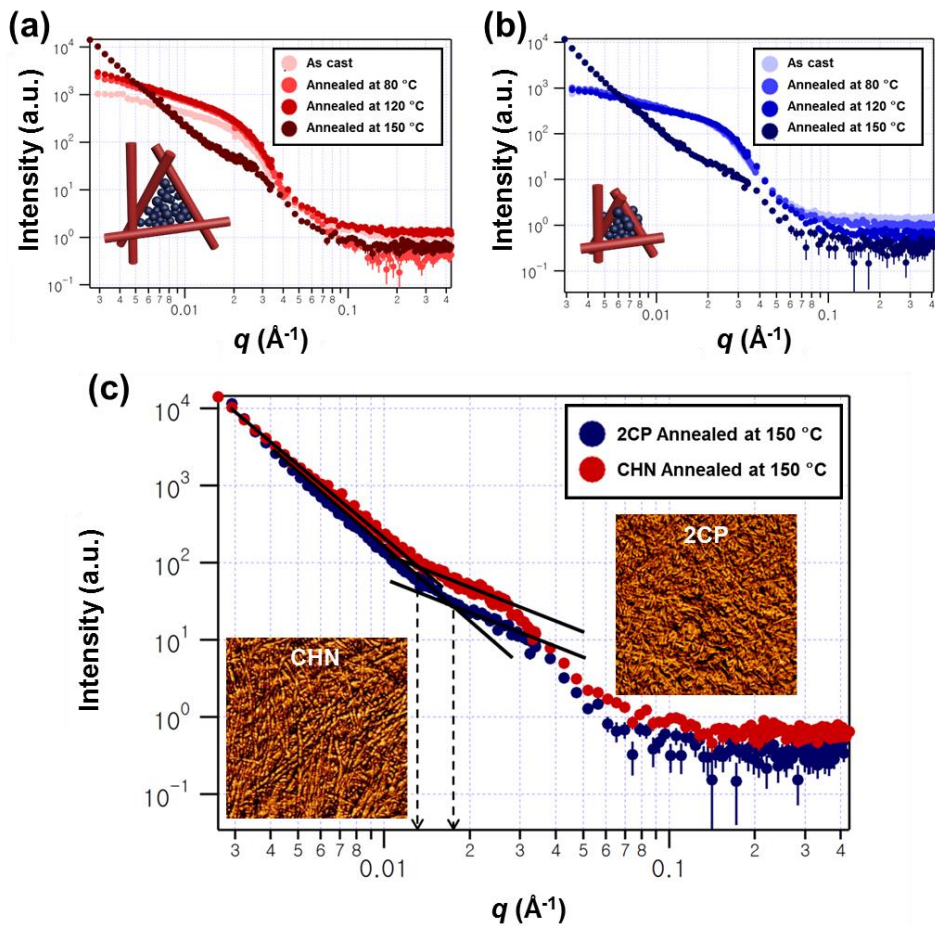


Figure 3.2.5. SANS profiles of P3HT:PCBM blend films prepared from (a) cyclohexanone added, (b) 2-chlorophenol added at different annealing conditions and (c) profiles of 2CP added samples and CHN added samples annealed at 150 °C for comparison of their network sizes

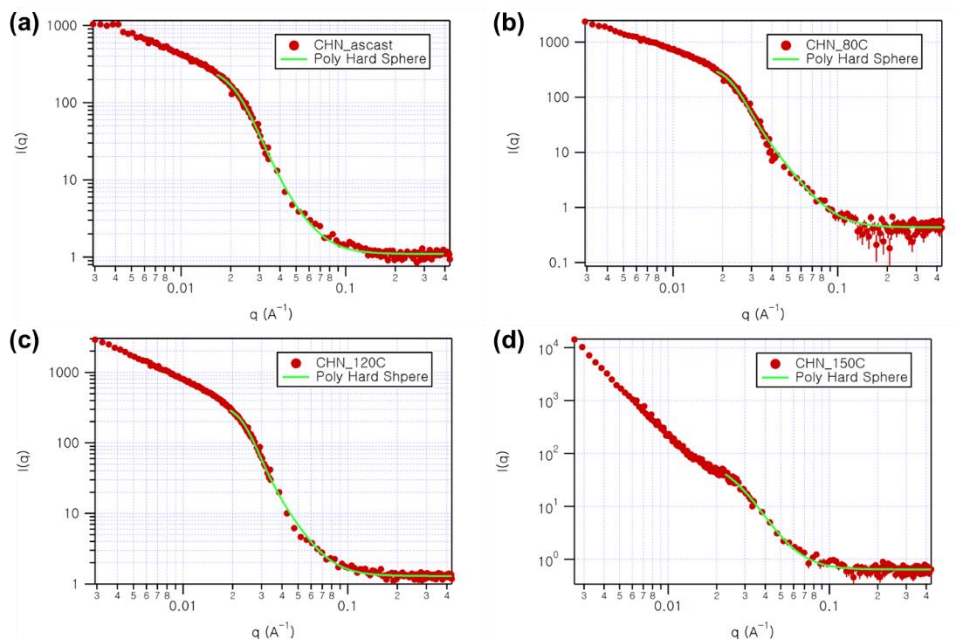


Figure 3.2.6. SANS profiles of P3HT:PCBM blend films (a) as cast and annealed at (b) 80 °C, (c) 120 °C, and (d) 150 °C prepared from blend solutions with cyclohexanone and their fitted curves.

Table 3.2.1. Summary of fitted results of Figure 3.2.6.

Fitting Parameters	As cast	80 °C	120 °C	150 °C
Radius (nm)	8.96	10.3	10.4	5.69
Polydispersity (%)	39.4	34.5	32.5	48.9
PCBM Agglomerates Vol %	24.5	31.2	32.8	15.8
PCBM Vol % in matrix	20.7	12.8	11	37.9

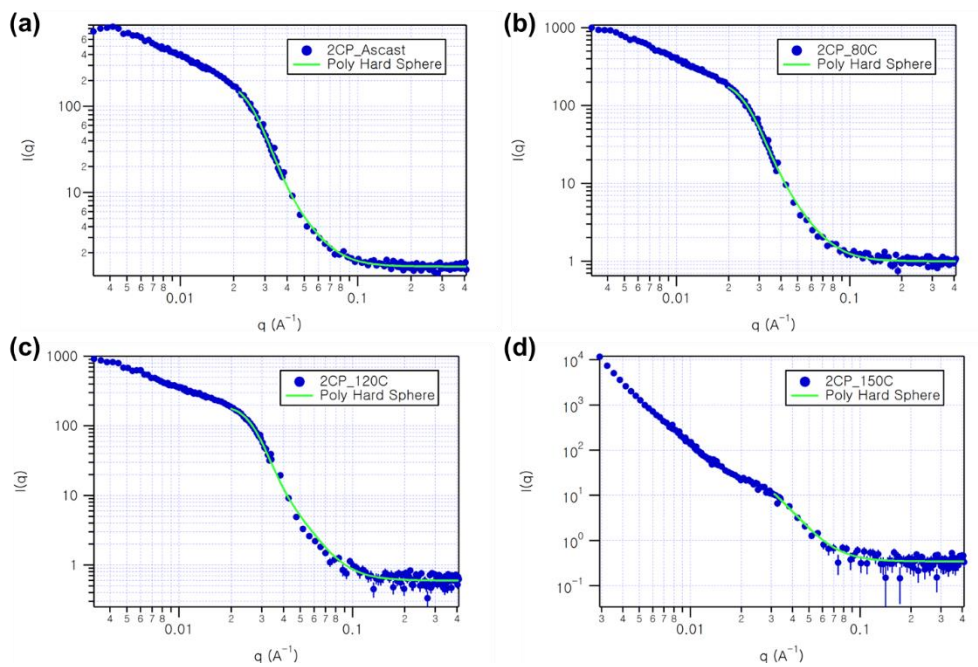


Figure 3.2.7. SANS profiles of P3HT:PCBM blend films (a) as cast and annealed at (b) 80 °C, (c) 120 °C, and (d) 150 °C prepared from blend solutions with 2-chlorophenol and their fitted curves.

Table 3.2.2. Summary of fitted results of Figure 3.2.6.

Fitting Parameters	As cast	80 °C	120 °C	150 °C
Radius (nm)	8.99	8.81	9.19	4.82
Polydispersity (%)	32.2	33.6	29.0	51.3
PCBM Agglomerates Vol %	24.9	25.6	26.6	9.19
PCBM Vol % in matrix	20.7	17.9	17.2	37.9

To examine the effect of nanowire network structures on the electrical properties, stability, and the performance of organic photovoltaic devices, solar cells with the configuration of ITO/PEDOT:PSS/P3HT:PCBM/LiF:Al were fabricated on glass substrates. The thickness of the active layers on all devices were kept at 180 nm. Before thermal annealing, CHN-based devices showed the highest power conversion efficiency followed by the 2CP-based devices and additive-free devices. The observation is attributed to the highly developed crystalline structures of the device from CHN as shown in Figure 3.2.8. and Figure 3.2.9. Those trends were kept until annealing up to 120 °C. Upon the thermal induction of nanowire networks, all devices showed highly increased device performance attributed to the increased J_{sc} . This is in agreement with the decreased PCBM domain sizes as well as increased electron and hole mobilities by nanowire network structures as shown in Table 3.2.5. Moreover, PCE of 2CP based devices were greater than that of CHN based devices, suggesting that the nanowire network structures composed of shorter nanowires are more effective for higher device performance.

Device properties in terms of stability were also measured by thermally aging at 120 °C under N_2 atmosphere. Devices with nanowire network structures showed significantly enhanced device stabilities, retaining more than 90 % of their initial PCE after exposure to 120 °C for more than 10 hours. However, PCE of non-treated and non-network devices deteriorated significantly, with less than 65 % of their highest values remaining after two hours of thermal treatment.

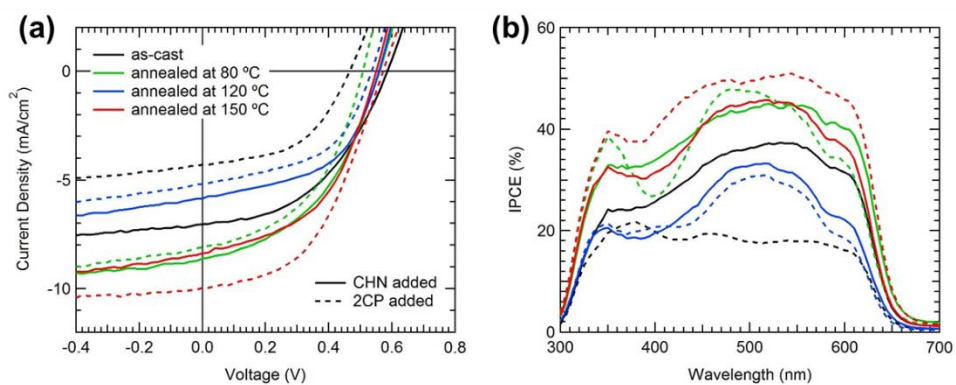


Figure 3.2.8. The current density-voltage characteristics of devices spin-coated from P3HT:PCBM blend solutions with different additives at different annealing conditions. a) J-V curve, b) IPCE of solar cells

Table 3.2.3. Summary of device performances with different additives and annealing conditions

Additives	CHN Added				2CP Added			
	as-cast	at 80 °C	at 120 °C	at 150 °C	as-cast	at 80 °C	at 120 °C	at 150 °C
J_{sc} (mA cm ⁻²)	7.03	8.63	5.86	8.37	4.30	8.08	5.18	9.96
V_{oc} (V)	0.59	0.56	0.56	0.55	0.47	0.51	0.54	0.57
FF (%)	46.26	44.65	51.74	48.89	49.94	46.89	51.02	47.75
PCE (%)	1.90	2.16	1.69	2.25	1.00	1.92	1.42	2.72

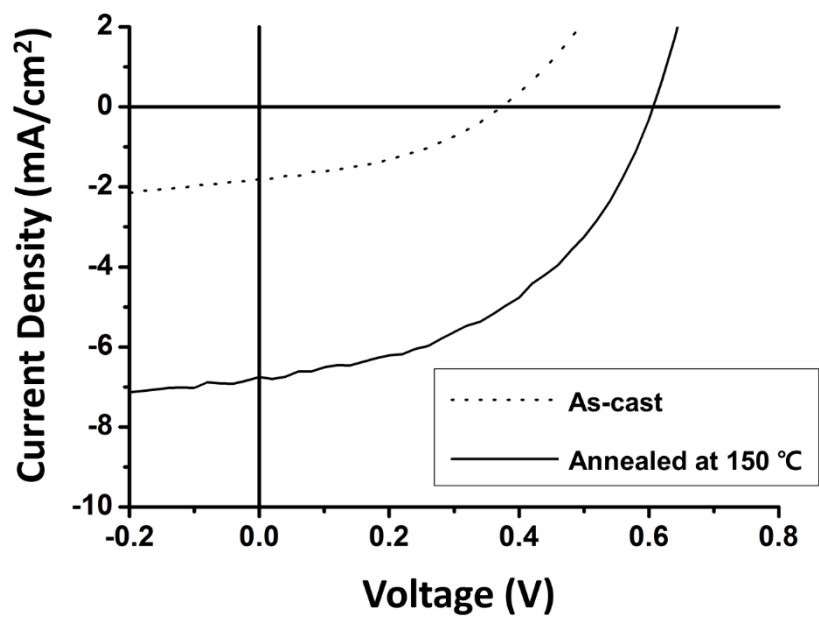


Figure 3.2.9. J-V characteristics of as cast and annealed at 150 °C P3HT:PCBM blend films without additives under simulated AM 1.5G solar illumination.

Table 3.2.4. Summary of device performance of P3HT:PCBM blend films without additives.

Conditions	As cast	150 °C
J _{sc} (mA cm ⁻²)	1.81	6.75
V _{oc} (V)	37.3	60.6
FF (%)	40.0	46.6
PCE (%)	0.288	1.91

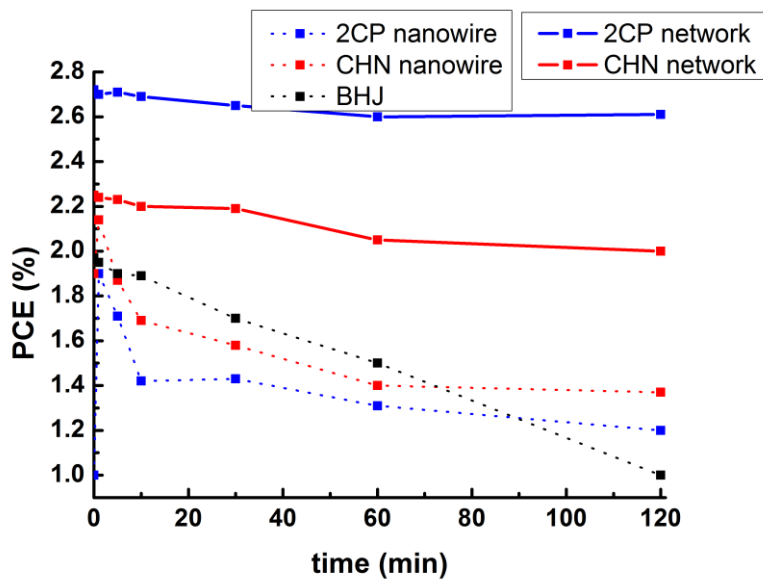


Figure 3.2.10. Stability curves of devices to compare the differences between non-additive and additives, network and non-network structures under continuous heating at 120 °C for 120 minutes

Table 3.2.5. Summary of fitted results of Figure 3.2.6.

	2CP (150 °C)	CHN (150 °C)	BHJ (150 °C)	2CP (non)	CHN (non)	BHJ (non)
Degree of Confinements	++ (34.9 nm)	+ (48.3 nm)	-	-	-	-
Radius (nm)	4.82	5.69	6.91	8.99	8.96	x
Hole Mobility ($10^{-5} \text{ cm}^2\text{V}^{-1}\text{s}^{-1}$)	241	203	9.72	96.1	143	1.23
Electron Mobility ($10^{-5} \text{ cm}^2\text{V}^{-1}\text{s}^{-1}$)	256	237	48.7	137	139	5.23
PCE (%)	2.72	2.25	1.91	1.00	1.90	0.288

3.3. Nanoconfined geometry by quasi-Ordered Heterojunction Solar Cells Fabricated by Sequential Process

In this study, we demonstrate an exhaustive study on the correlation between vertically-segmented crystallinity of photoactive layer and the performance of OSCs regarding PCE and thermal stability by employing sequentially processed layers. Some studies showed a little relevance or irrelevance of crystallinity and device performances owing to sole studies on properties of averaged bulk film.¹¹⁵ Vertical segmentation of active layers considering top and inner layers separately is important taking into account their efficient usage of photons absorbed at upper layer and interconnection between top and bottom layers. Since electron donor and acceptor were sequentially deposited, varying different boiling points of solvents could induce different crystalline structures along vertical direction due to different evaporation rates. On the basis of the conventional structure of ITO \ poly(3,4-ethylenedioxythiophene) polystyrene sulfonate (PEDOT:PSS) \ poly[4,8-bis(5-(2-ethylhexyl)thiophen-2-yl)benzo[1,2-b;4,5-b']dithiophene-2,6-diyl-alt-(4-(2-ethylhexyl)-3-fluorothieno[3,4-b]thiophene-)-2-carboxylate-2-6-diyl)] (PTB7-th) \ [6,6]-phenyl-C71-butyric acid methyl ester (PC₇₀BM) \ LiF \ Al, we varied the solvent of PTB7-th with identical thickness which resulted in considerably different performance. The top and inner layer crystallinity of thin films were measured through grazing-incidence wide-angle X-ray scattering (GIWAXS) changing the incident angles from 0.11° to 0.17°. The GIWAXS suggest that sequentially deposited layers showed much higher top layer crystallinity than BHJ. As a consequence, more charges are dissociated and transported from crystalline PTB7-th \ PC₇₀BM interface which lead to the increased short-circuit current (J_{SC}).

Moreover, compared to BHJ whose PCE deteriorated within initial 5 hours, sequentially processed films having high top layer crystallinity, showed superior stability retaining PCE above 3% after 1,000 hours of thermal degradation. On the other hand, the relative stability which was calculated by dividing from their initial PCE, showed contrary results, showing 90% stability for TCB, solvent with the highest boiling points revealing an invariant relation between crystallinity and thermal stability.

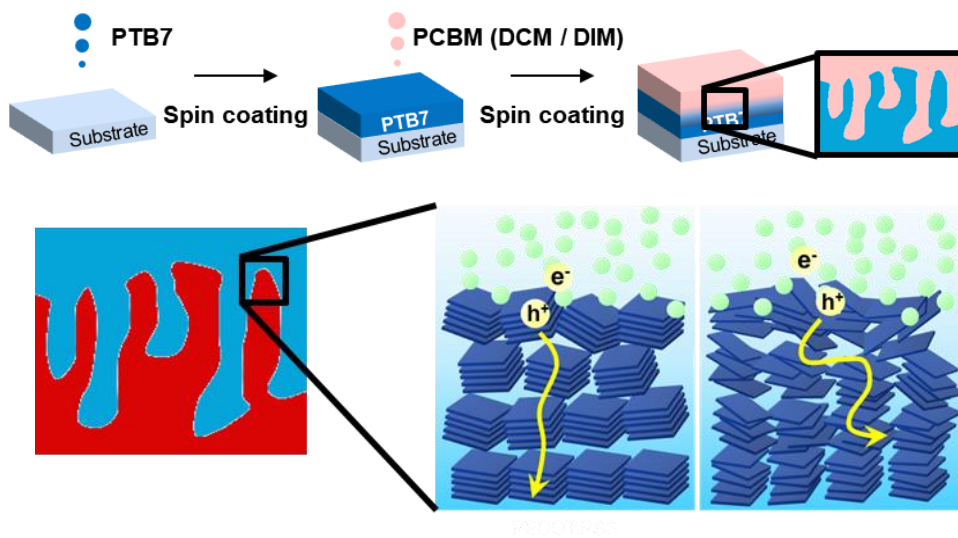


Figure 3.3.1. Schematic illustration of procedures and nanomorphology fabricated by sequential process

3.3.1. Experimental

Materials PEDOT:PSS (CLEVIOS™ P VP AI 4083) was purchased from Heraeus Deutschland GmbH & Co. KG. PTB7-th was purchased from Solarmer Energy Inc. and PC70BM (purity > 99% by nuclear magnetic resonance (NMR)) was purchased from One-Materials Inc. Acceptor additive DIM (purity > 99%) was purchased from Sigma-Aldrich Inc. Solvents, including CF, CB, DCB and TCB, were all purchased from Sigma-Aldrich Inc.

GIWAXS Measurements Details GIWAXS was performed at the 3C Beamline of the Pohang Accelerator Laboratory (PAL). All samples were prepared on Si wafer spin-casted by employing the same deposition conditions of fabricating organic solar cells devices. X-ray with a wavelength of $\lambda = 1.29 \text{ \AA}$ and incident angles varying from 0.11° to 0.17° were used for the measurements. Same exposure time was used for fair comparison.

Device Fabrication and Measurement OSCs were fabricated through following procedures. ITO glass was cleaned by sonication using acetone, IPA and DI consequently. After sonication, ultraviolet-ozone (UVO) surface treatment was conducted. Under ambient condition, PEDOT:PSS was spin-coated on the ITO glass followed by annealing at 120°C for 15 min. For BHJ device, photoactive layer solution consisting of PTB7-th:PC70BM (1:1.5 wt% ratio) solution dissolved in CB with total concentration 25 mg mL^{-1} was spin-coated above PEDOT:PSS surface at 1000 rpm for 60 sec. For sequentially processed devices, PTB7-th solution dissolved in CF (8 mg mL^{-1} , 2500 rpm), CB (15 mg mL^{-1} , 2500 rpm), DCB (18 mg mL^{-1} , 2000 rpm) and TCB (20 mg mL^{-1} , 2000 rpm) were spin-coated above the PEDOT:PSS layer with following annealing at 70°C for 10 min which formed similar thickness confirmed through the absorption spectra. Then, PC₇₀BM dissolved in DCM:DIM

(99:1 vol%) solution was spin-coated above the PTB7-th layer at 4000 rpm for 30 sec. After coating the photoactive layer, LiF (0.5 nm) and Al (100 nm) were thermally evaporated. For HOD fabrication, same fabrication methods were followed until PTB7-th layer. Afterwards, MoO₃ (10 nm) and Ag (100 nm) were sequentially evaporated. The J-V characteristics of OSCs were characterized using a source measurement (Tektronix Inc., Keithley 237) equipped with an AM 1.5 G solar simulator (Newport Corporation, 91160A). The IPCE spectra of devices were measured using an IPCE measurement system (Newport Corporation, QEPVSI-B).

3.3.2. Results and discussion

Crystalline structures in organic solar cells are crucial for good charge transport as well as stable nano-morphology. However, most of previous studies have only considered their bulk crystallinity, averaged crystallinity of overall films. Some results showed a little relevance or irrelevance between those bulk crystallinity and power conversion efficiency.¹¹⁵ Taking into account that transport of dissociated charges occurs vertically to each electrode, both top and inner layer crystallinity are a critical factor for high efficiencies and thermal stability. We could control crystallinity of top layer and underneath layer by varying boiling points of solvents of PTB7-th in sequential process. GIWAXS have been performed to elucidate the vertically-segmented crystallinity of thin films. Most previous studies have chosen incident angle of X-ray beams to be larger than the critical angle, only measuring bulk crystalline structures of thin films. In this study, we ranged the incidence angles from 0.11° to 0.17° to measure crystalline structures of top layer as well as underneath crystalline structures. At the incidence angle of 0.11° , X-ray beams only penetrate surfaces of the films so that we can measure surface nanostructures of the samples. At the critical angle of 0.13° ,¹¹⁶ penetration depth of X-ray beams were increased up to full penetration depth of samples and crystalline structures in top layer and inner layer were measured. As the incidence angles were increased above critical angles, X-rays penetrated further into silicon substrates mainly revealing information of inner layer of samples, which finally allow us to measure the vertically-segmented crystalline structures of the samples.⁸²⁻⁸⁴

PTB7-th only films have shown different top and inner layer crystallinity according to their boiling points of casting solvents as shown in Figure 3.3.2.

Pronounced scattering intensity at the (010) position of PTB7-th in out-of-plane direction is observed for all samples indicating dominant face-on orientation of crystallite, which corresponds with previous reports on the PTB7 system.^{90, 115, 117} From the intensity and angular cut at (010) position, we could compare the population of ordered polymers having preferential face-on orientation.¹¹⁸⁻¹²² Bulk crystallinity measured at 0.14° and 0.17° were similar or slightly decreased as the boiling points of solvents were increased. However, the difference becomes more distinct at the smaller incidence angle which corresponds to crystalline structure of top layer. As the boiling points of solvents were decreased, top layer crystallinity were significantly enhanced.

After deposition of PC₇₀BM dissolved in DCB and DIM, overall crystallinity of PTB7-th were decreased because of swelling of polymers during PC₇₀BM casting processes (Figure 3.3.3. and Figure 3.3.5.). Both top layer and underneath crystallinity in sequentially deposited samples showed similar trends with the results of PTB7-th only films. Especially, CF, the lowest boiling points has shown significantly enhanced crystalline structures in top layer suggesting importance of boiling points of casting solvents in sequential process. In addition, sequentially deposited samples showed much higher crystallinity in top layer compared to BHJ, which will be beneficial for stable and efficient performances. As discussed in the previous paragraphs, the reason of the highest characteristics of CF based on sequentially processed device is mainly attributed to the preferable crystalline structure of PTB7-th at the top layer. In addition, same characterizations were conducted on the PTB7-th \ PC₇₀BM layer without DIM in the PC₇₀BM solution which prevents excessive dissolution of underneath PTB7-th layer. Although the CF based sequentially deposited layer without DIM showed similar crystallinity in inner

layer, its top layer formed very poor crystallinity (Figure 3.3.4.). It resulted in low PCE of 1.557% which reinforces the importance of vertically-segmented crystallinity for the efficient OSCs.

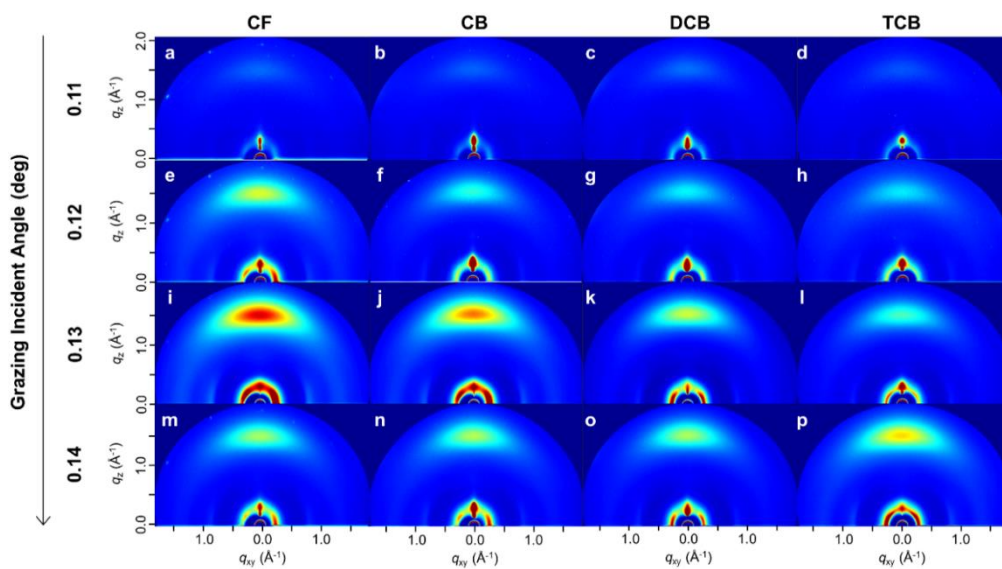


Figure 3.3.2. 2D Grazing-Incidence Wide-Angle X-ray Scattering (GIWAXS) patterns of PTB7-th depending on solvent and grazing incident angle.

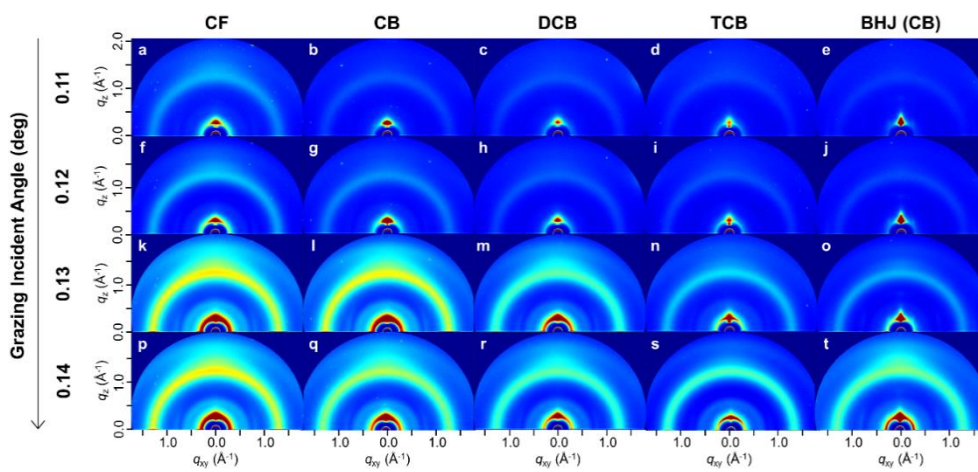


Figure 3.3.3. 2D Grazing-Incidence Wide-Angle X-ray Scattering (GIWAXS) patterns of PTB7-th \ PC70BM sequentially deposited layers depending on solvent and grazing incident angle.

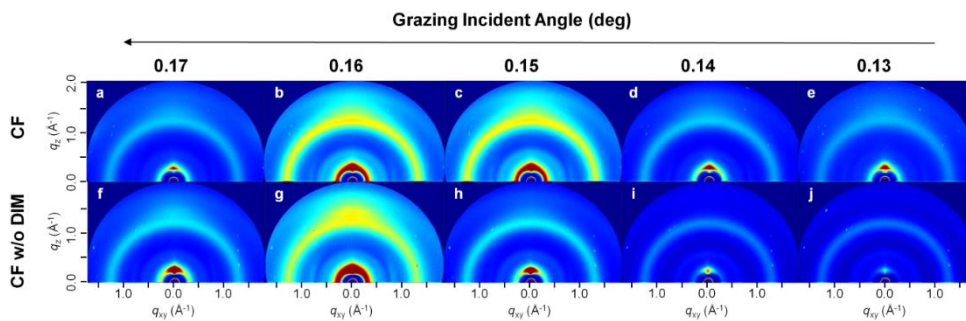


Figure 3.3.4. 2D Grazing-Incidence Wide-Angle X-ray Scattering (GIWAXS) patterns of PTB7-th \ PC70BM sequentially deposited layers depending on solvent and grazing incident angle.

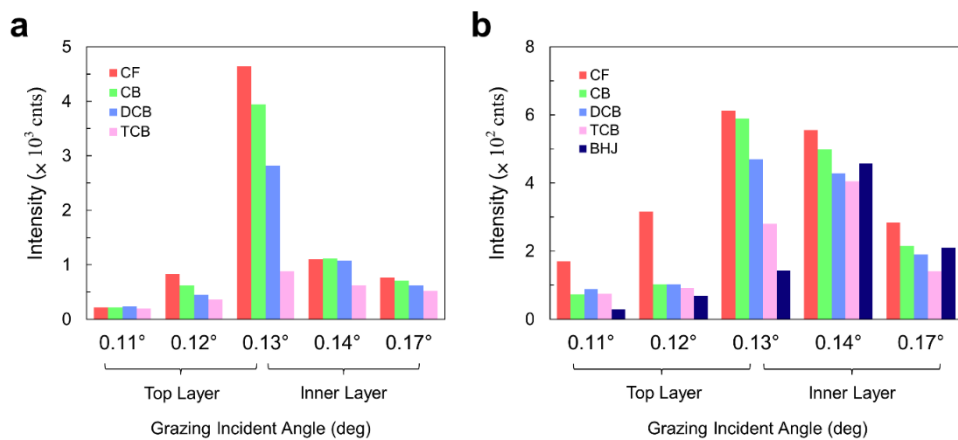


Figure 3.3.5. Scattering intensities measured at (010) position in qz direction with different grazing incidence angles and deposition solvents of (a) PTB7-th and (b) PTB7-th \ PC70BM sequentially deposited layers.

As depicted in Figure 3.3.6. and Table 3.3.1., the J-V characteristics varied significantly depending on the photoactive layer conditions. Briefly, devices with BHJ and CF based sequentially processed device showed similar performance of $J_{SC} = 14.304 \text{ mA cm}^{-2}$, $V_{OC} = 0.809 \text{ V}$, $FF = 0.621$, $PCE = 7.204\%$ and $J_{SC} = 15.422 \text{ mA cm}^{-2}$, $V_{OC} = 0.792 \text{ V}$, $FF = 0.586$, $PCE = 7.156\%$, respectively. On the other hand, devices based on the other solvents showed lower characteristics where the PCE of CB, DCB, TCB based sequentially processed devices are 5.892%, 4.191% and 3.519%, respectively. Along with the various J-V characteristics, incident photon-to-electron conversion efficiency (IPCE) of devices with respect to the solvents showed similar order of magnitude: BHJ, CF, CB, DCB and TCB (Figure 3.3.6.b).

In order to figure out the charge migration property inside the PTB7-th with respect to the top and inner layer crystallinity, hole-only devices (HODs) were fabricated and characterized (Figure 7a). In accordance with precedent studies, the J-V graph of HOD generally shows consecutive regions of ohmic conduction, SCLC, trap-filled limited (TFL) SCLC and trap-free SCLC regions.¹²³ In brief, at low voltage region, the current increases linearly to the applied voltage indicating ohmic conduction. Afterward, the current starts to show square dependence to voltage which is attributed to the space charge formation inside the organic layer. However, after trap-filled limited voltage (VTFL), it starts to increase rapidly over square dependence because of trap filling procedures. After the current increase by the factor of θ , trap-free SCLC follows with square dependency indicating complete filling of traps. In Figure 3.3.7.a, graphs of CF and CB based HODs show almost identical results with serial steps of ohmic conduction and SCLC which have ignorable regions of TFL SCLC. However, it is noteworthy that DCB and TCB based HODs show distinct TFL SCLC regions. For DCB based HOD, the VTFL equals to

0.341 V and current density (J) increased by the order of 10^2 . Meanwhile, TCB based HOD showed VTFL of 2.326 V and current density (J) increment in the order of 10^4 , which showed much larger increment in terms of VTFL and θ . Because the magnitude of VTFL is known to be proportional to $N_t \cdot L^2$, where N_t is trap density and L is layer thickness,¹²⁴ it can be interpreted that DCB and TCB based PTB7-th contain more trap sites inside the layer compared to CF and CB. Considering the fact that less crystalline structure at surface layer is disadvantageous for efficient charge dissociation at the interface, it can be concluded that the results of HODs are in good agreement with the results of device performance (Figure 1) and GIWAXS (Figure 2 and Figure 3).

In addition, the open-circuit voltage (V_{OC}) as a function of light intensity (P_{light}) was measured to check the effect of trap-assisted recombination (Figure 5b). In accordance with the previously reported articles, the slope of natural logarithm of P_{light} against V_{OC} equals to the product of the ideality factor (n) and thermal voltage (kT/q), where k is Boltzmann's constant, T is absolute temperature in Kelvin and q is the elementary charge. In brief, bimolecular recombination is the dominant factor in open-circuit condition because of the lack of electric field. However, when additional monomolecular recombination such as trap-assisted recombination starts to involve, the ideality factor (n) starts to increase up to 2 to the maximum. Based on the methods, the ideality factors (n) of CF, CB, DCB and TCB were extracted to be 0.976, 1.246, 1.165, 1.265 and 1.495, respectively. Along with the J-V characteristics of HODs (Figure 5a), solvents with higher boiling points of DCB and TCB based devices showed higher ideality factor compared to CB based OSC. Thus, on the basis of the HOD results and P_{light} -dependent V_{OC} , it can be concluded that the variant performance in OSCs (Figure 3.3.6.) is attributed to the different top layer

crystallinity (Figure 3.3.2. and Figure 3.3.3.) which is in good agreement with the trend found in the VTFL (Figure 3.3.7.a) and ideality factor (n) (Figure 3.3.7.b).

To get a further insight into the device properties in terms of stability, devices were thermally aged at 85°C under Ar atmosphere for 1,000 h (Figure 3.3.8.). In order to provide a precise index of degradation, widely used life-time indicator T_{80} is adopted which shows the duration time until the performance drops by 20% from its initial value. In terms of J_{SC} , BHJ device showed a rapid degradation ($T_{80} = 5.5$ h) while sequentially processed devices dissolved in CF, CB, DCB and TCB maintained 90%, 87%, 93% and 100% of their initial values after 1,000 h (Figure 3.3.8.a). Similar to the trend observed in J_{SC} , V_{OC} showed apparent difference between BHJ and sequentially processed OSCs. Whereas the V_{OC} of BHJ deteriorated rapidly ($T_{80} = 9.8$ h), the sequentially processed devices retained their initial values even after 1,000 h (Figure 3.3.8.b). The disparity between BHJ and sequentially processed devices is in a good agreement with the former reports claiming the disadvantageous structure of BHJ against thermal stress compared to the sequentially processed photoactive layers which are robust against the thermal stress. However, their FF degradation tendency severely differed according to their photoactive geometry, which was fabricated by typical mixture deposition (BHJ) or sequentially deposition, as well as solvents used in sequential deposition. T_{80} of BHJ and CF, CB, DCB based sequentially processed devices corresponded to 28 min, 419 h, 84 h, 834 h while TCB based device retained its 89% at the end of the aging procedure (Figure 3.3.8.c). Taking into account that the overall PCE is a combined index of J_{SC} , V_{OC} and FF, the degradation tendency of PCE followed that of FF (Figure 3.3.8.c,d). Although the fundamental connection between vertically-segmented crystallinity and FF degradation trend needs to be further studied, it is

noteworthy that the solvents used in sequential deposition not only affected the top and inner layer crystallinity, the main reason for the PCE divergence (Figure 3.3.6.), but also the long-term thermal stability (Figure 3.3.8.) providing a critical clue in designing efficient and stable OSCs.

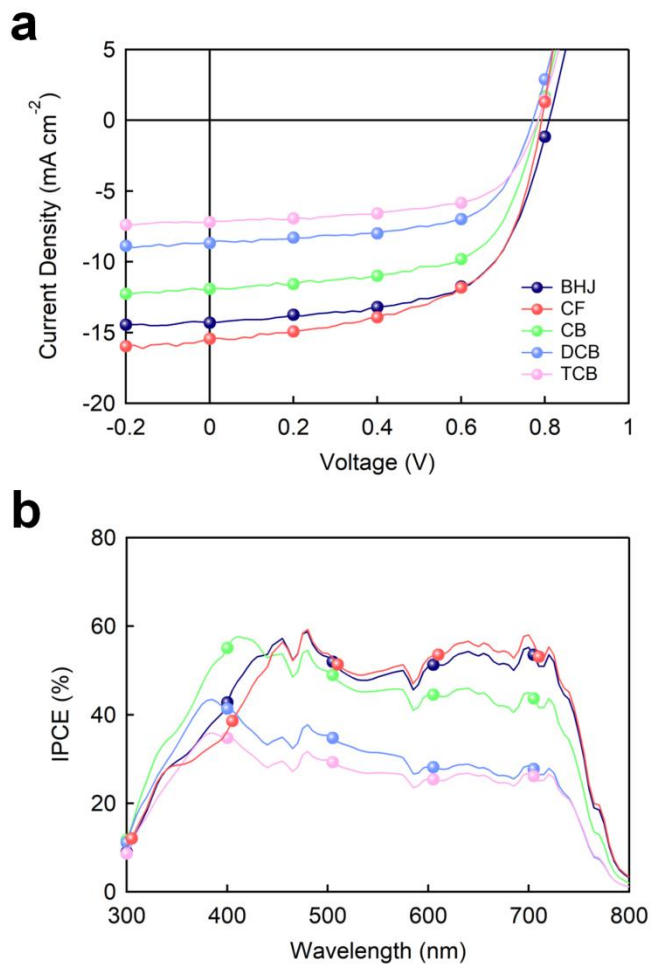


Figure 3.3.6. (a) Current-voltage (J-V) characteristics, (b) incident photon-to-electron conversion efficiency (IPCE) of OSCs with PTB7-th dissolved in various solvents with identical thickness of photoactive layer.

Table 3.3.1. Current-voltage (J-V) characteristics of OSCs with various photoactive layer conditions.

	BHJ	Sequential Deposition			
		CF	CB	DCB	TCB
J_{sc} (mA cm ⁻²)	14.304	15.422	11.899	8.674	7.189
V_{oc} (V)	0.809	0.792	0.784	0.770	0.783
FF	0.621	0.586	0.631	0.626	0.625
PCE (%)	7.204	7.156	5.892	4.191	3.519

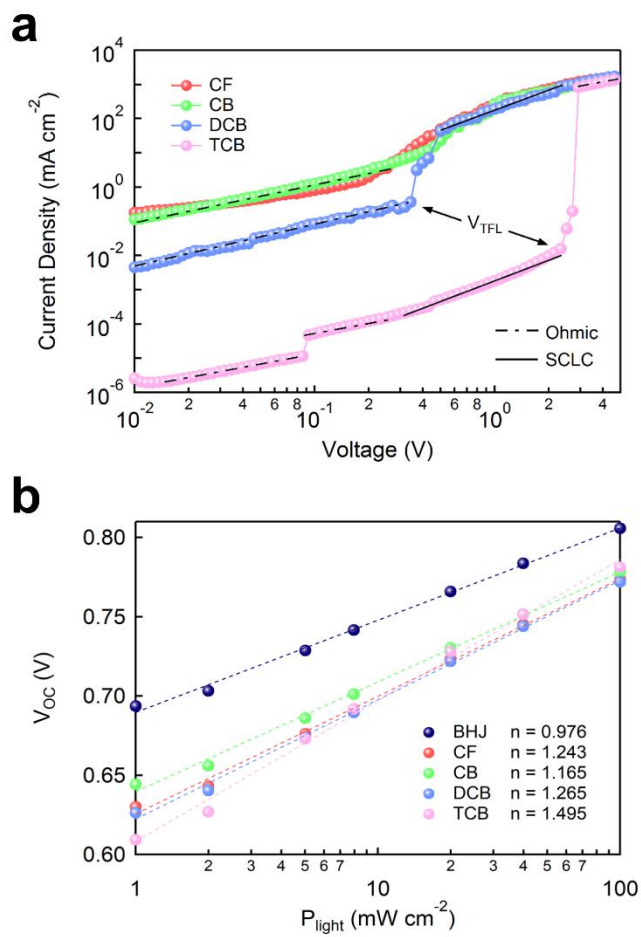


Figure 3.3.7. (a) Current-voltage (J-V) characteristics of HODs and (b) V_{OC} as a function of P_{light} varying the solvent of PTB7-th.

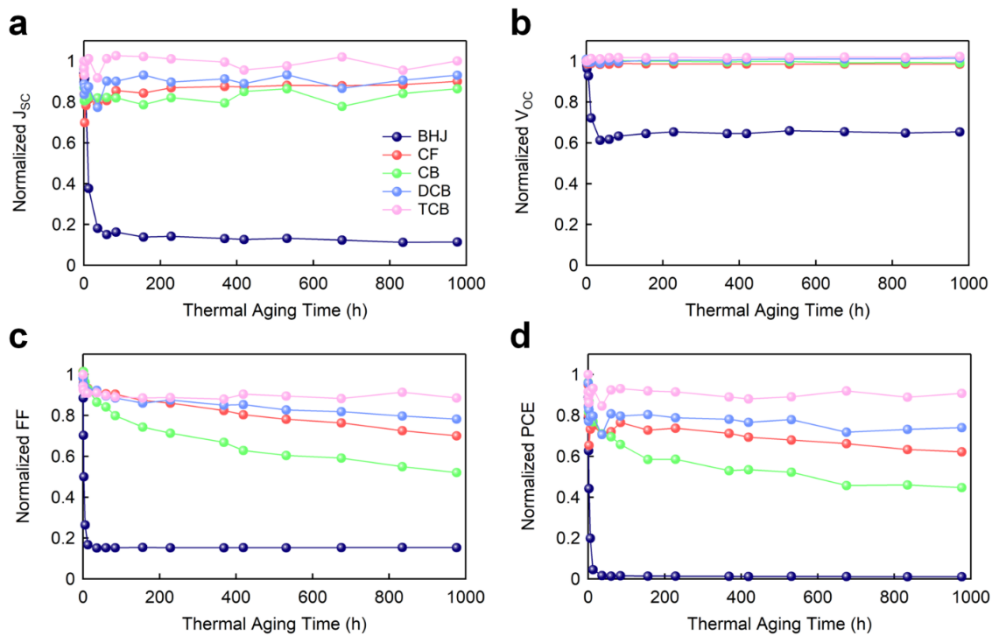


Figure 3.3.8. Degradation tendency of (a) J_{sc} , (b) V_{oc} , (c) FF, (d) PCE as a function of 85°C thermal aging at 85°C for 1000 h.

3.4. Conclusion

Two examples of nanoconfined geometry were shown and applied in organic solar cell to realize efficient and stable performance. First we observed the formation of network structures of P3HT nanowires by thermal treatment and analyzed the effects of nanowire network structures on the electrical properties, power conversion efficiencies, and thermal stability of the resulting photovoltaic devices. The detailed structural features were characterized by SANS measurements, and the results revealed the formation of nanoconfined geometry in PCBM domains, leading to suppressed aggregation. In addition, shorter nanowires fabricated by using 2CP additive showed smaller network structures which led to higher degree of confinement. Blend films having nanowire network structures showed highly increased electron and hole mobilities, along with smaller domain sizes that resulted in significantly enhanced device performance compared to typical non-network BHJ structures of the same thickness. Devices based on the smaller network structures showed the highest device performance, with 43 % enhancement in PCE compared to non-network devices. Moreover, nanowire network devices showed significantly enhanced device stability compared to BHJ and non-network structures. We believe that employing polymeric nanowire and their nanowire network structures is a promising strategy to realize stable and efficient organic solar cells.

Second, we conducted an exhaustive and systematic investigation on the correlation between vertically-segmented crystallinity and performance of OSCs including J-V characteristics and thermal stability. In order to vary the top and inner layer crystallinity, several solvents, such as CF, CB, DCB and TCB, were adopted which sensitively affected the performance of OSCs. In brief, while other factors (V_{OC} , FF) maintained similarly regardless of the top and inner layer crystallinity, J_{SC}

differed a lot which consequently resulted in variant PCE: CF (7.156%), CB (5.892%), DCB (4.191%) and TCB (3.519%). The different J_{SC} is mainly ascribed to the crystallinity at the top layer. On the basis of the GIWAXS measurement results (Figure 2 and 3), it is revealed that though the crystallinity at the bulk state is almost same, or slight higher for solvent with lower boiling points, the top layer showed higher crystallinity for lower boiling points. The different degree of top layer crystallinity resulted in different charge dissociation property which is also supported by the J-V characteristics of HODs (Figure 4). Contrary to the PCE results, the stability against external heat of 85°C is found to be irrelevant to the top and inner layer crystallinity. Rather it is concluded that OSC with less top and inner layer crystallinity showed better endurance. The different thermal stability is ascribed to the different durability of FF depending on the vertically- segmented crystallinity. Although the fundamental explanation on the less stable FF of higher PCE devices should be further studied, our result provides a differentiated analysis regarding the vertically-segmented crystallinity and performance of OSCs. We believe that our strategies, using nanoconfinement provide a valuable insight into designing highly efficient and stable OSCs.

Chapter 4. Controlling Structural Properties and Dynamics of Conjugated Polymers by Nanoconfined Geometry for Efficient and Stable Organic Solar Cells

4.1. Introduction

In chapter 2, effect of nanoconfinement on structure properties of conjugated polymer were studied. By employing nanostructured sample, we could obtain highly increased charge mobilities along vertical direction for both semicrystalline polymer and amorphous polymer due to increased crystallinity corresponding to face-on orientation. In chapter 3, effect of nanoconfinement on dynamics of organic materials were studied. By employing robust n-type polymer nanostructures, we could impose confined geometry to PCBM surroundings suppressing aggregation of PCBM. Previous two examples showed significance of nanoconfinement for efficient and stable performance. However, those systems are difficult to analyze dynamics of materials quantitatively. Therefore, we used ordered heterojunction (OHJ) well-defined systems as a platform to understand structural properties and dynamics and to utilize both improved structural and dynamical properties by nanoconfinements.

Effect of nanoconfinement on both structural properties and dynamics was applied to organic solar cell to realize efficient and stable organic solar cells in this chapter. P-type materials PCBM and PNDIT were deposited on top of 70 nm size in diameter P3HT nanopillars to fabricate ordered heterojunction geometry. Strong face-on orientation with high crystallinity in P3HT nanopillars will provide effective pathways for hole transport along vertical direction. Their interdiffusion between

donor and acceptor molecules were effectively controlled by changing annealing conditions. In addition, their dynamics were quantitatively analyzed by in-situ GISAXS experiments. They have shown different rate of diffusion and stabilized degree of diffusion. We could highly enhance device performance by decreasing domains sizes from the controlled interdiffusion between donor and acceptor molecules. Moreover, they endured harsh thermal conditions up to 200 °C for 4 hours by the stabilized interdiffusion due to nanoconfinement.

4.2. Experimental

Fabrication of P3HT Nanopillar and Nanohole. P3HT nanopillar and nanoholes were prepared using the same method in Chapter 2.

Device Fabrication and Characterization. Solar cell devices were fabricated on patterned indium tin oxide (ITO)-coated glass substrates, which were cleaned using a sequence of sonication in acetone, isopropyl alcohol, and deionized water for 15 min, and subsequently dried overnight in an oven. The substrates were then subjected to 10-min ultraviolet-ozone (UVO) treatment. Poly(3,4-ethylene dioxythiophene):poly(styrene sulfonate) (PEDOT:PSS, Clevios HTL solar) was then spin-coated at 4000 rpm for 40 sec to realize a film thickness of ~ 70 nm. The resulting samples were dried for 30 min at $120\text{ }^{\circ}\text{C}$ and subsequently taken to an inert atmosphere. In a glove box, P3HT nanopillars (or nanoholes) were transferred to the PEDOT:PSS-coated ITO substrates. PC₆₀BM (or PNDIT) dissolved in dichloromethane was then spin-coated on the top of P3HT nanopillars (nanoholes). 0.5-nm LiF and 100-nm Al layers were then thermally evaporated under 10^{-6} Torr vacuum. After the completion of device fabrication, the devices were thermally annealed from $80\text{ }^{\circ}\text{C}$ to $200\text{ }^{\circ}\text{C}$ for 60 min. The active area of the solar cells given by the overlap between ITO and Al electrodes was 9 mm^2 .

The current density-voltage (J-V) characteristics of the solar cell devices were measured with a source measurement unit (Keithley SMU237). The device performance was characterized under AM1.5G solar spectrum at 1 Sun (100 mW/cm^2) illumination simulated by a Newport 91160A device.

Quantitative Imaging (QI)-cSFM. Nanostructured P3HT/PCBM films were prepared on bare ITO substrates. QI-cSFM was performed using a JPK Nanowizard 3 in Advanced QI mode. Cantilevers coated with a 25 nm thick layer of chromium and platinum iridium on both sides (PPP-EFM from Nanosensors) were used to measure the conductivity of all the samples. All the measurements were performed with a tip bias voltage of +6 V. A halogen lamp with an intensity of 45 mW/cm² was employed to excite and measure the photoconductivity of the samples.

Grazing-Incidence Small and Wide-Angle X-ray Scattering (GISAXS and GIWAXS) Measurements. GISAXS was performed at the 3C Beamline of the Pohang Accelerator Laboratory (PAL). The sample-detector distance (SDD) was 3.950 m. X-ray with a wavelength of $\lambda = 1.135 \text{ \AA}$ and an incident angle of 0.14° were used for the measurements. GIWAXS was performed at the 9A Beamline of the Pohang Accelerator Laboratory (PAL). X-ray with a wavelength of $\lambda = 1.114 \text{ \AA}$ and an incident angle of 0.14° were used for the measurements. Nanostructured samples were thermally annealed in a vacuum sample chamber and they reached the final temperatures (80 - 200 °C) within 1-2 min and GISAXS and GIWAXS measurements on the samples were performed at a fixed temperature for 120 min.

4.3. Results and Discussion

4.3.1. Ordered Heterojunctions by Polymer : Fullerene systems

We suggest a new fabrication method, based on the combination of NIL with subsequent self-organization of molecules to fabricate active layers of OPVs. Herein, we combine the unique advantage of NIL allowing to generate controlled morphology with the self-organization of molecules into nm-scale domains by providing an external stimulus, which is the thermal annealing in this work. Upon thermal anneal, phenyl-C61-butyric acid methyl ester (PCBM) readily diffuses into conjugated polymer films, typically within a few seconds, leading to the bulk heterojunction architecture. Here, we demonstrate that the mutual diffusion of P3HT into PCBM, which has never been considered before because of its relatively lower rate. It is also an important factor to be considered as well as the PCBM diffusion. These systematic mutual diffusion studies allow us to precisely control the nanostructure as well as to understand their nanostructure formation mechanism which has been difficult to elucidate using previous approaches. The controlled morphology of nanostructured P3HT:PCBM with the face-on orientation combined with the mutual diffusion of donor and acceptor molecules by thermal annealing at 150 °C exhibited a 92 % increase in device performance compared to the as-cast P3HT:PCBM solar cell.

The procedure to fabricate P3HT nanopillar arrays, based on the soft molding pattern transfer, is illustrated in Figure 4.3.1.a). Different sizes of P3HT nanopillars can be easily prepared by the soft molding pattern transfer method which has previously been reported. Polyfluoropolyether (PFPE) replica molds with hexagonal nanopores were prepared using a two-step replication process from an AAO template. The P3HT nanopillar arrays were transferred to a target substrate after filling up the

nanopores of PFPE replica molds with P3HT solutions by spin-casting. We note that the transfer process is possible at low temperature (50 - 60 °C) and low pressure (~ 4 bar) because of low surface energy properties of PFPE molds. We fabricated P3HT nanopillars with 75 nm in diameter and 100 nm in height, confirming the nanopillars of uniform size as shown in the scanning electron microscopy image (Figure 4.3.1.b)). The volume ratio of empty space to P3HT nanopillars is estimated to be 1:1 (Figure 4.3.1.c)). Next, we deposited PCBM on the P3HT nanopillar array by spin coating using dichloromethane as an orthogonal solvent. Scanning force microscopy (SFM) analysis of the PCBM-coated samples at this process step revealed that PCBM completely covered the P3HT nanopillars (Figure 4.3.2b). The dimples in the topography were found at the top of the nanopillars and were attributed to voids formed during spin-casting (left side of Figure 4.3.2a). Furthermore, defect areas such as delaminated P3HT pillars were not observed, indicating that the nanopillar structure was intact during sample preparation. In addition, we confirmed that our P3HT:PCBM nanostructured films were fabricated in large area with good ordering, as evidenced from grazing-incidence small angle X-ray scattering (GISAXS) measurements (Figure 4.3.3.).

Although the NIL is the method capable of realizing micro- to nano-scale patterns, the fabricated nanopillars of 75 nm in diameter and 100 nm in height are not sufficient to meet the requirements for perfect ordered heterojunctions of active layers in organic solar cells. The latter exciton diffusion in active heterojunctions requires the distance between donors and acceptors in the range of 10 nm. Therefore, additional thermal annealing was employed to enable the molecular diffusion on otherwise interdigitated donor-acceptor structures to meet such requirement. To explore the effect of temperature on diffusivity, SFM experiments have been

performed on the patterned P3HT:PCBM thin films which were annealed for 20 min at a series of temperature from 80 °C to 180 °C. In addition, we soaked the samples in cyclohexane to selectively remove the upper layer of PCBM deposited on the P3HT nanopillars so that the pillar structures underneath, depending on anneal conditions, can be studied in more detail. Cyclohexane (CH) has typically been used to remove top PCBM layer without affecting the P3HT layer underneath. Figure 4.3.2.b) shows the scanning force microscopy (SFM) height images just after annealing the samples and Figure 4.3.2.c) shows the height images after soaked with cyclohexane. For the samples as-prepared and annealed at 80 °C, we noticed that there is a conversion from dimples of about 3 nm deep, located at the top of P3HT nanopillars, to small protrusions upon cyclohexane treatment observed between non-treated and CH-treated samples. We further observed that for the samples annealed at 120 and 150 °C, the small dimples observed on top of P3HT pillars become small protrusions of about 3 nm in height even without cyclohexane treatment. We attribute the conversion of the dimples to the small protrusions located on top of P3HT pillars to the decrease in the thickness of PCBM overlayer due to the migration of PCBM molecules to fill up the voids between P3HT nanopillars, as sketched in Figure 4.3.2.a). Upon annealing the samples to 150 °C the interfaces between pillars and their surroundings become fuzzy or blurry, implying that the P3HT chains mutually diffuse into the PCBM surroundings. Further increase in the anneal temperature up to 180 °C leads to the disappearance of pillar structure. We attribute the disappearance of the pillar nanostructure as the consequences of massive mutual diffusion between PCBM and P3HT molecules.

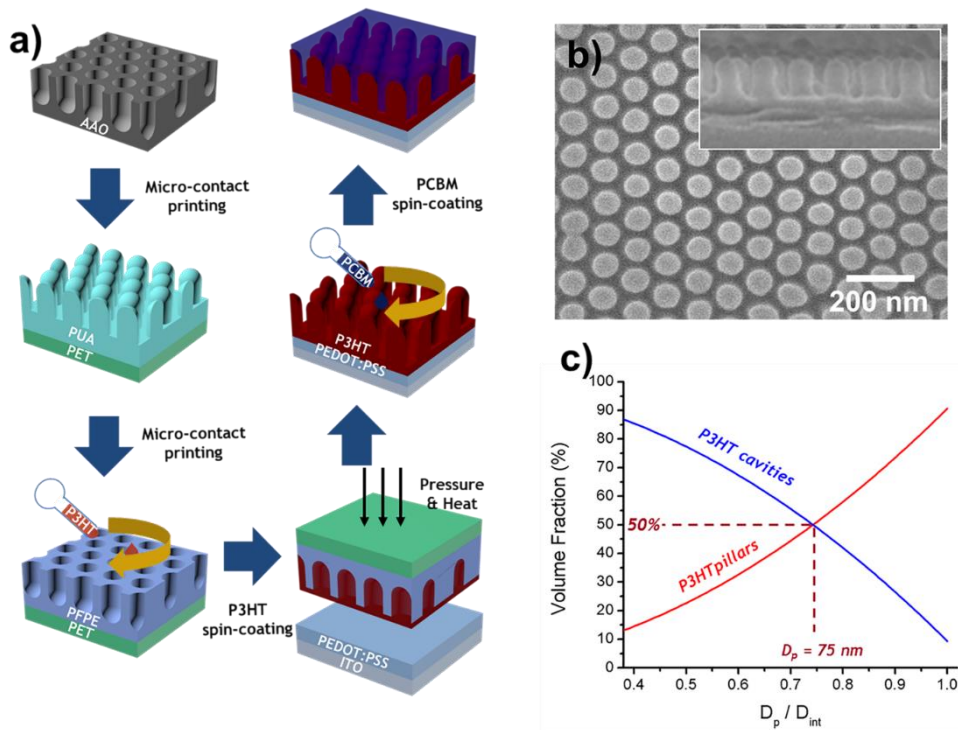


Figure 4.3.1. a) A schematic illustration for the procedure to fabricate P3HT nanopillars and subsequent PCBM deposition. b) Plan-view and cross-section scanning electron microscopy (SEM) images of P3HT nanopillars prepared. c) A diagram showing the change in volume fraction of P3HT pillars and cavities as a function of pillar diameter (where D_p is the pillar diameter and D_{int} is the pillar to pillar distance)..

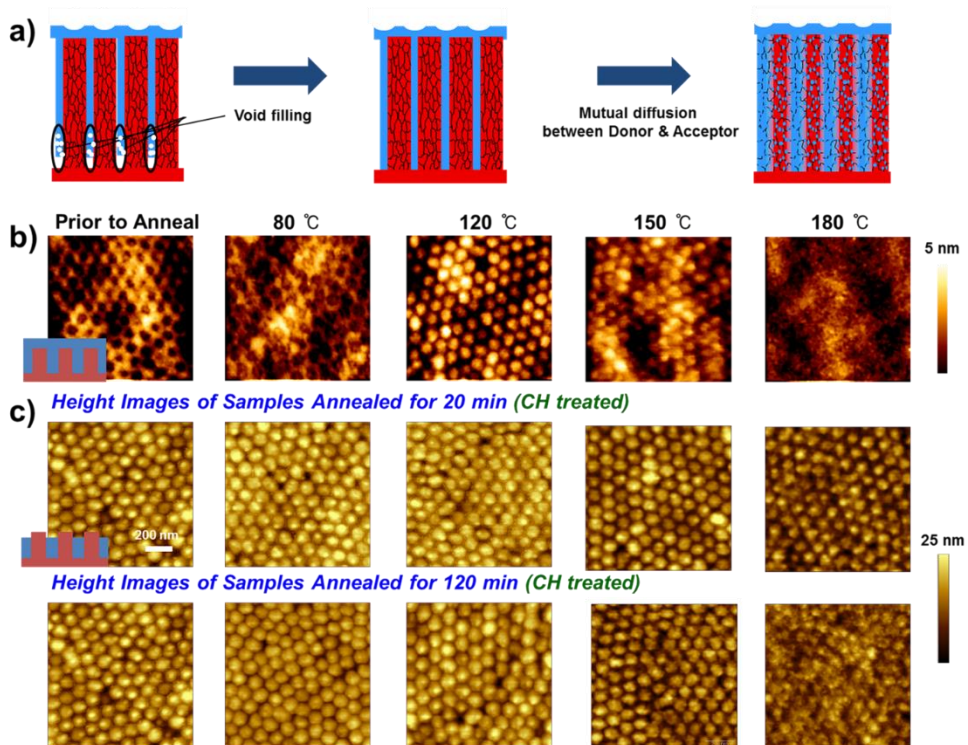


Figure 4.3.2. a) A schematic illustrating of the two types of diffusion processes. SFM height images of b) P3HT:PCBM nanostructured samples as-prepared and annealed at four different temperatures (80, 120, 150, and 180 °C) for 20 min and c) P3HT nanopillar structures with PCBM top layers that were removed by cyclohexane.

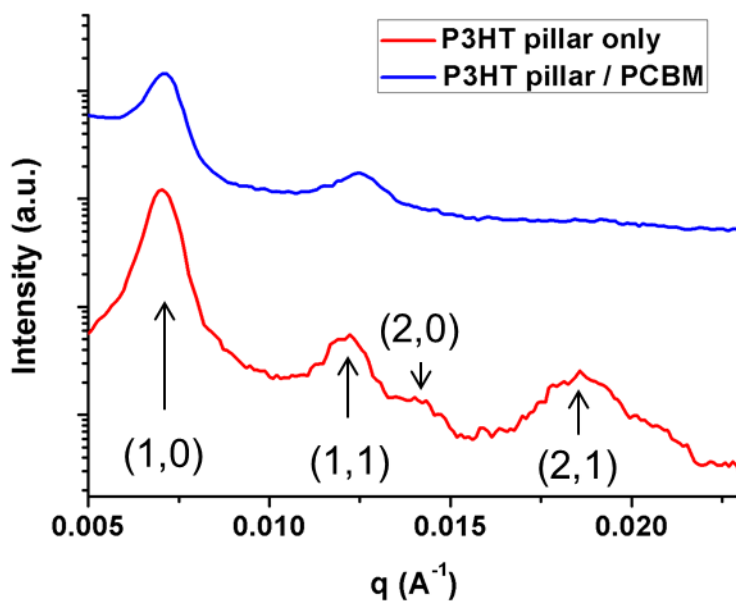


Figure 4.3.3. Horizontal cuts of GISAXS measurements of a P3HT pillar only film (red) and a sample with P3HT pillars deposited with PCBM (blue) with corresponding Miller indices. The P3HT pillar only film shows the hexagonal scattering with the fourth-order peak feature representing a good ordering of the P3HT nanopillars. The P3HT pillars surrounded by PCBM shows the first and second order peaks due to low electron density contrast between P3HT and PCBM.

GIWAXS provides information on the molecular arrangement of the crystalline phases of P3HT in terms of orientation and average size of the crystalline phases. The 2D GIWAXS patterns of imprinted P3HT nanopillars showed strong $\pi - \pi$ peaks along the out-of-plane direction, representing the face-on orientation (Figure 4.3.4.a)). However, PCBM deposition followed by thermal annealing resulted in a slight decrease in the face-on orientation (Figure 4.3.4 and Figure 4.3.6.). In order to investigate the azimuthal alignment of the P3HT chains, the angular scattering profiles were obtained at the (010) peak position (Figure 4.3.6.). These profiles provide information on the angular distribution of $\pi - \pi$ stacks of P3HT. Our measurements revealed that the face-on population decreased with increasing annealing temperature (Figure 4.3.4.g)).

The temporal changes of the P3HT (100) peaks allow determining the size of lamellae crystals during annealing at different temperatures (Figure 4.3.4.). Using Scherrer's equation, the temporal changes in P3HT crystal size were obtained from the corresponding (100) peak widths, which was extracted from the GIWAXS patterns (Figure 4.3.5.). The growth behaviors are shown in Figures 4.3.4.h) and 4.3.4.i), showing that they reach plateau values within 5 min, which is in good agreement with the previous results. As the annealing temperature was increased, the crystal size also increased. However, when the sample was annealed at 180 °C, the crystal size along the out-of-plane direction became smaller than the size annealed at 150 °C, presumably due to the nano-confinement effects.

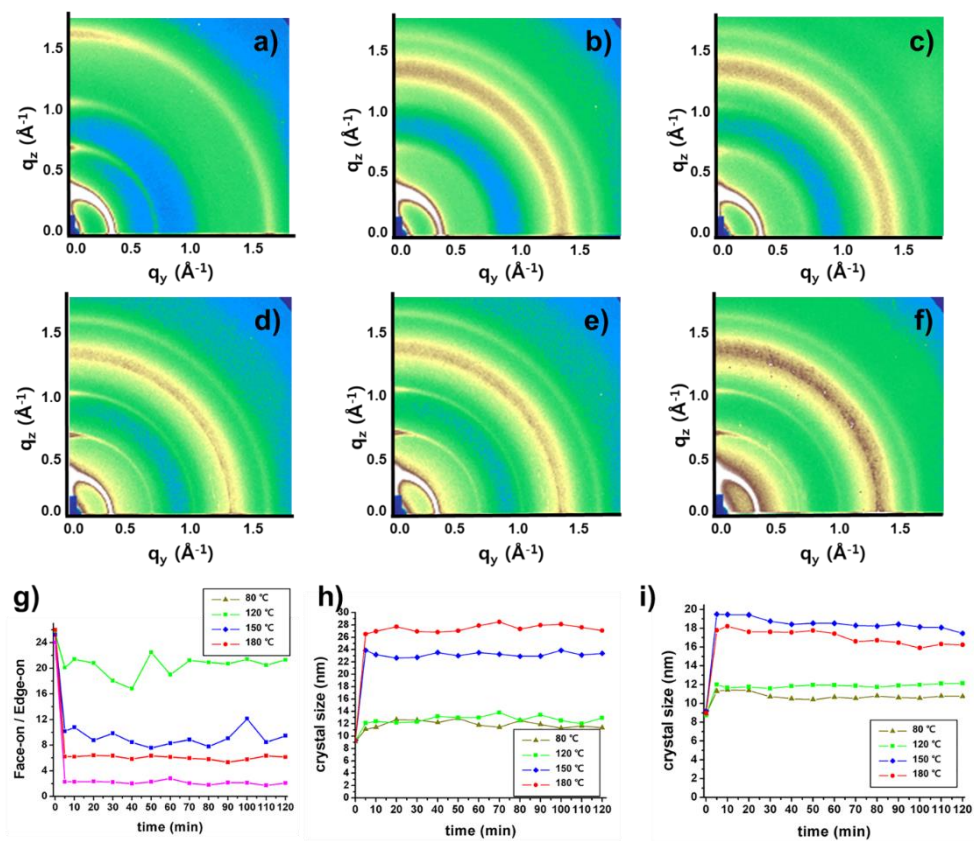


Figure 4.3.4. GIWAXS 2D scattering patterns of a) P3HT nanopillars, b) as-prepared nanostructured P3HT/PCBM films (PCBM deposited on P3HT nanopillars), and c) nanostructured P3HT/PCBM films annealed at 80 °C, d) 120 °C, e) 150 °C, and f) 180 °C. g) The ratio of face-on orientation population to edge-on orientation of nanostructured P3HT/PCBM films with 4 different anneal temperatures. The changes in crystal size as a function of annealing time: h) in the in-plane direction and i) in the out-of-plane direction at 4 different annealing temperatures.

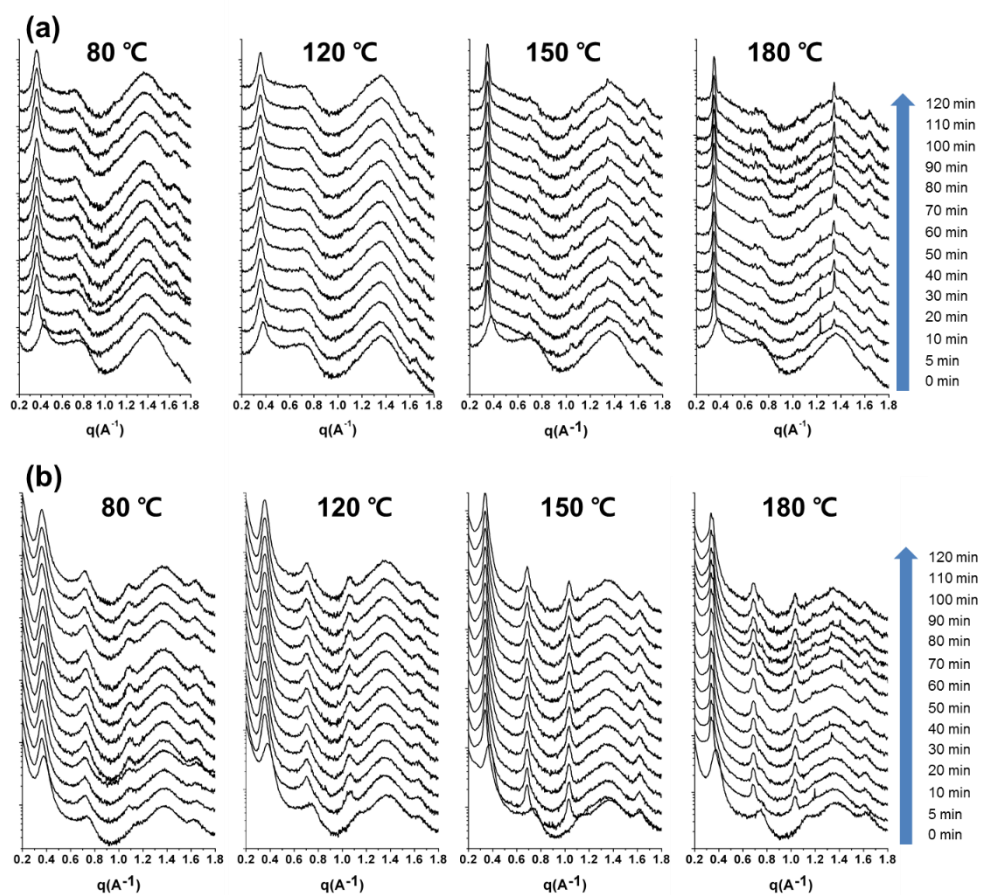


Figure 4.3.5. GIWAXS line cuts along: (a) q_y and (b) q_z directions from nanostructured P3HT/PCBM films, which were measured during thermal anneal at 4 different anneal temperatures (80, 120, 150, and 180 °C) up to 120 min.

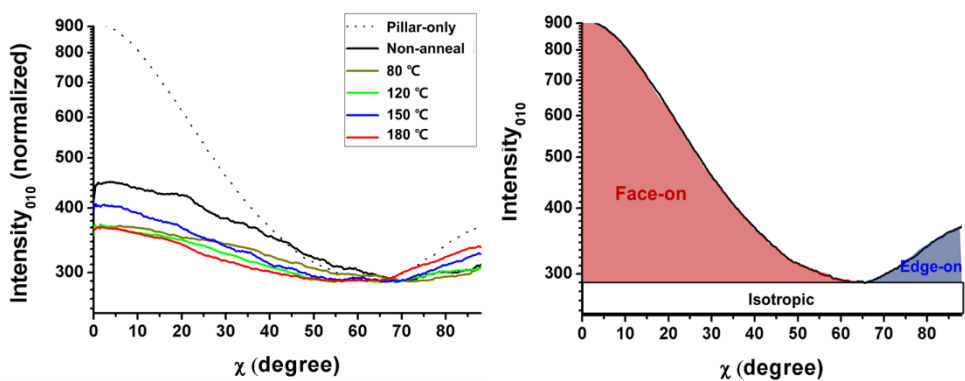


Figure 4.3.6. (a) Angular cuts at the (010) position of P3HT pillar-only, as-cast P3HT pillar/PCBM, and the P3HT pillar/PCBM samples annealed at 4 different temperatures. (b) A schematic on the contributions to face-on (red), edge-on (blue), and isotropically (white) oriented P3HT in the integrated intensity of the angular cut.

GISAXS measurements have been performed to quantitatively monitor the in-situ molecular diffusion and its effect on pillar nanostructures. GISAXS allows us to gain information on statically averaged structures ranging from a few nanometers to several hundred nanometers, which correspond to the domain size of active layers in organic solar cells. Many investigations have previously been performed to probe the domain structures as well as their temporal changes using in-situ GISAXS.¹²⁵⁻¹²⁷ However, since the domains in BHJs are much less ordered and polydisperse in size as well as randomly distributed in 3-dimension, their scattering peaks are typically very weak and broadly smeared, which makes the results hard to analyze and interpret.¹²⁵ Since our hexagonally-packed ordered heterojunctions with P3HT nanopillars and PCBM, produced by the new patterning approach, are well-defined in large area, we could extract more information on molecular diffusion and nanostructures from pronounced higher order peaks of the hexagonal patterns. By analyzing the scattering invariants (i.e., total scattering intensities) of scattering results, two kinds of dynamic processes were also identified as already speculated in the analyses of the SFM images.

P3HT:PCBM nanostructured samples showing the first and second order scattering features correspond well with the hexagonal packing whose distance between pillars is 100 nm as shown in Figure 4.3.3. Figures 4.3.7.a) ~ 4.3.7.d) show the changes in the GISAXS scattering profiles of the nanostructured P3HT/PCBM during the thermal anneal processes which induces molecular diffusion. These data clearly show the temperature- and time-dependent decrease in the scattering peaks. The amount or degree of mutual diffusion between donor and acceptor molecules can be qualitatively analyzed by calculating the total scattering intensity (TSI) of the peaks at different annealing temperatures and times. When the samples were

annealed at 80 °C and 120 °C for 20 min, the TSI reached 96 % and 94 % of the initial TSI value, respectively, due to the void filling process shown in Figure 4.3.2a. Annealing at 120 °C showed a faster void filling. It reached its equilibrium TSI value of 93 % within 30 min while 50 min was taken in the case of annealing the sample at 80 °C. In contrast, for the sample annealed at 150 °C, the mutual diffusion between P3HT and PCBM as well as the void filling was observed. After the void filling was complete in 4 - 5 min, TSI was further decreased due to the mutual diffusion between P3HT and PCBM. It reached the equilibrium value of 72 % TSI, corresponding to 13 % of P3HT diffused into surroundings. Even a faster decrease in TSI was observed when the sample was annealed at 180 °C, again due to the massive mutual diffusion, reaching their equilibrium value of 51 % TSI in 30 min (corresponding to 29 % of P3HT diffused into surroundings). The temperature-dependent mutual diffusion revealed by GISAXS qualitatively agrees well with the SFM results. The changes in TSI and the fractions of P3HT that diffused into the surroundings are plotted in Figures 4.3.7.e) and 4.3.7.f).

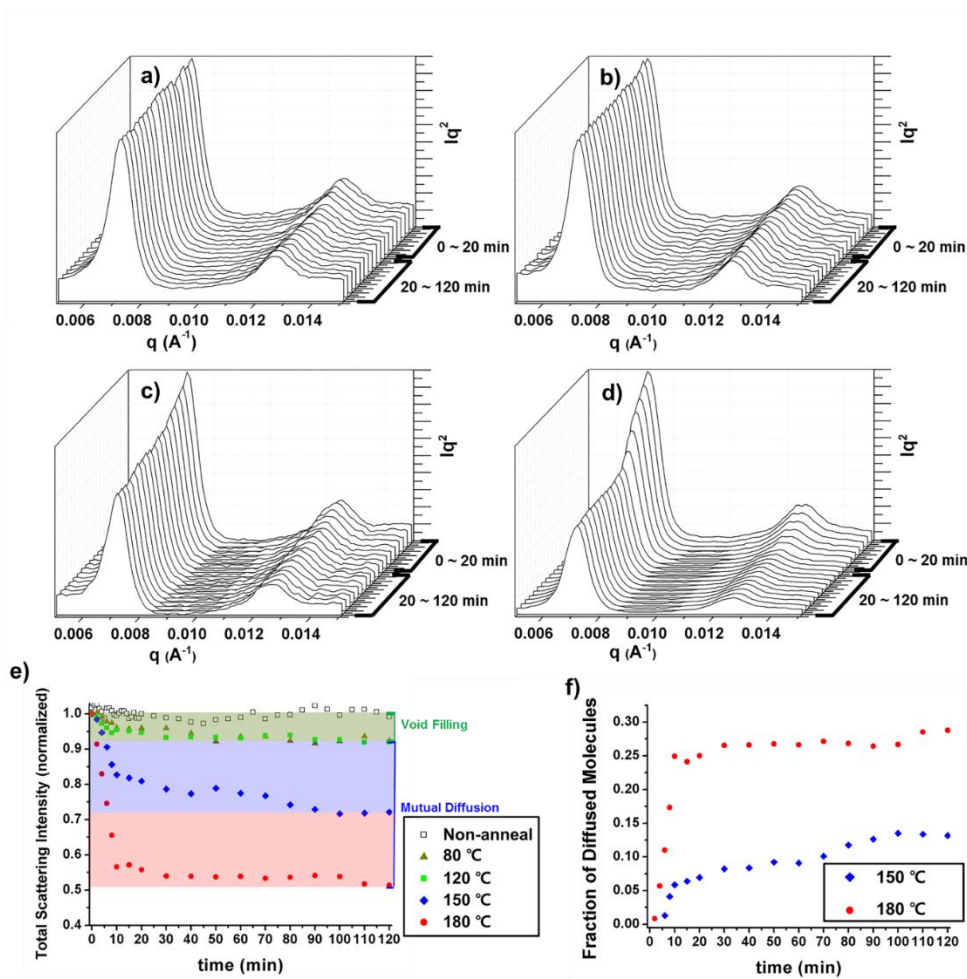


Figure 4.3.7. The changes in GISAXS scattering profiles of nanostructured P3HT/PCBM as a function of annealing time (up to 120 min) at: a) 80 °C, b) 120 °C, c) 150 °C, and d) 180 °C. e) The changes in total scattering intensity (TSI) as a function of annealing time at 4 different anneal temperatures. f) The changes in the fraction of P3HT diffused into surroundings as a function of annealing time for the samples annealed at 150 and 180 °C.

To investigate the electrical properties of individual nanopillars, we performed conductive SFM (cSFM). Typically, cSFM requires contact mode operation. However, the contact mode operation on soft samples can lead to surface deformation, such that fragile polymer nanopillar structures can be easily bent or even destroyed. To reduce or minimize this deleterious effect, a new cSFM mode has recently been developed, which is based on the torsion mode and/or on the peak force. Here, we applied the quantitative imaging (QI) mode, which allowed us to correlate the current flow between a tip and a sample at a defined loading force. First, the as-cast nanostructured P3HT/PCBM sample was investigated by QI-cSFM. For this sample, the PCBM surrounding area exhibited higher conductance when compared with the P3HT pillars upon measurements in dark and under illumination. The higher conductance is a consequence of higher charge mobility of PCBM compared to the P3HT pillars (Figure 4.3.11.). Annealing the samples at 80 °C and 120 °C, the mean conductance as well as photo-conductivity increased. We attribute this increase in photo-conductivity to the decrease in void space, which leads to better contacts between electron donor and acceptor materials. Furthermore, at 80 °C we also observed that the P3HT crystal size increased even though the fraction of the face-on orientation was slightly decreased. When the sample was annealed at 150 °C, it showed the highest conductance and photo-conductivity. A further increase in the annealing temperature to 180 °C resulted in the precipitous decrease in both conductance and photo-conductivity down to the magnitudes of the as-cast sample. The latter result seems plausible because an annealing temperature above 150 °C leads to the destruction of percolated pathways in nanopillars and, at the same time, to the decrease in the fraction of face-on P3HT orientation. In order to obtain more statistically averaged information of the samples, we performed measurements on

larger areas of $4 \mu\text{m} \times 4 \mu\text{m}$. This scale corresponds to the measurements of conductivities on more than 1,500 nanopillars. We plotted all current values measured at each pixel of the image in the histograms (Figure 4.3.9.). Then, we extracted the average conductivity and photo-conductivity from the histograms and summarized them in Table 4.3.1. The different histograms reflect higher (photo)conductivity for a proper amount of face-on orientation of P3HT pillars combined with increased crystal size.

We have so far investigated the nano-morphologies, electrical properties, and their correlations in the pillar-based P3HT/PCBM thin films depending on finely-tuned molecular diffusion using various techniques such as SFM, GISAXS, GIWAXS, and QI-cSFM. To further explore the morphological and electrical effects of individual pillars on overall solar cell device performance, solar cell devices (3 mm x 3 mm) were fabricated and measured under the AM 1.5G 1 Sun solar illumination (Figure 4.3.10.). Solar cell parameters deduced from current density (J)-voltage (V) curves are summarized in Table 4.3.2. As consistent with our results on individual pillars from QI-cSFM, different anneal conditions resulted in different short circuit current density (J_{SC}). The device performance gradually improved when the samples were annealed up to 150 °C, at which the solar cell showed 2.44 % of power conversion efficiency (PCE). The increase in PCE from the as-cast device to the devices annealed up to 120 °C is mainly attributed to the increase in J_{SC} because the voids initially formed at the interfaces between donor pillars and acceptor molecules disappeared upon annealing at relatively low temperature. Further increase in the device PCE with annealing the device at 150 °C is believed to originate from the additional mutual diffusion, which further reduces the pillar domain size, presumably providing more interfacial area for exciton dissociation or

carrier collection. However, after annealing the solar cell device at 180 °C, the PCE dramatically decreased. At this anneal temperature, the massive mutual diffusion between P3HT and PCBM completely destroyed the imprinted percolating pathways of the P3HT pillars. In addition, we confirmed the lower fraction of face-on oriented P3HT molecules at this anneal temperature.

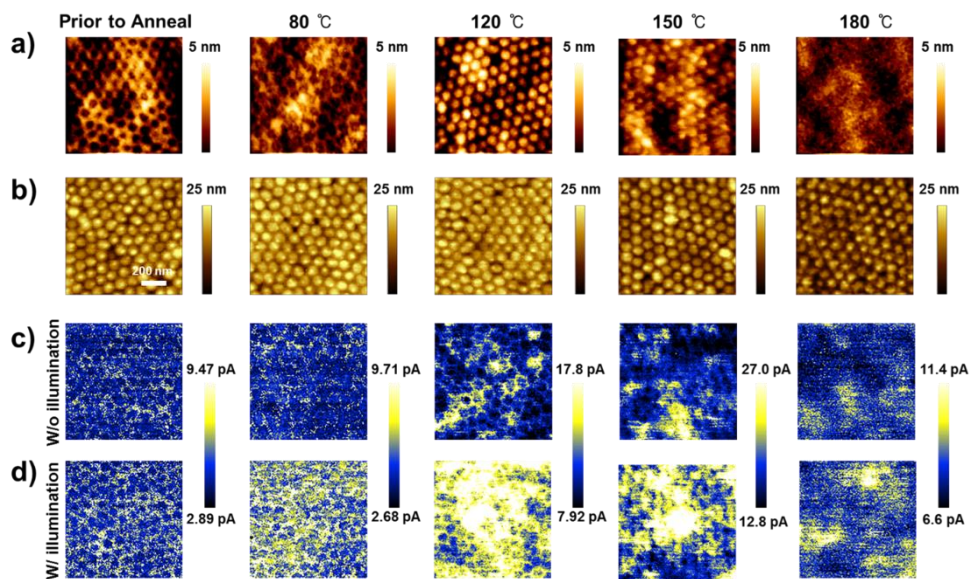


Figure 4.3.8. Height images of nanostructured P3HT/PCBM films a) with and b) without PCBM cap layer removed by cyclohexane treatment (i.e., only P3HT nanopillars remained) at 4 different annealing temperatures. cSFM images of nanostructured P3HT/PCBM films in the c) dark state and d) illuminated state annealed at 4 different temperatures.

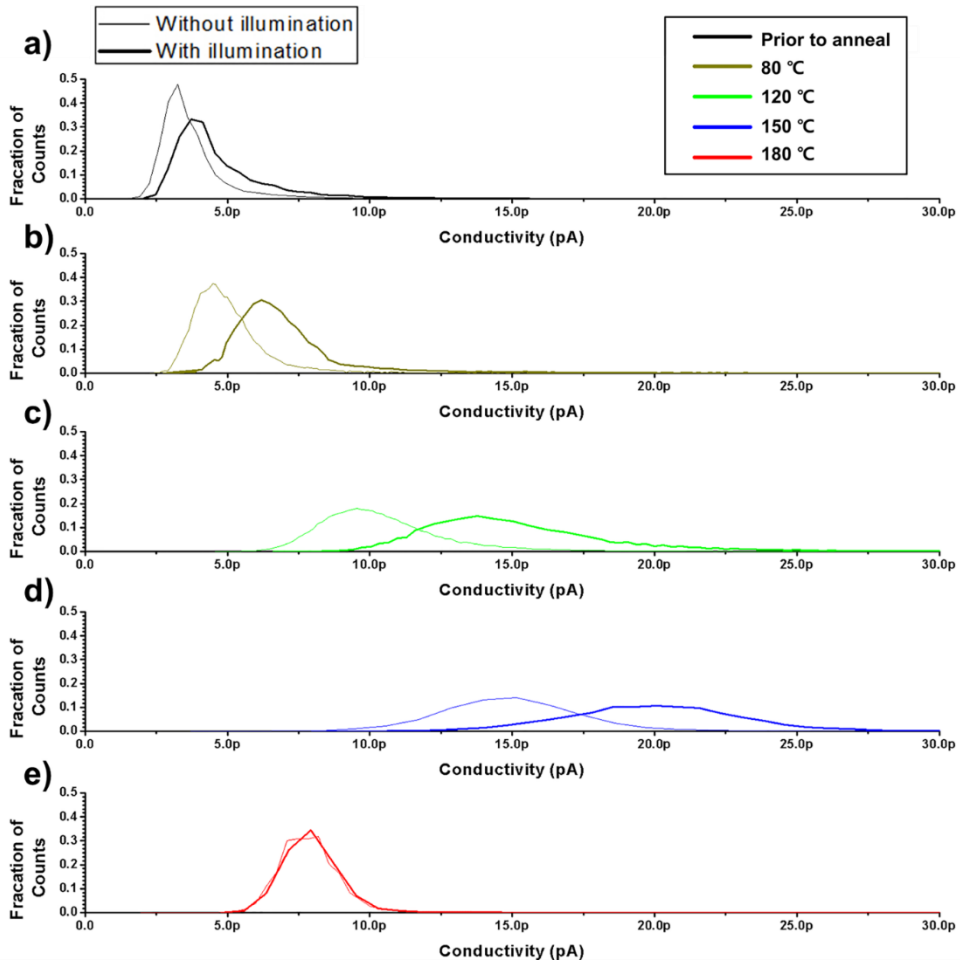


Figure 4.3.9. Histograms extracted from the cSFM results (with >1500 pillars) on the nanostructured P3HT/PCBM films with (a) as prepared and annealed at: (b) 80 °C, (c) 120 °C, (d) 150 °C, and (e) 180 °C.

Table 4.3.1. Summary of ensemble average conductivity and photoconductivity extracted from the histograms of Figure 4.3.9.

	As-Prepared	80 °C	120 °C	150 °C	180 °C
w/o illumination	3.92 pA	5.09 pA	10.5 pA	15.7 pA	8.06 pA
w/ illumination	5.02 pA	7.37 pA	15.5 pA	20.4 pA	8.39 pA
photoconductivity	1.10 pA	2.28 pA	4.95 pA	4.75 pA	0.333 pA

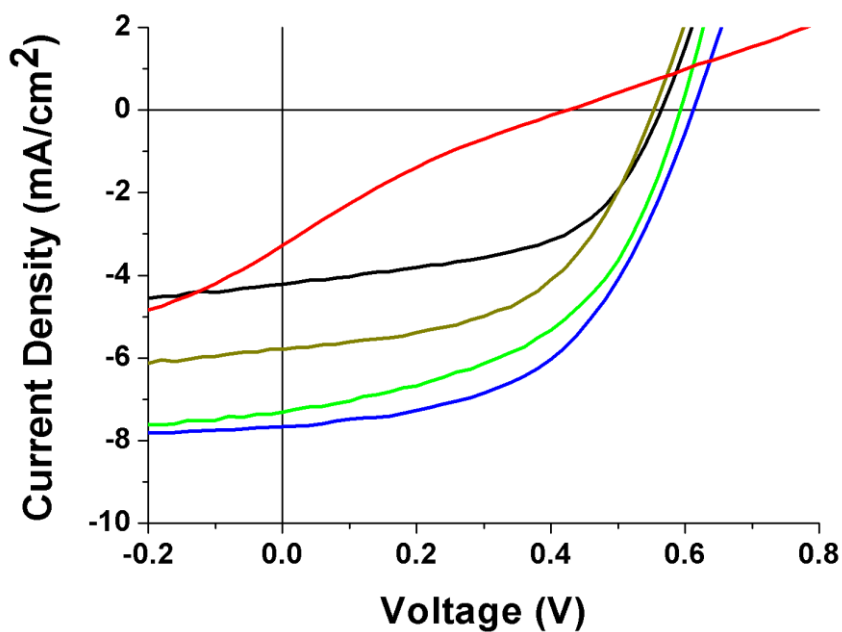


Figure 4.3.10. J-V characteristics of nanostructured P3HT/PCBM solar cells in different anneal conditions (as-prepared, annealed at 80 °C, 120 °C, 150 °C, and 180 °C), measured under 1 Sun illumination.

Table 4.3.2. Performance parameters of nanostructured P3HT/PCBM solar cells extracted from the J-V characteristics.

	As-Prepared	80 °C	120 °C	150 °C	180 °C
J_{sc} (mA/cm²)	4.22	5.79	7.32	7.68	3.27
V_{oc} (V)	0.56	0.55	0.59	0.61	0.43
FF (%)	53.40	52.07	49.17	51.84	19.86
PCE (%)	1.27	1.67	2.13	2.44	0.28

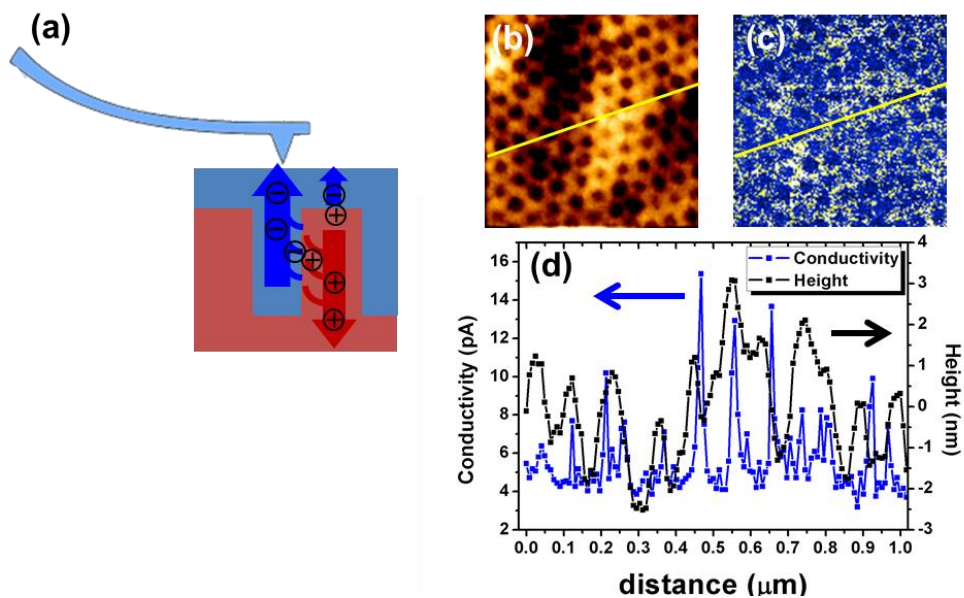


Figure 4.3.11. (a) A schematic illustration of the conductivity distribution on nanostructured P3HT:PCBM films. The QI-SFM images of: (b) height and (c) conductivity for a nanostructured P3HT:PCBM film (as-cast) with illumination and their (d) cross-sectional height and current graphs. The surroundings of pillars, which are mainly filled with PCBM, show higher conductivity than the P3HT pillar regions due to higher charge mobility of PCBM.

4.3.2. Ordered Heterojunctions by Polymer : Polymer Systems

N-type polymers as alternatives for PCBM have been widely studied. Even though efficient charge separation was available at the donor/acceptor interfaces by PCBM, it has been suffered from their strong crystallizing properties and low absorbance properties considered to be main obstacles for the commercialization. Various kinds of n-type polymer were designed and synthesized which can absorb light and have high mobilities. Recently, about 9 % of PCE²⁹ which are close to PCBM were reported using new n-type polymers. In this part, polymer-polymer ordered heterojunction using P3HT as p-type polymer and poly{[N,N'-bis(2-hexyldodecyl)-naphthalene-1,4,5,8-bis(dicarboximide)-2,6-diyl]-alt-5,5'-(2,2'-thiophene)} (PNDIT) as n-type were used for this study.

In this study we used P3HT hole pattern to avoid void formation between pillar and pillar region during deposition process as mentioned in polymer-fullerene system. We used PNDIT as n-type materials. PNDIT dissolved in DCM were spin-coated on top of 75 nm sized P3HT hole pattern to have 1:1 volume ratio between two materials. Nanostructures were well-remained after deposition of PNDIT which were confirmed from GISAXS results as shown in Figure 4.3.12 e). poly{[N,N'-bis(2-hexyldodecyl)-naphthalene-1,4,5,8-bis(dicarboximide)-2,6-diyl]-alt-5,5'-(2,2'-bithiophene)} (PNDIT2) were also tried but it did not show well-defined peaks because of low electron density differences between two materials which corresponds well with previous study.⁴⁰

Thermal annealing was used to control the mutual diffusion of p-type and n-type polymers. We annealed devices at different annealing temperatures from 120 °C to 200 °C up to 60 minutes. By using dynamics of organic materials, we could decrease the domain sizes from 75 nm as mentioned in polymer-fullerene system to

increase the device performances by increasing the interface areas between donor and acceptor materials. Moreover, because of confined geometry, diffusion dynamics were fixed at certain points which could be beneficial for device stability.

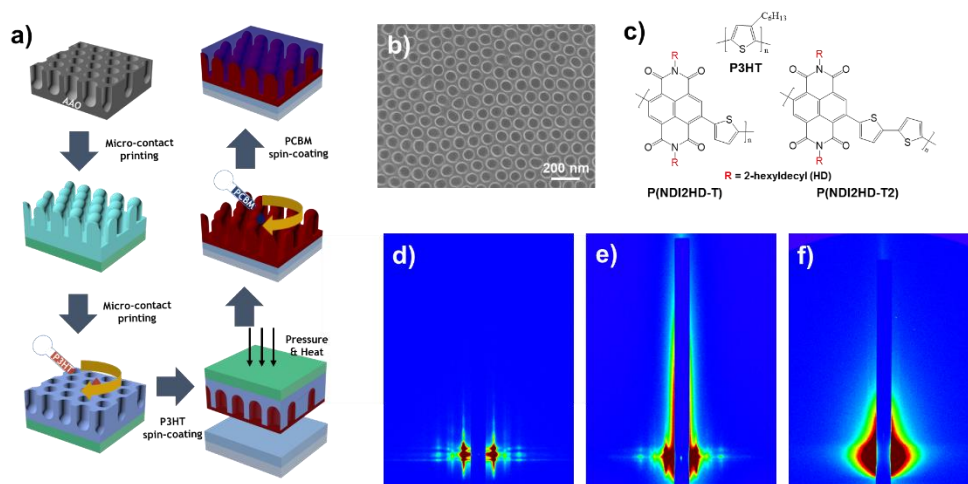


Figure 4.3.12. a) A schematic illustration for the procedure to fabricate P3HT nanoholes and subsequent PNDIT deposition. b) Plan-view scanning electron microscopy (SEM) images of P3HT nanoholes prepared. c) Chemical structures of polymers used in this study. 2D GISAXS patterns of d) P3HT nanoholes, e) P3HT nanoholes/PNDIT and f) P3HT nanoholes/PNDIT2.

To elucidate crystalline structure of samples, we measured GIWAXS experiments. P3HT nanoholes also showed strong $\pi - \pi$ peaks along the out-of-plane direction, representing the dominant face-on orientation because of nanoconfinement effect as shown in Figure 4.3.13.b). After deposition of PNDIT, their face-on orientation were decreased because of swelling of P3HT during spin-cast process shown in Figure 4.3.13.c). However, both P3HT and PNDIT showed dominant face-on orientation. After thermal annealing, the population of face-on crystallites was increased which is the opposite results of P3HT:PCBM cases in Chapter 4.3.1. As the annealing temperatures were increased, the peaks corresponding to $\pi - \pi$ more significantly increased which is attributed to interaction of thiophene groups in P3HT and PNDIT molecules under nanoconfinement which is beneficial for device performance. In order to investigate the azimuthal alignment of the P3HT chains, the angular scattering profiles were obtained at the (010) peak position as shown in Figure 4.3.13.j) and k). These profiles provide information on the angular distribution of $\pi - \pi$ stacks of P3HT and reinforce significance of nanoconfinements in polymer-polymer systems.

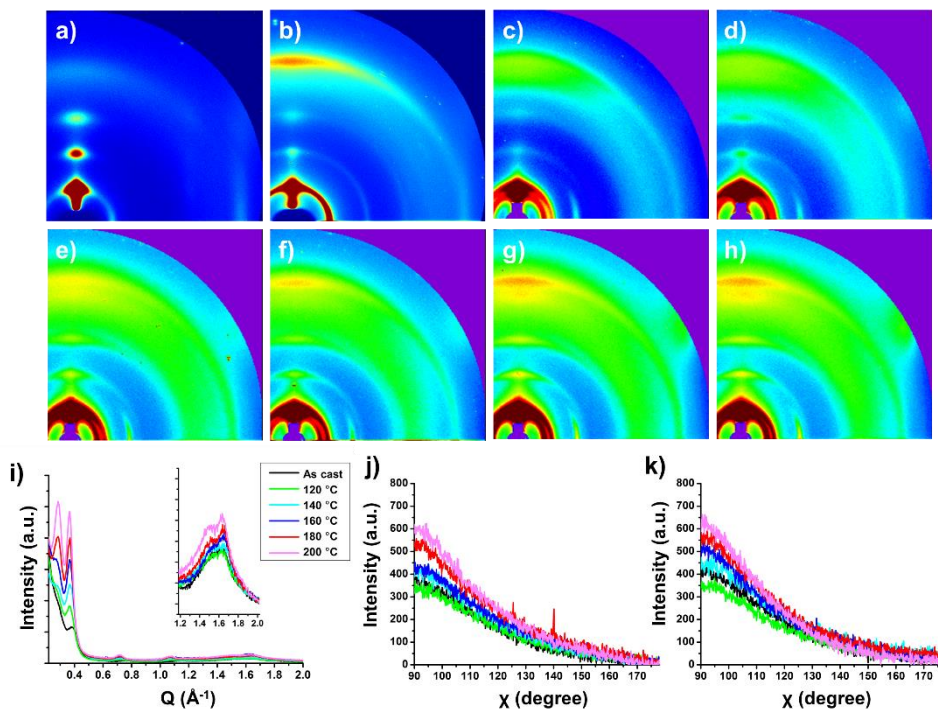


Figure 4.3.13. GIWAXS 2D scattering patterns of a) P3HT flat (spin-cast), b) P3HT nanohole pattern, c) as prepared P3HT nanohole/PCBM film, and interdiffused P3HT nanohole/PCBM films annealed at d) 120 °C, e) 140 °C, f) 160 °C, g) 180 °C, and h) 200 °C. i) Line cuts along out-of-direction of interdiffused P3HT nanohole/PCBM films annealed at different temperatures. Angular cuts at the (010) position of j) PNDIT and k) P3HT.

To quantitatively analyze polymer-polymer dynamics under confinements, we performed in-situ GISAXS experiments using the same method in Chapter 4.3.1. They were measured *in-situ* annealing from 120 °C to 200 °C for 2 hours. We could observe strong hexagonal peaks at $q=0.007 \text{ \AA}^{-1}$ and their temperature and time dependent changes of peak intensities were analyzed. From the measurement of non-anneal sample for 2 hours showed no decrease in peak intensities as shown in Figure 4.3.14.a) representing little damages on samples by x-ray beams during measurements. When annealed at 120 °C, their peak intensities were slightly decreased less than 10 % of initial values. As the annealing temperatures were increased, peak intensities were more rapidly decreased and reached to certain stabilized points. Even annealing at 200 °C which is harsh temperature conditions for polymer, they were decreased to 60 % of initial values. The amount diffused molecules by donor and acceptor molecules can be qualitatively analyzed by calculating the total scattering intensity (TSI) of the peaks at different annealing temperatures and times. Integrated values of each curves will be shown at the below part.

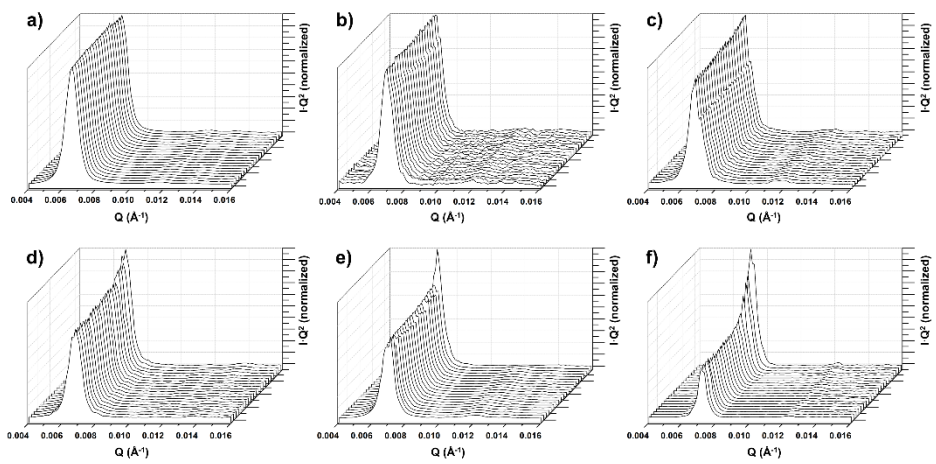


Figure 4.3.14. The changes in GISAXS scattering profiles of nanostructured P3HT/PNDIT as a function of annealing time (up to 120 min) at: a) as-prepared, b) 120 °C, c) 140 °C, d) 160 °C, e) 180 °C, and f) 200 °C.

Fraction of diffused molecules and PCE at different annealing temperatures and times were plotted in Figure 4.3.15. The contour plot shows the summary of fraction of diffused molecules at different temperatures and times which were calculated from integrated values of GISAXS curves. The rate of diffusion was differed as well as reached to saturated points which do not diffuse any more according to annealing temperatures. As the annealing the temperatures were increased, the values were more rapidly decreased. Figures 4.3.15.b) shows the relative PCE calculated by PCE of OHJ divided by reference PCE (Best PCE by BHJ) at different annealing temperatures and times. Yellow regions in the figure show superb device performance including best device performance which is 50 % higher than PCE of BHJ. This implies proper amount of diffusion is important for device performance. Moreover, their devices showed superior thermal stability even annealed at 200 °C due to stabilized diffusion of molecules by nanoconfinements. Their summarized device stability results were shown in Figure 4.3.16..

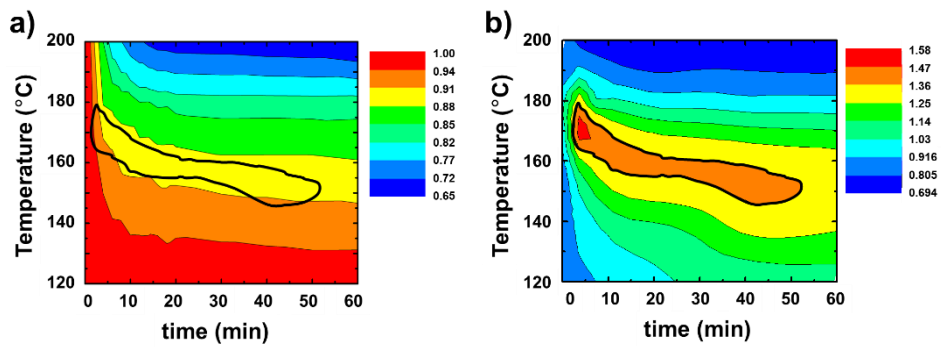


Figure 4.3.15. Contour plots of a) molecular diffusion and d) power conversion efficiencies as a function of annealing time and temperatures.

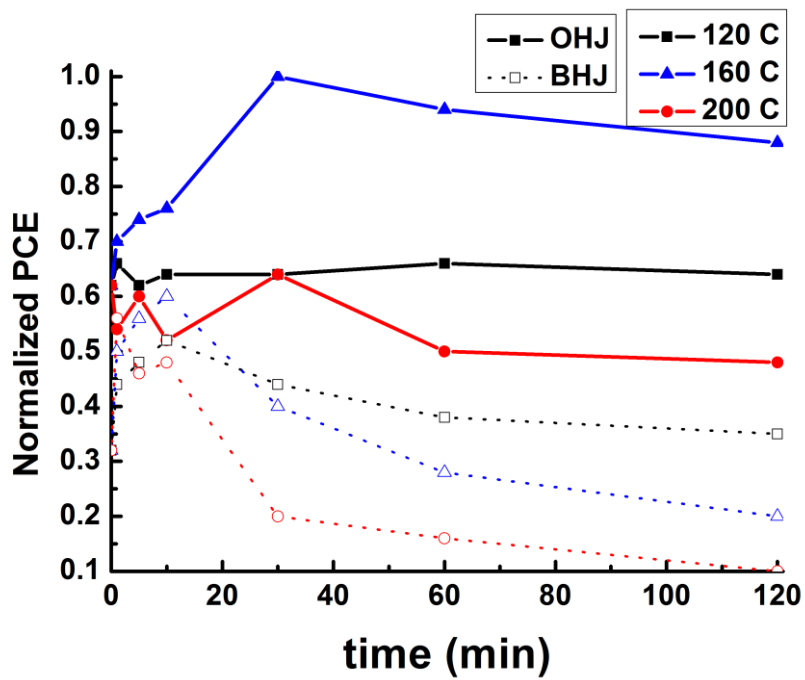


Figure 4.3.16. Device stabilities as a function of active layer geometry, annealing temperature and time.

4.4. Challenges and Further Works

The effects of nanoconfinements on structural properties and dynamics of conjugated polymers were studied by fabricating ordered heterojunction geometry in organic solar cells. Dominant face-on orientation with high crystallinity and smaller size of nano-domains with stabilized nanomorphologies were obtained by employing nanoconfinement effects. Based on those nanoconfinement effects on structural properties and dynamics, more than 50 % higher device performance along with 200 °C thermal stability were obtained. This reinforces the importance and prominence of our strategies. However, there exist several challenges to be commercialized and applied for other applications.

Even though we successfully fabricated nanostructures using low bandgap polymers which is amorphous and studied effects of nanoconfinement on structural properties showing significantly enhanced electrical properties, we could not apply those nanostructures in OPV because of difficulties in fabrication process. There are no proper solvents for the deposition of n-type materials on top of low bandgap polymer nanostructures. Dichloromethane is a well-known orthogonal solvent for P3HT and we used them in P3HT:PCBM and P3HT:PNDIT OHJ system. Even though some studies used DCM with additives to fabricate bilayer structures with low bandgap and PCBM, low bandgap nanostructures were too easily destroyed during spin-coating process due to large amounts of amorphous parts in polymers. Suitable solvents or fabrication methods will be required to extend our strategies to other materials.

We also show the prominence of electrically doped nanopillars as a method to increase charge mobility and oxidation stability. Their charge mobilities were increased more than 500 times compared to bulk thin films and the oxidation stability

were dramatically increased. Considering their large surface area, they could be widely used for other applications.

Bibliography

1. C. K. Chiang, C. R. Fincher, Y. W. Park, A. J. Heeger, H. Shirakawa, E. J. Louis, S. C. Gau and A. G. MacDiarmid, *Physical review letters*, 1977, **39**, 1098-1101.
2. M. Knupfer, *Applied Physics A*, 2003, **77**, 623-626.
3. P. Peumans and S. R. Forrest, *Chemical Physics Letters*, 2004, **398**, 27-31.
4. L. A. A. Pettersson, L. S. Roman and O. Inganäs, *Journal of Applied Physics*, 1999, **86**, 487-496.
5. J. J. M. Halls, K. Pichler and R. H. Friend, *Applied Physics Letters*, 1996, **68**, 3120.
6. J. J. M. Halls, C. A. Walsh, N. C. Greenham, E. A. Marsegli, R. H. Friend, S. C. Moratti and A. B. Holmes, *Nature*, 1995, **376**, 498.
7. J. G. G. Yu, J. C. Hummelen, F. Wudl, A. J. Heeger, *Science*, 1995, **270**, 1789-1791.
8. S. E. Shaheen, C. J. Brabec, N. S. Sariciftci, F. Padinger, T. Fromherz and J. C. Hummelen, *Applied Physics Letters*, 2001, **78**, 841.
9. P. Cheng and X. Zhan, *Chemical Society reviews*, 2016, **45**, 2544-2582.
10. C. Lindqvist, A. Sanz-Velasco, E. Wang, O. Bäcke, S. Gustafsson, E. Olsson, M. R. Andersson and C. Müller, *Journal of Materials Chemistry A*, 2013, **1**, 7174.
11. O. Backe, C. Lindqvist, A. Diaz de Zerio Mendaza, S. Gustafsson, E. Wang, M. R. Andersson, C. Muller and E. Olsson, *Nanoscale*, 2015, **7**, 8451-8456.
12. J. Jo, S.-S. Kim, S.-I. Na, B.-K. Yu and D.-Y. Kim, *Advanced Functional Materials*, 2009, **19**, 866-874.
13. A. Swinnen, I. Haeldermans, M. vande Ven, J. D'Haen, G. Vanhoyland, S. Aresu, M. D'Olieslaeger and J. Manca, *Advanced Functional Materials*, 2006, **16**, 760-765.
14. K. Kawano, R. Pacios, D. Poplavskyy, J. Nelson, D. D. C. Bradley and J. R. Durrant, *Solar Energy Materials and Solar Cells*, 2006, **90**, 3520-3530.
15. V. S. Balderrama, M. Estrada, P. L. Han, P. Granero, J. Pallarés, J. Ferré-Borrull and L. F. Marsal, *Solar Energy Materials and Solar Cells*, 2014, **125**, 155-163.
16. K. Norrman, M. V. Madsen, S. A. Gevorgyan and F. C. Krebs, *Journal of the American Chemical Society*, 2010, **132**, 16883.
17. D. J. Lipomi and Z. Bao, *Energy & Environmental Science*, 2011, **4**, 3314.
18. S. Savagatrup, A. D. Printz, T. F. O'Connor, A. V. Zaretski, D. Rodriguez, E. J. Sawyer, K. M. Rajan, R. I. Acosta, S. E. Root and D. J. Lipomi, *Energy & Environmental Science*, 2015, **8**, 55-80.
19. S. Savagatrup, A. D. Printz, T. F. O'Connor, A. V. Zaretski and D. J. Lipomi, *Chemistry of Materials*, 2014, **26**, 3028-3041.
20. N. S. Sariciftci, L. Smilowitz, A. J. Heeger and F. Wudl, *Science*, 1992, **258**, 1474-

- 1476.
21. B. Kraabel, C. H. Lee, D. McBranch, D. Moses, N. S. Sariciftci and A. J. Heeger, *Chemical Physics Letters*, 1993, **213**, 389-394.
 22. P. Schilinsky, C. Waldauf and C. J. Brabec, *Applied Physics Letters*, 2002, **81**, 3885-3887.
 23. Y. Liang, Z. Xu, J. Xia, S. T. Tsai, Y. Wu, G. Li, C. Ray and L. Yu, *Advanced materials*, 2010, **22**, E135-138.
 24. Z. He, C. Zhong, S. Su, M. Xu, H. Wu and Y. Cao, *Nature Photonics*, 2012, **6**, 593-597.
 25. S. H. Liao, H. J. Jhuo, Y. S. Cheng and S. A. Chen, *Advanced materials*, 2013, **25**, 4766-4771.
 26. Z. He, B. Xiao, F. Liu, H. Wu, Y. Yang, S. Xiao, C. Wang, T. P. Russell and Y. Cao, *Nature Photonics*, 2015, **9**, 174-179.
 27. T. Kim, J. H. Kim, T. E. Kang, C. Lee, H. Kang, M. Shin, C. Wang, B. Ma, U. Jeong, T. S. Kim and B. J. Kim, *Nature communications*, 2015, **6**, 8547.
 28. Y. Guo, Y. Li, O. Awartani, H. Han, J. Zhao, H. Ade, H. Yan and D. Zhao, *Advanced materials*, 2017, **29**.
 29. Z. Li, X. Xu, W. Zhang, X. Meng, Z. Genene, W. Ma, W. Mammo, A. Yartsev, M. R. Andersson, R. A. J. Janssen and E. Wang, *Energy Environ. Sci.*, 2017, **10**, 2212-2221.
 30. S. Li, L. Ye, W. Zhao, S. Zhang, S. Mukherjee, H. Ade and J. Hou, *Advanced materials*, 2016, **28**, 9423-9429.
 31. L. Ye, W. Zhao, S. Li, S. Mukherjee, J. H. Carpenter, O. Awartani, X. Jiao, J. Hou and H. Ade, *Advanced Energy Materials*, 2017, **7**, 1602000.
 32. W. Zhao, S. Li, H. Yao, S. Zhang, Y. Zhang, B. Yang and J. Hou, *Journal of the American Chemical Society*, 2017, **139**, 7148-7151.
 33. M. Li, K. Gao, X. Wan, Q. Zhang, B. Kan, R. Xia, F. Liu, X. Yang, H. Feng, W. Ni, Y. Wang, J. Peng, H. Zhang, Z. Liang, H.-L. Yip, X. Peng, Y. Cao and Y. Chen, *Nature Photonics*, 2016, **11**, 85-90.
 34. F. Padinger, R. S. Rittberger and N. S. Sariciftci, *Advanced Functional Materials*, 2003, **13**, 85-88.
 35. G. Li, V. Shrotriya, J. Huang, Y. Yao, T. Moriarty, K. Emery and Y. Yang, *Nature Materials*, 2005, **4**, 864-868.
 36. F. Zhang, K. G. Jespersen, C. Björström, M. Svensson, M. R. Andersson, V. Sundström, K. Magnusson, E. Moons, A. Yartsev and O. Inganäs, *Advanced Functional Materials*, 2006, **16**, 667-674.

37. J. Peet, J. Y. Kim, N. E. Coates, W. L. Ma, D. Moses, A. J. Heeger and G. C. Bazan, *Nat Mater*, 2007, **6**, 497-500.
38. Y. Yang, K. Mielczarek, A. Zakhidov and W. Hu, *ACS applied materials & interfaces*, 2014, **6**, 19282-19287.
39. D. Chen, W. Zhao and T. P. Russell, *ACS Nano*, 2012, **6**, 1479-1485.
40. T. Pfadler, M. Coric, C. M. Palumbiny, A. C. Jakowetz, K. P. Strunk, J. A. Dorman, P. Ehrenreich, C. Wang, A. Hexemer, R. Q. Png, P. K. Ho, P. Muller-Buschbaum, J. Weickert and L. Schmidt-Mende, *ACS Nano*, 2014, **8**, 12397-12409.
41. X. He, F. Gao, G. Tu, D. G. Hasko, S. Hüttner, N. C. Greenham, U. Steiner, R. H. Friend and W. T. S. Huck, *Advanced Functional Materials*, 2011, **21**, 139-146.
42. J. S. Kim, Y. Park, D. Y. Lee, J. H. Lee, J. H. Park, J. K. Kim and K. Cho, *Advanced Functional Materials*, 2010, **20**, 540-545.
43. M.-S. Kim, J.-S. Kim, J. C. Cho, M. Shtein, L. J. Guo and J. Kim, *Applied Physics Letters*, 2007, **90**, 123113.
44. X. Lu, H. Hlaing, C.-Y. Nam, K. G. Yager, C. T. Black and B. M. Ocko, *Chemistry of Materials*, 2015, **27**, 60-66.
45. M. Aryal, F. Buyukserin, K. Mielczarek, X.-M. Zhao, J. Gao, A. Zakhidov and W. Hu, *Journal of Vacuum Science & Technology B: Microelectronics and Nanometer Structures*, 2008, **26**, 2562-2566.
46. T. Kim, H. Yoon, H. J. Song, N. Haberkorn, Y. Cho, S. H. Sung, C. H. Lee, K. Char and P. Theato, *Macromolecular rapid communications*, 2012, **33**, 2035-2040.
47. X. He, F. Gao, G. Tu, D. Hasko, S. Huttner, U. Steiner, N. C. Greenham, R. H. Friend and W. T. Huck, *Nano Lett*, 2010, **10**, 1302-1307.
48. G. Ding, C. Li, X. Li, Y. Wu, J. Liu, Y. Li, Z. Hu and Y. Li, *Nanoscale*, 2015, **7**, 11024-11032.
49. W. Zeng, K. S. L. Chong, H. Y. Low, E. L. Williams, T. L. Tam and A. Sellinger, *Thin Solid Films*, 2009, **517**, 6833-6836.
50. Y. Yang, K. Mielczarek, M. Aryal, A. Zakhidov and W. Hu, *Nanoscale*, 2014, **6**, 7576-7584.
51. C. W. Tang and A. C. Albrecht, *The Journal of chemical physics*, 1975, **62**, 2139.
52. C. W. Tang, *Applied Physics Letters*, 1986, **48**, 183.
53. G. Ding, K. Wang, X. Li, C. Wang, Z. Huc and J. Liu, *Polymer Chemistry*, 2017, **8**, 2666-2674.
54. B. Azzopardi, C. J. M. Emmott, A. Urbina, F. C. Krebs, J. Mutale and J. Nelson, *Energy & Environmental Science*, 2011, **4**, 3741.
55. M. Jorgensen, K. Norrman, S. A. Gevorgyan, T. Tromholt, B. Andreasen and F. C.

- Krebs, *Advanced materials*, 2012, **24**, 580-612.
56. S. A. Gevorgyan, M. V. Madsen, B. Roth, M. Corazza, M. Hösel, R. R. Søndergaard, M. Jørgensen and F. C. Krebs, *Advanced Energy Materials*, 2016, **6**, 1501208.
57. C. H. Peters, I. T. Sachs-Quintana, J. P. Kastrop, S. Beaupré, M. Leclerc and M. D. McGehee, *Advanced Energy Materials*, 2011, **1**, 491-494.
58. R. Roesch, T. Faber, E. von Hauff, T. M. Brown, M. Lira-Cantu and H. Hoppe, *Advanced Energy Materials*, 2015, **5**, 1501407.
59. J. U. Lee, J. W. Jung, J. W. Jo and W. H. Jo, *Journal of Materials Chemistry*, 2012, **22**, 24265.
60. J. Xu, S. Wang, G.-J. N. Wang, C. Zhu, S. Luo, L. Jin, X. Gu, S. Chen, V. R. Feig, J. W. F. To, S. Rondeau-Gagné, J. Park, B. C. Schroeder, C. Lu, J. Y. Oh, Y. Wang, Y.-H. Kim, H. Yan, R. Sinclair, D. Zhou, G. Xue, B. Murmann, C. Linder, W. Cai, J. B.-H. Tok, J. W. Chung and Z. Bao, *Science*, 2017, **335**, 59-64.
61. J. L. Keddie, R. A. L. Jones and R. A. Cory, *Europhysics Letters*, 1994, **27**, 59-64.
62. D. Wang, K. Nakajima, F. Liu, S. Shi and T. P. Russell, *ACS Nano*, 2017, **11**, 8660-8667.
63. C. J. Ellison and J. M. Torkelson, *Nat Mater*, 2003, **2**, 695-700.
64. B. G. Kim, E. J. Jeong, J. W. Chung, S. Seo, B. Koo and J. Kim, *Nat Mater*, 2013, **12**, 659-664.
65. L. Si, M. V. Massa, K. Dalnoki-Veress, H. R. Brown and R. A. Jones, *Physical review letters*, 2005, **94**, 127801.
66. M. Aryal, K. Trivedi and W. W. Hu, *ACS Nano*, 2009, **3**, 3085-2090.
67. D. E. Johnston, K. G. Yager, H. Hlaing, X. Lu, B. M. Ocko and C. T. Black, *ACS Nano*, 2014, **8**, 243-249.
68. M. Krutyeva, A. Wischnewski, M. Monkenbusch, L. Willner, J. Maiz, C. Mijangos, A. Arbe, J. Colmenero, A. Radulescu, O. Holderer, M. Ohl and D. Richter, *Physical review letters*, 2013, **110**, 108303.
69. K. Shin, S. Obukhov, J. T. Chen, J. Huh, Y. Hwang, S. Mok, P. Dobriyal, P. Thiyagarajan and T. P. Russell, *Nat Mater*, 2007, **6**, 961-965.
70. V. Skrypnichuk, G. J. Wetzelaer, P. I. Gordiichuk, S. C. Mannsfeld, A. Herrmann, M. F. Toney and D. R. Barbero, *Advanced materials*, 2016, **28**, 2359-2366.
71. T. Uemura, N. Yanai, S. Watanabe, H. Tanaka, R. Numaguchi, M. T. Miyahara, Y. Ohta, M. Nagaoka and S. Kitagawa, *Nature communications*, 2010, **1**, 83.
72. J. Lee, K. H. Ku, M. Kim, J. M. Shin, J. Han, C. H. Park, G. R. Yi, S. G. Jang and B. J. Kim, *Advanced materials*, 2017, **29**.
73. J. M. Shin, Y. Kim, H. Yun, G. R. Yi and B. J. Kim, *ACS Nano*, 2017, **11**, 2133-2142.

74. K. H. Kim, J. L. Liao, S. W. Lee, B. Sim, C. K. Moon, G. H. Lee, H. J. Kim, Y. Chi and J. J. Kim, *Advanced materials*, 2016, **28**, 2526-2532.
75. K. H. Kim, C. K. Moon, J. H. Lee, S. Y. Kim and J. J. Kim, *Advanced materials*, 2014, **26**, 3844-3847.
76. C. K. Moon, K. H. Kim and J. J. Kim, *Nature communications*, 2017, **8**, 791.
77. Y. H. Sung, P.-H. Jung, K.-H. Han, Y. D. Kim, J.-J. Kim and H. Lee, *Optical Materials*, 2017, **72**, 828-832.
78. V. A. Kolesov, C. Fuentes-Hernandez, W. F. Chou, N. Aizawa, F. A. Larrain, M. Wang, A. Perrotta, S. Choi, S. Graham, G. C. Bazan, T. Q. Nguyen, S. R. Marder and B. Kippelen, *Nat Mater*, 2017, **16**, 474-480.
79. H. Masuda and K. Fukuda, *Science*, 1995, **268**, 1466-1468.
80. M. K. Choi, H. Yoon, K. Lee and K. Shin, *Langmuir*, 2011, **27**, 2132-2137.
81. J. Ko, J. Song, H. Yoon, T. Kim, C. Lee, R. Berger and K. Char, *Advanced Materials Interfaces*, 2016, **3**, 1600264.
82. P. Müller-Buschbaum, *European Polymer Journal*, 2016, **81**, 470-493.
83. Y. Zhong, K. Suzuki, D. Inoue, D. Hashizume, S. Izawa, K. Hashimoto, T. Koganezawa and K. Tajima, *J. Mater. Chem. A*, 2016, **4**, 3335-3341.
84. S. Y. Yang, J. Park, J. Yoon, M. Ree, S. K. Jang and J. K. Kim, *Advanced Functional Materials*, 2008, **18**, 1371-1377.
85. D. R. Barbero and N. Boulanger, *ACS Nano*, 2017, **11**, 9906-9913.
86. K. H. Lee, Y. Zhang, P. L. Burn, I. R. Gentle, M. James, A. Nelson and P. Meredith, *Journal of Materials Chemistry C*, 2013, **1**, 2593.
87. N. D. Treat, M. A. Brady, G. Smith, M. F. Toney, E. J. Kramer, C. J. Hawker and M. L. Chabynyc, *Advanced Energy Materials*, 2011, **1**, 82-89.
88. N. D. Treat, T. E. Mates, C. J. Hawker, E. J. Kramer and M. L. Chabynyc, *Macromolecules*, 2013, **46**, 1002-1007.
89. P. Cheng, C. Yan, T. K. Lau, J. Mai, X. Lu and X. Zhan, *Advanced materials*, 2016, **28**, 5822-5829.
90. Q. Liu, J. Toudert, F. Liu, P. Mantilla-Perez, M. M. Bajo, T. P. Russell and J. Martorell, *Advanced Energy Materials*, 2017, DOI: 10.1002/aenm.201701201, 1701201.
91. L. Tan, F. Yang, M. R. Kim, P. Li, D. T. Gangadharan, J. Margot, R. Izquierdo, M. Chaker and D. Ma, *ACS applied materials & interfaces*, 2017, **9**, 26257-26267.
92. D. H. L. Hyun Ah Um, Dong Uk Heo, Da Seul Yang, Jicheol Shin, Hionsuck Baik, Min Ju Cho, Dong Hoon Choi, *ACS Nano*, 2015, **9**, 5264-5274.
93. S. Wang, M. Kappl, I. Liebewirth, M. Muller, K. Kirchhoff, W. Pisula and K. Mullen,

- Advanced materials*, 2012, **24**, 417-420.
94. M. Chang, Z. Su and E. Egap, *Macromolecules*, 2016, **49**, 9449-9456.
 95. P.-H. Chu, N. Kleinhenz, N. Persson, M. McBride, J. L. Hernandez, B. Fu, G. Zhang and E. Reichmanis, *Chemistry of Materials*, 2016, **28**, 9099-9109.
 96. Y. Lee, J. Y. Oh, S. Y. Son, T. Park and U. Jeong, *ACS applied materials & interfaces*, 2015, **7**, 27694-27702.
 97. F. S. K. Hao Xin, Samson A. Jenekhe, *Journal of the American Chemical Society*, 2008, **130**, 5424-5425.
 98. S. B. Jo, W. H. Lee, L. Qiu and K. Cho, *Journal of Materials Chemistry*, 2012, **22**, 4244.
 99. D. H. Kim, J. Mei, A. L. Ayzner, K. Schmidt, G. Giri, A. L. Appleton, M. F. Toney and Z. Bao, *Energy & Environmental Science*, 2014, **7**, 1103.
 100. J. H. Kim, M. Kim, H. Jinnai, T. J. Shin, H. Kim, J. H. Park, S. B. Jo and K. Cho, *ACS applied materials & interfaces*, 2014, **6**, 5640-5650.
 101. M. Kim, J. H. Park, J. H. Kim, J. H. Sung, S. B. Jo, M.-H. Jo and K. Cho, *Advanced Energy Materials*, 2015, **5**, 1401317.
 102. J. Lee, S. B. Jo, M. Kim, H. G. Kim, J. Shin, H. Kim and K. Cho, *Advanced materials*, 2014, **26**, 6706-6714.
 103. J. Lee, D. H. Sin, B. Moon, J. Shin, H. G. Kim, M. Kim and K. Cho, *Energy Environ. Sci.*, 2017, **10**, 247-257.
 104. J. Y. Oh, M. Shin, H. W. Lee, Y. J. Lee, H. K. Baik and U. Jeong, *ACS applied materials & interfaces*, 2014, **6**, 7759-7765.
 105. H. Yan, Y. Song, G. R. McKeown, G. D. Scholes and D. S. Seferos, *Advanced materials*, 2015, **27**, 3484-3491.
 106. C. J. T. Alexander L. Ayzner, Sarah H. Tolbert, Benjamin J. Schwartz, *The Journal of Physical Chemistry C*, 2009, **113**, 20050-20060.
 107. W. T. Choi, J. Song, J. Ko, Y. Jang, T.-H. Kim, Y.-S. Han, J. Lim, C. Lee and K. Char, *Journal of Polymer Science Part B: Polymer Physics*, 2016, **54**, 128-134.
 108. C.-Y. Chen, S.-H. Chan, J.-Y. Li, K.-H. Wu, H.-L. Chen, J.-H. Chen, W.-Y. Huang and S.-A. Chen, *Macromolecules*, 2010, **43**, 7305-7311.
 109. Y.-C. Li, K.-B. Chen, H.-L. Chen, C.-S. Hsu, C.-S. Tsao, J.-H. Chen and S.-A. Chen, *Langmuir*, 2006, **22**, 11009-11015.
 110. B. J. Bauer, E. K. Hobbie and M. L. Becker, *Macromolecules*, 2006, **39**, 2637-2642.
 111. L. A. Hough, M. F. Islam, B. Hammouda, A. G. Yodh and P. A. Heiney, *Nano Letters*, 2006, **6**, 313-317.
 112. A. Urbina, C. Miguel, J. L. Delgado, F. Langa, C. Díaz-Paniagua and F. Batallán,

- Physical Review B*, 2008, **78**.
113. J. W. Kiel, A. P. Eberle and M. E. Mackay, *Physical review letters*, 2010, **105**, 168701.
114. J. W. Kiel, M. E. Mackay, B. J. Kirby, B. B. Maranville and C. F. Majkrzak, *The Journal of chemical physics*, 2010, **133**, 074902.
115. S. Guo, W. Wang, E. M. Herzig, A. Naumann, G. Tainter, J. Perlich and P. Muller-Buschbaum, *ACS applied materials & interfaces*, 2017, **9**, 3740-3748.
116. J. Huang, J. H. Carpenter, C. Z. Li, J. S. Yu, H. Ade and A. K. Jen, *Advanced materials*, 2016, **28**, 967-974.
117. P. Cheng, C. Yan, Y. Wu, S. Dai, W. Ma and X. Zhan, *J. Mater. Chem. C*, 2016, **4**, 8086-8093.
118. O. K. Kwon, M. A. Uddin, J. H. Park, S. K. Park, T. L. Nguyen, H. Y. Woo and S. Y. Park, *Advanced materials*, 2016, **28**, 910-916.
119. Z. Zheng, O. M. Awartani, B. Gautam, D. Liu, Y. Qin, W. Li, A. Bataller, K. Gundogdu, H. Ade and J. Hou, *Advanced materials*, 2017, **29**.
120. Z. Wang, Y. Zhang, J. Zhang, Z. Wei and W. Ma, *Advanced Energy Materials*, 2016, **6**, 1502456.
121. K. C. Lee, S. Song, J. Lee, D. S. Kim, J. Y. Kim and C. Yang, *Chemphyschem : a European journal of chemical physics and physical chemistry*, 2015, **16**, 1305-1314.
122. L. Yang, J. R. Tumbleston, H. Zhou, H. Ade and W. You, *Energy Environ. Sci.*, 2013, **6**, 316-326.
123. O. D. Jurchescu, J. Baas and T. T. M. Palstra, *Applied Physics Letters*, 2004, **84**, 3061-3063.
124. R. W. I. de Boer and A. F. Morpurgo, *Physical Review B*, 2005, **72**.
125. W.-R. Wu, U.-S. Jeng, C.-J. Su, K.-H. Wei, M.-S. Su, M.-Y. Chiu, C.-Y. Chen, W.-B. Su, C.-H. Su and A.-C. Su, *ACS Nano*, 2011, **5**, 6233-6243.
126. S. Guo, M. A. Ruderer, M. Rawolle, V. Korstgens, C. Birkenstock, J. Perlich and P. Muller-Buschbaum, *ACS applied materials & interfaces*, 2013, **5**, 8581-8590.
127. K. W. Chou, B. Yan, R. Li, E. Q. Li, K. Zhao, D. H. Anjum, S. Alvarez, R. Gassaway, A. Biocca, S. T. Thoroddsen, A. Hexemer and A. Amassian, *Advanced materials*, 2013, **25**, 1923-1929.

국문초록

전도성 고분자는 전기적, 광학적 성질에 기존에 플라스틱이 지니고 있던 가볍고, 튼튼하고, 유연하다는 성질이 더해져서 차세대 반도체 물질로 각광받았다. 이러한 전도성 고분자를 유기박막트랜지스터, 유기발광소자, 유기태양전지와 같은 다양한 분야로의 응용을 위한 연구가 활발히 진행되어왔다. 특히 유기발광소자의 경우 이미 상용화되어 디스플레이와 광원을 대체하고 있는 수준에 이르렀다. 가볍고, 유연할 뿐만 아니라 값이 저렴한 유기태양전지 또한 인류의 에너지 문제를 해결하는데 기여할 것으로 기대되어 연구가 진행되고 있다.

1980년대 광전환 효율이 0.1 %도 안되던 유기태양전지는 최근 12 %의 효율이 보고될 정도로 비약적으로 발전하였다. 이는 저밴드갭 고분자의 합성과 같은 재료에서의 혁신과 벌크이종접합 구조 형성과 같은 공정 과정에서의 혁신이 있어서 가능하였다. 저밴드갭 고분자를 통해 더 많은 양의 빛을 흡수하여 더 효율적으로 활용할 수 있게 되었으며, 벌크이종접합 구조를 통해 전하 분리와 이동에 효율성을 획기적으로 높일 수 있었다. 하지만, 유기물 고유의 단점인 화학적 불안정성과 나노혼합물의 불안정성 때문에 상용화되기에는 힘들어보인다. 이번에는 소자의 효율 뿐만 아니라 안정성을 함께 높을 수 있는 획기적인 방법이 필요한 때이다.

나노간섭효과는 높은 소자의 효율과 안정성을 모두 한 번에 실현할 수 있는 가능성을 가지고 있다. 고분자가 나노 구조에 갇힐 경우 벌크

상태에서는 얻을 수 없는 다른 구조적, 동역학적 특성을 보인다. 전도성 고분자의 구조적, 동역학적 특성을 함께 조절할 수 있다면 높은 효율을 가지면서도 안정적인 태양전지를 구현할 수 있을 것이다. 본 연구에서는 이러한 다양한 전도성 고분자에 대한 나노간힘효과를 체계적으로 진행하여 기존에 발견하기 어려웠던 우수한 성질들을 확인할 수 있었다. 이러한 나노간힘효과를 유기태양전지에 적용하여 그 가능성을 확인하였다.

첫번째 장에서는 전도성 고분자, 유기태양전지 그리고 나노간힘효과의 전반적인 내용을 설명하고 이를 통해 본 연구의 중요성과 독창성을 설명하고자 한다.

두번째 장에서는 나노간힘효과에 의한 전도성 고분자의 구조적 특성 변화를 연구하였다. 이를 위해 우선 다양한 전도성 고분자를 다양한 형태 및 크기를 만들 수 있는 패터닝 기법을 개발하여 다른 종류의 전도성 고분자를 다양한 크기로 제작할 하였다. 이렇게 다양하게 나노구조화된 전도성 고분자의 구조적 특성을 조사하였고, 그 결과 나노간힘효과에 의해 비결정성 고분자의 결정성의 상당히 증가하는 것을 확인할 수 있었다. 실제로 수직방향으로 전하이동도를 측정하였을 때 100 배 이상 증가함을 확인하였다. 뿐만 아니라 쉽게 산화되는 점을 극복하기 위해 나노기둥들의 표면들을 도핑 처리하였다. 이를 통해 2-3 배 추가적으로 높은 전하이동도를 얻을 수 있었을 뿐만 아니라, 공기에서도 안정적인 특성을 보이는 것을 확인하였다.

세번째 장에서는 두 가지 나노간힘구조의 예시를 통해 나노간힘조건 하에서 분자들의 독특한 동역학 거동을 확인하고, 이를

유기태양전지에 응용가능 함을 보였다. 첫 번째 나노간힘구조는 고분자 나노와이어의 네트워크 구조에 의한 나노간힘구조이다. 물리적으로 연결된 나노와이어들이 주변의 PCBM의 확산 및 결정화를 억제시켜 120 ° C의 높은 온도에서도 효율이 안정적으로 유지되는 것을 확인할 수 있었다. 두번째 나노간힘구조는 유사 정렬된 이중접합구조의 의한 것이다. 순차적 코팅 방식을 이용하면 전자주개 및 받개 물질의 계면이 손가락이 맞물리듯이 엮힌 구조를 형성할 수 있고, 이를 바탕으로 높은 효율과 안정성을 얻을 수 있었다.

마지막 장에서는 앞서 살펴본 나노간힘효과에 의한 구조적 특성과 동역학적 특성을 모두 사용하여 유기태양전지에 적용하였다. 이를 위해 100 nm 간격으로 전자주개 및 받개 물질이 규칙적으로 존재하는 정렬된 이중접합 구조를 사용하였다. 나노기둥 또는 나노구멍 구조로 존재하는 고분자들은 나노간힘효과에 의해 수직 방향으로 향상된 전하이동도를 얻을 수 있었다. 뿐만 아니라 이들이 나노 구조하에 규칙적으로 존재하기에 열을 계속 주더라도 나노구조가 안정적으로 유지되는 것을 정량적으로 확인하였고, 실제로 소자 성능도 200 ° C 와 같은 아주 극한의 조건에서도 유지되는 것을 확인하였다. 즉, 이러한 나노 간힘효과를 전도성 고분자에 도입할 경우 유기물의 가지는 한계를 극복할 수 있음을 확인할 수 있었으며 향후 다른 유기전자소자에서 활용될 수 있을 것이다.

